

DISSERTATION

Numerical, Semi-analytical and Analytical Approaches for Investigating Parametrically Excited Non-linear Systems

submitted in partial fulfilment of the requirements for the degree
Doctor of Technical Sciences (Dr.techn.)
under supervision of

Ao.Univ.Prof. Dipl.-Ing. Dr.techn. Horst Ecker
Institute of Mechanics and Mechatronics
Division Technical Dynamics
TU Wien

and

Prof. Brian Richard Mace MA Dphil PhD
Head of the Department of Mechanical Engineering
University of Auckland

submitted to the TU Wien
Faculty of Mechanical and Industrial Engineering

by

Dipl.-Ing. Till Jochen Kniffka
1027794
Wagramer Str. 23/1/3.6
1220 Vienna

Vienna, 12/07/2016

“And if you only do solid research instead of making a groundbreaking discovery, what does it matter?”

“Only do solid research?! Uh... I come to you for help, and you insult me?!”

The Big Bang Theory, season 8, episode 13

For all the people who believe in fundamental research.

Acknowledgements

The research efforts leading to the presented results were supported by a One-year Grant for Doctoral Candidates by the German Academic Exchange Service (DAAD) and a Marietta Blau Grant by the Federal Ministry of Science, Research and Economy (BMWFV), Republic of Austria. I would like to thank these institutions for supporting research in all fields of science, technology and arts. I deeply believe that this investment is returned multiply by the grant holders via their work and their commitment not only during their doctoral program but during their whole professional life.

Personally, I first and foremost have to thank Prof. Horst Ecker who has supported me fatherlike. He also introduced me to the topic of parametric excitation and, from the beginning, had great confidence in me which lay the basement for my scientific career. His expert knowledge on parametric excitation is reflected by this thesis.

I also have to thank Prof. Brian Mace and Dr. Roger Halkyard who welcoming hosted me at the University of Auckland. Prof. Brian Mace has been a great help with his deep knowledge about non-linear dynamics. Dr. Roger Halkyard supported the presented work with his questioning mind and his positive suggestions in fruitful discussions.

Furthermore, I have to thank all the staff at the Institute of Mechanics and Mechatronics for what they have taught me and how they supported me, notably Prof. Manfred Kaltenbacher, Prof. Werner Mack and Prof. Alois Steindl.

Deutsche Kurzfassung

Diese Arbeit behandelt Ansätze zur Untersuchung nichtlinearer Systeme unter Parametererregung (PE). PE bedeutet, dass mindestens ein Parameter des Systems zeitvariant ist. Das beeinträchtigt die Stabilität der Ruhelage des Systems. Innerhalb bestimmter Frequenzbänder der PE kann die Ruhelage instabil sein. Bei solchen PE Frequenzen treten Schwingungen auf, die nur durch Nichtlinearitäten des Systems in ihrer Amplitude begrenzt sind. Im Gegensatz dazu gibt es andere PE Frequenzbänder, innerhalb derer die Ruhelage des Systems weiter stabilisiert wird. Dies geschieht durch einen Effekt, der die Schwingungsenergie periodisch in stärker gedämpfte Schwingungsmoden transferiert.

Ist die Ruhelage instabil, wird sich das System von ihr entfernen und verzweigten Grenzzyklen zustreben, falls solche existieren. Im Rahmen dieser Arbeit werden Ansätze aufgezeigt, wie diese Grenzzyklen analytisch, semianalytisch und numerisch untersucht werden können. Es wird auch gezeigt, wie die Stabilität dieser Zustände analysiert werden kann. Anhand dieser Ergebnisse wird demonstriert, wie nichtlineare PE Systeme modifiziert werden können, um ihre Eigenschaften zu ändern und ihre Leistung zu verbessern.

Ein wesentliches in dieser Arbeit dargestelltes Ergebnis ist ein neuartiger Ansatz nichtlineare PE Zweifreiheitsgradsysteme in Instabilitätsbereichen der Ruhelage mit Einfreiheitsgradmodellen zu nähern. Diese Näherung ermöglicht auch die analytische Beschreibung des Verhaltens solcher Systeme in diesen Bereichen. Dadurch können kritische Systemparameter und ihr Wirken auf das Verhalten des Systems erkannt werden.

Diese Ergebnisse werden unterstützt durch numerische Simulationen an entscheidenden PE Frequenzen. Außerdem werden beispielhaft verschiedene mikroelektromechanische Systeme betrachtet, bei denen die erzielten Ergebnisse angewendet werden können.

Der hauptsächliche Nutzen der Arbeit liegt darin nichtlineare PE Mehrfreiheitsgradsysteme einfacher beschreiben und daher effizienter gestalten zu können. Sie bietet damit einen einfachen Zugang PE Systeme mit mindestens zwei Freiheitsgraden zu realisieren und eröffnet somit die Möglichkeit Parameterkombinationsresonanzen und Parameter Anti-Resonanzen zu nutzen.

Schlagwörter: Parametererregte Schwingungen, Parameterantiresonanz, Stabilität, Nichtlineare Dynamik, Mikroelektromechanische Systeme, Quasi-modale Transformation

Abstract

This thesis is about investigating parametric excitation (PE) in non-linear systems. PE systems are characterised by at least one system parameter which varies over time. This has an impact on the stability of the system's rest position. Within certain PE frequency intervals the system's rest position is unstable leading to vibrations only limited by non-linearities. Whereas other intervals may exist at which the rest position is further stabilised by an effect periodically shifting the vibrations' energy to more strongly damped modes.

If the rest position is unstable, the system is repelled by this state. If a bifurcated limit cycle exists, the system is attracted towards this state. This thesis presents approaches to investigate these limit cycles analytically, semi-analytically and numerically. It is shown how to analyse the stability of these states. Based on these findings it is demonstrated how to tune non-linear PE systems in order to change their characteristics and to improve their performance.

A major outcome presented in this thesis is a novel approach to a model reduction to one degree of freedom for two degree of freedom non-linear PE systems within instability intervals of the rest position. This approach also allows to state analytic results for the behaviour of such systems at these instability intervals. Thus critical system parameters can be identified and insights into the dependence of the system's behaviour on these parameters is provided.

The results are supported by numerical simulations at specific PE frequencies. Examples are given showing the application of the research results to microelectromechanical systems.

These findings allow to approximate and hence to design nonlinear PE MDOF systems more easily. Thus they encourage to take advantage of PE effects only available in systems with at least two degrees of freedom: parametric combination resonances and parametric anti-resonances.

Keywords: parametrically excited vibrations, parametric anti-resonance, stability, non-linear dynamics, microelectromechanical systems, quasi-modal transformation

Contents

Acknowledgements	III
Deutsche Kurzfassung	IV
Abstract	V
List of Symbols	VIII
1 Introduction	1
1.1 Objectives and Motivation	1
1.2 Overview	2
1.3 Original Contributions	3
2 Parametric Excitation of Non-linear Systems: Effects and Methods of Investigation	5
2.1 Effects of Parametric Excitation	5
2.1.1 Parametric Resonances	5
2.1.2 Parametric Anti-Resonances	7
2.2 Methods for Solving Non-linear ODEs	9
2.2.1 Homotopy Method	9
2.2.2 Continuation Method	10
2.3 Stability Analysis of Time-periodic Systems	11
2.3.1 Averaging Methods	11
2.3.2 Floquet's Method	11
3 Analytical Investigations of One and Two Degree of Freedom Parametrically Excited Non-Linear Systems	14
3.1 One Degree of Freedom System	14
3.1.1 Modelling	14
3.1.2 Normalisation	15
3.1.3 Analytical and Semi-Analytical Investigation of the Behaviour at Parametric Resonances	16
3.1.4 Stability Analysis and Identification of the Type of the Bifurcations	24

3.2	Two Degree of Freedom System	27
3.2.1	Modelling	27
3.2.2	Modal Analysis	29
3.2.3	Quasi-Modal Transformation of the Equations of Motion	30
3.2.4	Analytical and Semi-Analytical Investigation of the Behaviour at Parametric Resonances	34
4	Numerical Investigations of One and Two Degree of Freedom Parametrically Excited Non-Linear Systems	39
4.1	Numerical Investigations of the One Degree of Freedom System	40
4.1.1	Numerical Results by a Continuation Method	42
4.1.2	Poincaré Maps and Borders of Basins of Attraction	45
4.2	Numerical Investigations of the Two Degree of Freedom System	54
4.2.1	Numerical Results by a Continuation Method	57
4.2.2	Poincaré Maps and Borders of Basins of Attraction	63
5	Manipulating the Characteristics of a One and a Two Degree of Freedom Para- metrically Excited Non-Linear System	75
5.1	Manipulating the Characteristics of the 1DOF System	75
5.1.1	Steady Parametric Excitation	76
5.1.2	Non-steady Parametric Excitation	81
5.2	Manipulating the Characteristics of the 2DOF System	86
5.2.1	Steady Parametric Excitation	86
5.2.2	Non-steady Parametric Excitation	96
5.3	Achievements of Manipulating the Characteristics	98
6	Applications	99
6.1	MEMS Energy Harvester for Health Monitoring	99
6.2	MEMS Load Cell	102
6.3	MEMS Bandpass Filter for Electric Signals	104
7	Conclusion	107
	Bibliography	108

List of Symbols

Rarely used symbols and meanings different from the ones listed here are explained where they occur. Vectorial quantities are generally named with bold small letters. Matrix quantities are named with bold capital letters. Elements of vectors or matrices are named with corresponding non-bold letters and are not listed redundantly here.

General Conventions

o	scalar
\boldsymbol{o}	vector
\boldsymbol{O}	matrix

Notations

\mathbb{N}	set of real numbers
\approx	approximately
i	$\sqrt{-1}$, imaginary unit
$\Re\{ \}$	real part of a complex number
$\Im\{ \}$	imaginary part of a complex number
$\mathbf{1}$	identity matrix of appropriate size
\boldsymbol{O}^T	transpose of \boldsymbol{O}
\boldsymbol{O}^{-1}	inverse of \boldsymbol{O}
$\dot{(\)}$	derivative with respect to time t
$(\)'$	derivative with respect to eigentime τ
$\bar{(\)}$	$\frac{1}{T} \int (\) dt$, average over one period

Symbols

c_{ij}	damping constant of a damper between body i and body j
k_{ij}	stiffness constant of a spring between body i and body j
m_i	mass of body i
t	time
x_i	degree of freedom (DOF), translational displacement of body i
z_i	quasi-modal displacement of body i
δ	proportionality factor of damping and stiffness constants
ζ_i	quasi-modal damping constant of i th quasimode
κ^2	nonlinearity parameter
λ	complex eigenvalue
ϱ_n	$\text{eig}(\mathbf{R})$, Floquet multiplier of n th fundamental solution
σ	detuning factor of the parametric excitation frequency Ω
τ	eigentime
ψ	phase shift
ω_i	natural angular frequency of i th quasimode
Ω	parametric excitation frequency
φ	eigenvector
\mathbf{C}	damping matrix
\mathbf{J}	Jacobian
\mathbf{K}	stiffness matrix
\mathbf{M}	mass matrix
\mathbf{R}	monodromy matrix
\mathbf{Z}	modal damping matrix of a non-parametrically excited system
Λ	spectrum
Φ	modal matrix of a non-parametrically excited system

1 Introduction

1.1 Objectives and Motivation

The destabilising effect on a system's rest position caused by time-variant parameters is known since the late 19th century. It was first studied in detail by the French mathematician A. M. G. Floquet. The majority of research on *parametric excitation* (PE) still addresses systems which suffer from PE. In those systems PE is an undesired effect and may endanger safe operation. Typical examples for technical systems which suffer from PE are pantographs (e.g. [1]), wind-turbines (e.g. [2]) and asymmetric rotors (e.g. [3]).

PE vibrations often require attention, since they differ significantly from externally excited (forced) vibrations: First, while vibrations increase linearly over time at an ordinary resonance, they increase exponentially over time at a so-called *parametric resonance* (PR)—an instability of a system's rest position caused by PE. Second, the vibrations' amplitudes at PRs are only limited by non-linearities which in most technical systems are small. Thus vibration amplitudes generally are much larger at PRs than in ordinary resonance cases. Third, PRs are very narrow compared to ordinary resonances, but even low degree of freedom systems may experience multiple PRs.

Yet, from the perspective of PE the methods for investigating such systems are rather simple. Since the system is designed to be operated at a rest position of the PE induced vibrations, linearising the governing equations of motion is in general possible. A stability analysis of this rest position gives answer to the questions at which parameter regimes the system can be operated safely.

It took almost a hundred years to realise the possibilities available by utilising PE. The effects described above definitely complicate the design and operation of certain systems. But for other systems the same effects offer great potential to outperform conventional systems. In addition, A. TONDL discovered an effect of enhanced damping by PE in multi degree of freedom (MDOF) systems by the end of the 20th century [4]. This effect enables to stabilise systems (e.g. [5]). In particular, this is beneficial for systems which otherwise would have an unstable state of operation. Such instabilities may arise from self-excitation which can be caused by fluid-excitation or stick-slip effects [6].

The increasing computational power available and steadily improved user friendly software have led to a better understanding and hence to a growing number of systems actively using PRs in the beginning of the 21st century. However, for MDOF systems little progress has been made regarding both analytical and numerical methods for investigation. Partly this is caused by the problem of choosing a meaningful reduction of the

system's phase space to investigate and display the results. The *quasi-modal* reduction of the phase space presented in this thesis solves this problem by reducing MDOF models to one degree of freedom (1DOF) models at PR. This enables to investigate non-linear MDOF PE systems analytically and to display the results of analytical and numerical investigations.

1.2 Overview

The tasks outlined above are performed in seven chapters about which an overview is given here. A number of methods for investigating a certain class of systems—non-linear one and two degree of freedom PE systems—are presented.

Some of the research outcomes have very general character and can be applied to all PE systems. Thus they are presented in the introductory Chapter 2 among methods taken from references. To the contrary, some findings from references are so specific that they have to be illustrated in subsequent chapters among own findings. The outcomes of this thesis mean empowering researchers to extend systems from one to more degrees of freedom exploiting beneficial effects. To exemplify these effects, existing systems have to be taken from references as examples to demonstrate the advantages of more degrees of freedom.

This mix of knowledge from references and own contributions demands for clarification. A list of original contributions is given in the following section together with clarifying which methods and results are taken from references. In this section, regardless of where the information comes from, an overview is given about the topics presented in this thesis.

First, in Chapter 2 the principle effects of PE and the methods to investigate the behaviour caused by these effects are explained. These include methods for finding solutions of non-linear differential equations in Section 2.2 and methods for determining the stability of those solutions in Section 2.3.

In Chapter 3 1DOF and 2DOF non-linear PE systems are investigated analytically and semi-analytically. First, the 1DOF system is modelled in Section 3.1.1, then normalised in Section 3.1.2 and investigated analytically employing an averaging method in Section 3.1.3. Also, the stability of the found limit cycles is discussed in Section 3.1.4. After modelling the 2DOF system in Section 3.2.1 the system can be quasi-modally transformed to 1DOF systems—one for each PR. This allows to apply the findings from Section 3.1.

The obtained results are validated numerically in Chapter 4. This also demonstrates how to exploit the quasi-modal transformation of the phase space for creating meaningfully reduced spaces in which the results can be presented comprehensively. In addition, basins of attraction of the investigated systems' states are evaluated numerically in Section 4.1.2 and Section 4.2.2. Aspects of these outcomes regarding the safety of operation at certain states are discussed.

Chapter 5 illustrates approaches to tuning systems to a better performance and desired characteristics employing the results from Chapter 3 and Chapter 4. Similar to the

previous chapters this one is also divided discussing 1DOF and 2DOF systems separately. Each section starts discussing systems undergoing PE with a constant amplitude in Section 5.1.1 and Section 5.2.1, respectively. Subsequently the cases of transient PE amplitudes are analysed in Section 5.1.2 and Section 5.2.2. The results of this chapter are summarised in Section 5.3.

Chapter 6 introduces three microelectromechanical systems (MEMSs) which take advantage of certain effects of PE to outperform standard systems. In three sections first each system is explained. It is shown which features of the PE are significant for the system's performance. Referring to Chapter 5, possibilities of tuning the system are illustrated. Finally, the consequences of the extensions from 1DOF to 2DOF systems is discussed. The benefits by applying the results from Chapter 3 and Chapter 4 to the design process are depicted.

Finally Chapter 7 outlines and discusses the achievements presented in this thesis. The practical value is pointed out. Furthermore, directions and ideas for future work are given.

1.3 Original Contributions

This section lists the original contributions which can be found in this thesis. Contributions from references are indicated as such where they are explained.

Stability analysis of time-periodic systems based on Floquet's theorem is anything but new. However, few works have addressed the relation between the results of different methods to construct the monodromy matrix. Two different methods, one deriving the monodromy matrix by integration over the vibration's period and one by integration over the PE period, are compared in Section 2.3.2. The relation between the eigenvalues of the monodromy matrix of each approach is revealed. A way to transform both sets of eigenvalues into each other is illustrated.

Analytical and numerical investigations of 1DOF non-linear PE systems as modelled in Section 3.1.1 at PRs already were presented in RHOADS ET AL. [7]. However, the phase shift of the limit cycles had not been investigated numerically which is done in Section 4.1. Also, RHOADS ET AL. did not interrogate from which step of the approximation for the analytical investigation the degeneration of the branches comes from, so that in difference to the numerical results the branches are not closed loops. Employing a semi-analytical approach this phenomenon is explained in Section 3.1.3 by neglecting the damping being present in the system.

Nonetheless, so far these are all supplements of already published research. Entirely new perspectives presented in this thesis are the analytical, semi-analytical and numerical studies of 2DOF non-linear PE systems in Section 3.2.4, Section 4.2 and Section 5.2. A major aspect is the quasi-modal transformation of MDOF PE systems, which was first published in KNIFFKA [8] and first applied to non-linear systems in this thesis. This transformation is employed for a novel approach to a model reduction in Section 3.2.4. This quasi-modal reduction does not only allow one to apply the analytical results of 1DOF non-linear PE systems on 2DOF systems, but also enables to depict numerical results graphically (see Section 4.2 and Section 5.2).

2 Parametric Excitation of Non-linear Systems: Effects and Methods of Investigation

In this chapter the basics of both the effects of PE and the methods to investigate these effects are explained. A simple academic system is introduced in Section 2.1 for which certain effects are demonstrated specifically. The first section exemplifies the results of PE on the stability of linear and non-linear systems' rest positions. Section 2.2 addresses the task of finding coexisting solutions of non-linear PE differential equations, while Section 2.3 is about determining the stability of those solutions.

2.1 Effects of Parametric Excitation

A system is subject to PE, if it can be modelled as

$$\dot{x} = f(x, t) = A(x, t)x, \quad (2.1)$$

where x is a state vector and $A(x, t)$ is a possibly non-linear, time-variant system matrix. The abbreviation $\dot{(\)}$ denotes a time derivative. Note the absence of any non state dependent terms such as $g(t)$. The system is not excited by external loads. Here only time-periodic systems are discussed, so that

$$A(x, t) = A(x, T + t) \quad (2.2)$$

with T the period of the variation of the system's parameters. Depending on the value of this period, the system's rest position may be destabilised or stabilised in which case the system is attracted towards the rest position faster from a disturbed state. Both cases are discussed in this section, consequences for technical systems are explained and examples are given.

2.1.1 Parametric Resonances

According to the vast literature on Mathieu's equation and related problems (e.g. [9]) the trivial solution of Eq. (2.1) (the system's rest position) may be unstable for a PE frequency

$$\Omega_{\text{PR},i,n} = \frac{2\omega_i}{n}, \quad \forall n \in \mathbb{N}. \quad (2.3)$$

Here ω_i is a natural angular frequency of the system. Such an instability of the trivial solution is called parametric resonance (PR). The system is repelled from the trivial state starting to oscillate with amplitudes increasing exponentially over time. In addition, for

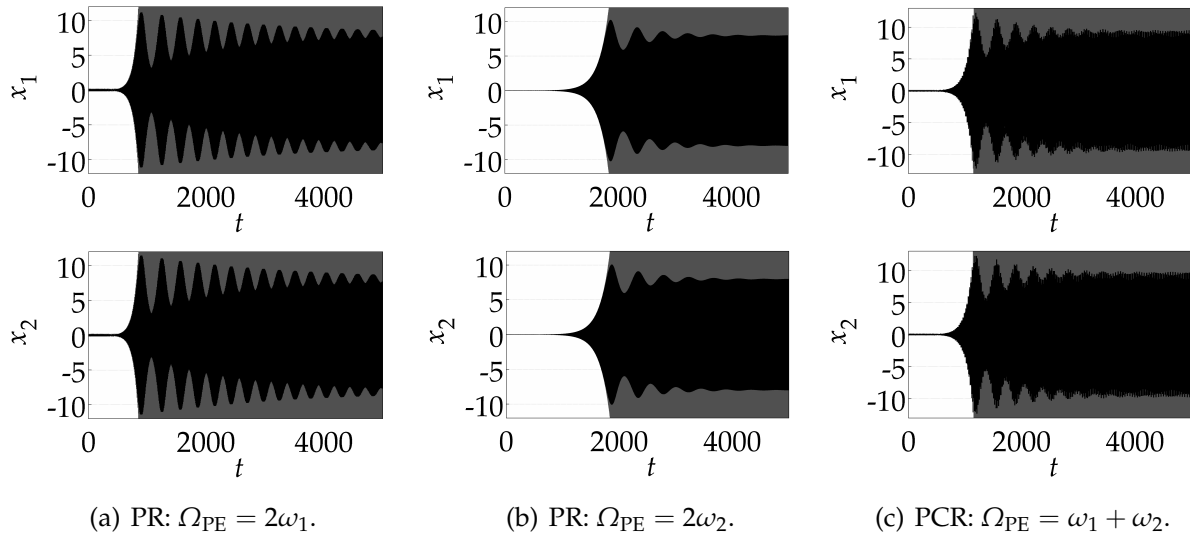


Figure 2.1: Increasing vibrations at PRs and PCR. Grey: linearised equations of motion; black: non-linear equations of motion.

MDOF systems parametric combination resonances (PCRs) may occur for PE frequencies of

$$\Omega_{\text{PCR},ij,n} = \frac{\omega_i + \omega_j}{n}, \quad \forall n \in \mathbb{N}, \quad (2.4)$$

where ω_i and ω_j both are natural angular frequencies of the system. Whether a PR or a PCR occurs at a frequency $\Omega_{\text{PCR},ij,n}$ depends on the damping being present.

Different to ordinary resonance cases, at PRs the amplitudes of the vibrations do not increase linearly over time but exponentially. Also, PRs are narrow compared to ordinary resonance cases. In addition, destabilising the rest position and forcing the system into bifurcated limit cycles means an instant change of the amplitudes in the frequency domain.

For illustration purposes the following academic dimensionless system is introduced

$$\begin{aligned} \ddot{\mathbf{x}} + \begin{pmatrix} 0.002 & -0.001 \\ -0.001 & 0.002 \end{pmatrix} \dot{\mathbf{x}} + \begin{pmatrix} 2 + 0.1 \cos(\Omega_{PE}t) + 0.001x_1^2 & -1 \\ -1 & 2 \end{pmatrix} \mathbf{x} = \mathbf{0} \\ \Rightarrow \begin{pmatrix} \dot{\mathbf{x}} \\ \ddot{\mathbf{x}} \end{pmatrix} = \begin{pmatrix} 0 & 0 & 1 & 0 \\ 0 & 0 & 0 & 1 \\ -2 - 0.1 \cos(\Omega_{PE}t) + 0.001x_1^2 & +1 & -0.002 & +0.001 \\ 1 & -2 & +0.001 & -0.002 \end{pmatrix} \begin{pmatrix} \mathbf{x} \\ \dot{\mathbf{x}} \end{pmatrix}. \end{aligned} \quad (2.5)$$

This system is parametrically excited by the term $0.1 \cos(\Omega_{PE}t)x_1$ with the angular PE frequency Ω_{PE} . Also, it is non-linear due to the term $0.001x_1^3$. The natural frequencies of the linearised system are $\omega_1 = 1$ and $\omega_2 = 1.7321$. The corresponding natural modes are $\boldsymbol{\varphi}_1 = [1, 1]^T$ and $\boldsymbol{\varphi}_2 = [-1, 1]^T$. The damping is not sufficiently large to stabilise the rest position $[\mathbf{x}, \dot{\mathbf{x}}]^T = \mathbf{0}$ at the PRs $\Omega_{PE} = 2\omega_1$, $\Omega_{PE} = 2\omega_2$ and the PCR $\Omega_{PE} = \omega_1 + \omega_2$ within significant intervals. Due to the non-linear stiffness, the vibrations' amplitudes are limited at PR (black graphs in Fig. 2.1). Without such non-linearities the amplitudes would increase infinitely at PR (grey graphs in Fig. 2.1).

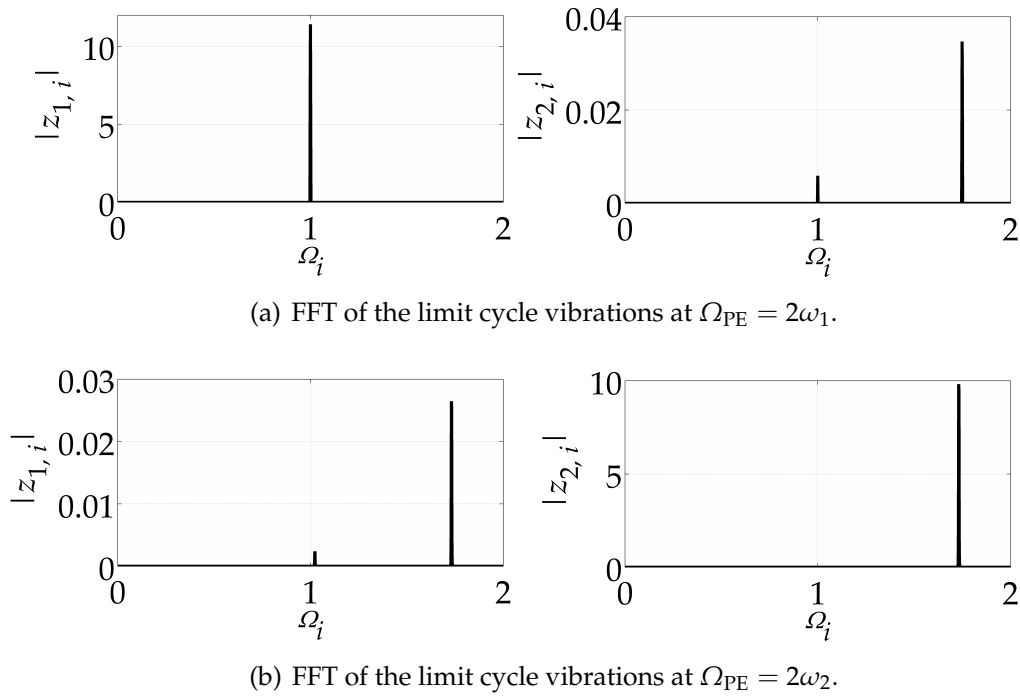


Figure 2.2: FFT of the limit cycles vibrations of the system Eq. (2.5) at both PRs.

The vibrations look the same for both degrees of freedom x_1 and x_2 at each PR and at the PCR. In fact, at PR $\Omega_{PE} = 2\omega_1$ the vibrations are approximately identical, whereas at PR $\Omega_{PE} = 2\omega_2$ they have the same amplitude but are phase-shifted by π . This is caused by the system's natural modes which both have entries of the same magnitude. This effect is explained in detail in Section 3.2.4.

At PR mainly the mode i is excited which corresponds to the PR frequency $\Omega_{PR,n} = \frac{2\omega_i}{n}$. Likewise, for PCRs with the centre frequency $\Omega_{PCR,n} = \frac{\omega_i + \omega_j}{n}$ both modes i and j are excited (see [10, 11] for example). Inspecting the vibrations at the PRs in the frequency domain, this effect is very clear for the system Eq. (2.5) (see Fig. 2.2).

At PR $\Omega_{PE} = 2\omega_1$, the amplitudes of the second mode z_2 are at maximum 0.3% of the amplitude of the first mode z_1 (see Fig. 2.2(a)). The same holds for the PR $\Omega_{PE} = 2\omega_2$: the amplitudes of the first mode z_1 are at maximum 0.27% of the amplitude of the second mode z_2 (see Fig. 2.2(b)).

2.1.2 Parametric Anti-Resonances

In addition, for MDOF systems it is possible not only to destabilise the rest position but also to enhance the energy dissipation when oscillating around the rest position. Thus the system can be brought to rest faster from a perturbed state at certain PE frequencies

$$\Omega_{PAR,ijn} = \frac{|\omega_i - \omega_j|}{n}, \quad \forall n \in \mathbb{N}. \quad (2.6)$$

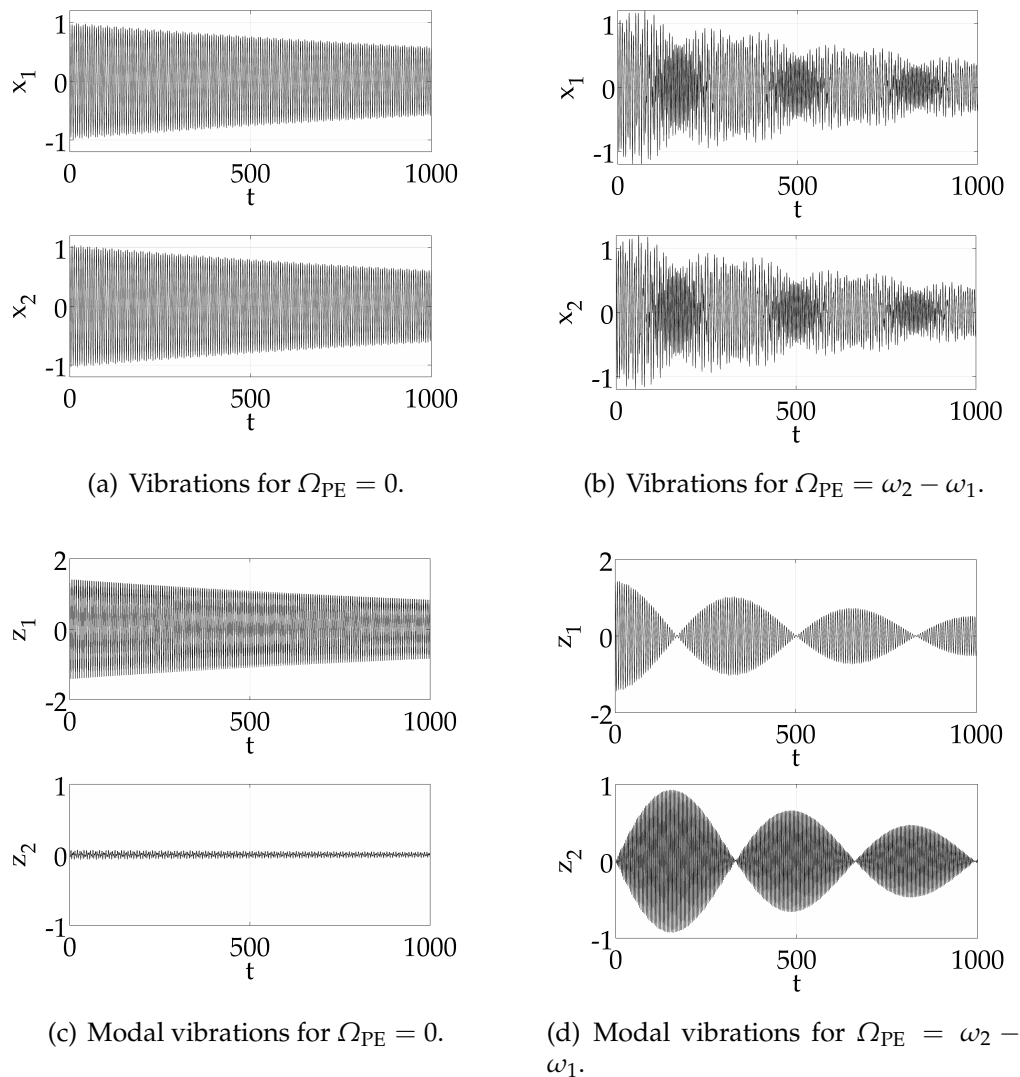


Figure 2.3: Vibrations and modal vibrations at $\Omega_{PE} = 0$ and $\Omega_{PE} = \omega_2 - \omega_1$. The faster dissipation of energy in (b) and (d) can be explained by the more efficient use of the higher modal damping of the second mode z_2 .

This effect was first discovered by TONDL [4] and is called parametric anti-resonance (PAR). The phenomenon is caused by periodically shifting energy between the modes i and j . Hence the higher modal damping of the higher mode is exploited more effectively [12].

The system Eq.(2.5) experiences a PAR at $\Omega_{PE} = \omega_2 - \omega_1 = 0.7321$. At this PAR 35% more energy is dissipated within the simulated time interval than at $\Omega_{PE} = 0$. The continuous energy transfer between both modes z_1 and z_2 becomes obvious in **Fig. 2.3d**. On average the amplitude of the second mode is much larger than for the non-PE system ($\Omega_{PE} = 0$) (compare **Fig. 2.3(c)** and **(d)**).

This effect of enhanced damping can be used to stabilise systems which are at risk of becoming unstable at their operational state [6, 13]. Using PE an open loop control can be designed stabilising systems which, for example, undergo self-excitation.

2.2 Methods for Solving Non-linear ODEs

Different to linear equations, non-linear equations do not have unique solutions. This also applies to non-linear differential equations. The solutions of such equations can be attracted by two different kind of states: *fixed points* (equilibria) and *limit cycles*. Because of their attracting behaviour they are called *attractors*. Attractors can be stable or unstable¹. Cycles are closed periodic orbits in the phase space. *Limit cycle* means that in a certain neighbourhood no other cycles exist [14].

Due to possible coexisting solutions, for non-linear differential equations the solutions cannot be found in their entirety by an ansatz in contrast to linear differential equations. One approach to deal with this problem analytically is to average the differential equations over one period of the limit cycle. The results are average changes of the phase parameters which can be set to zero in case of a limit cycle. This procedure is explained in more detail in Section 3.1.3. The emerging algebraic set of equations can either be solved analytically or can be evaluated employing numerical path-following methods. Alternatively, the original non-linear differential equations can be investigated by path-following methods directly.

Two numerical path-following methods for investigating non-linear equations are described in the following sections.

Because the limit cycle's period T^* is not known, for finding limit cycles numerically, Eq. (2.1) has to be scaled to a fixed interval, e.g. $[0, 1]$ or $[0, 2\pi]$. This way $x(t) = x(t + T^*)$ can be stated easily exploiting the interval's borders. This set of equations needs another constraint to have a unique solution. A common choice for a third variable is the L2-norm $x^2 + \dot{x}^2$ of the solution of Eq. (2.1). The path following packages AUTO [15] and MATCONT [16] utilise

$$\int_0^1 x^T(t)v dt = 0, \quad (2.7)$$

where v is the known tangent vector of a previously calculated limit cycle. This condition aims at selecting the solution with the smallest phase difference to the previous solution. In either case a boundary value problem is formulated.

To find the states $x(0)$ Newton-like methods are in use, which sensitively depend on the start value. In the following, two methods for finding these start values are presented: the homotopy method and the continuation method. These methods can also be applied for finding the solutions of an algebraic set of equations with a free parameter (see Chapter 3).

2.2.1 Homotopy Method

Homotopy is a continuous transition from one problem to another. The homotopy method embeds the original problem g_1 and a modified version g_0 of this problem in the family

$$g(x, \alpha) = 0 \quad (2.8)$$

¹In this thesis "stable", "stability" etc. always refers to Lyapunov stability (see Section 2.3).

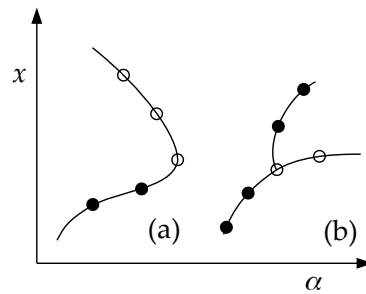


Figure 2.4: Convergence problems of the homotopy method (a) and the continuation method (b) at reversal points and bifurcations, respectively.

so that

$$g(x, 0) = g_0, \quad (2.9a)$$

$$g(x, 1) = g_1. \quad (2.9b)$$

Problems of this family for $\alpha \in [0, 1]$ are solved for $\alpha = \alpha_i$ on sufficiently small intervals $[\alpha_i, \alpha_{i+1}]$. As a start value for x_{i+1} the value x_i or a related value is used. With the method employed in Chapter 3 the start value $x_{0,i+1}$ is set to

$$x_{0,i+1} = x_i + (\alpha_{i+1} - \alpha_i) \frac{\partial x}{\partial \alpha}, \quad (2.10)$$

where $\frac{\partial x}{\partial \alpha}$ is computed via

$$f'(x_i, \alpha_i) \frac{\partial x}{\partial \alpha} + \frac{\partial f(x, \alpha)}{\partial \alpha} = 0. \quad (2.11)$$

The Jacobian $f'(x_i, \alpha_i)$ is known from the Newton iteration.

However, if $x(\lambda)$ has reversal points, singular matrices occur for the Newton method when utilising the homotopy method. This means, instead of new states beyond a reversal point, the branch may be followed backwards along the already detected states (see Fig. 2.4(a)) [17].

2.2.2 Continuation Method

This problem can be overcome by a continuation method as implemented in AUTO [15] and the MATLAB-based package MATCONT [16]. In contrast to the homotopy method, a continuation method treats the free parameter α as an unknown parameter which is solved simultaneously. This way the Jacobian of the linearised problem does not become singular at reversal points as for the homotopy method. Instead, the Jacobian becomes singular at bifurcation points where further solutions bifurcate from the followed path. On the one hand this enables to identify bifurcation points. On the other hand the re-

sulting convergence problems of the Newton method or Newton-like method in use may lead to *branch switching*: instead of the original branch a bifurcated path is followed (see Fig. 2.4(b)) [18].

2.3 Stability Analysis of Time-periodic Systems

Not all states found by the methods described above are stable. In the following stability refers to Lyapunov stability [19]. A state x_s is Lyapunov stable, if there is a $\delta > 0$ so that, if

$$|x(0) - x_s| < \delta \quad (2.12)$$

then there is an $\varepsilon > 0$ so that for any $t > 0$

$$|x(t) - x_s| < \varepsilon. \quad (2.13)$$

In general, non-linear systems can be linearised at the state of interest which enables to investigate the Jacobian of the linearised system. A state of a non-linear system is stable if the real parts of the eigenvalues of the Jacobian are negative [19].

However, for PE systems the Jacobian of the linearised system at a certain state is time-variant, since the system parameters are time-variant. Hence the Jacobian's eigenvalues are time-variant and do not give information about the stability. Two different methods to investigate the stability of states of such systems are presented in the following.

2.3.1 Averaging Methods

If the PE system is analysed analytically with averaging methods (see Section 2.2 or Section 3.1.3 for details), the time-periodic set of differential equations is averaged over one period of the vibration leading to a time-constant set of differential equations. This set of differential equations can be linearised and its Jacobian can be evaluated according to the approach outlined above.

2.3.2 Floquet's Method

A method to analyse a state's stability directly without approximating the time-periodic system is to evaluate its *monodromy matrix* \mathbf{R} . The solution of Eq. (2.1)

$$\dot{\mathbf{x}} = \mathbf{f}(\mathbf{x}, t) = \mathbf{A}(\mathbf{x}, t)\mathbf{x}$$

can be assumed to take the form

$$\mathbf{x}(t) = \mathbf{x}_0(t) + \Delta\mathbf{x}(t), \quad (2.14)$$

where $\mathbf{x}_0(t) = \mathbf{x}_0(t + T^*)$ is a cycle with a constant period T^* and $\Delta\mathbf{x}(t)$ is a small additional disturbance. Because of this periodicity the solution $\mathbf{x}(t)$ only is Lyapunov stable, if

$$\mathbf{x}(t + T^*) \leq \mathbf{x}(t). \quad (2.15)$$

With $x_0(t)$ being periodic, the differential equation can be written in terms of the disturbance Δx as

$$\dot{\Delta x} = \dot{x} - \dot{x}_0 = A(x, t)\Delta x. \quad (2.16)$$

The dependence of fundamental solutions ΔX of the disturbance Δx on time can be formulated employing the monodromy matrix R^* , i.e.

$$\Delta X(t + T^*) = \Delta X(t)R^*. \quad (2.17)$$

Different to the Jacobian, the monodromy matrix R^* , which T^* -periodically maps sets of fundamental solutions, is time-constant. With Eq. (2.17) the stability condition Eq. (2.15) becomes

$$|\varrho_n^*| \stackrel{!}{\leq} 1, \quad (2.18)$$

with ϱ_n^* the eigenvalues of the monodromy matrix R^* . These eigenvalues are called *characteristic multipliers* or *Floquet multipliers* referring to the French mathematician A. M. G. Floquet.

However, for this method the period T^* of the cycle x_0 has to be known. Approximating the period T^* can be achieved efficiently via harmonic balancing, which for example is implemented in the MATLAB-based path following package MANLAB [20].

A computationally less expensive way to investigate the stability of time-periodic systems is based on the PE period T instead of the vibration's period [21]: If $X(t)$ is a set of fundamental solutions of Eq. (2.1), $X(t + T)$ also is a set of fundamental solutions, because choosing $\tau = t + T$ yields

$$\frac{dx}{d\tau} = A(\tau - T)x = A(\tau)x. \quad (2.19)$$

This enables one to map sets of fundamental solutions in analogy to Eq. (2.17), i.e.

$$X(t + T) = X(t)R. \quad (2.20)$$

Hence x is stable, only if

$$|\varrho_n| = |\text{eig}(R)| \leq 1. \quad (2.21)$$

Because the monodromy matrix R compares sets of solutions with respect to the period T of the PE, the period T^* does not need to be known. For deriving R numerically, x has to be integrated over one period T with an independent set of initial conditions. Because being computationally less expensive this approach commonly is favoured instead of deriving the monodromy matrix with respect to the vibrations period. It is implemented in software packages like MATCONT [16].

The essential difference of the two different sets of Floquet multipliers is that the multipliers ϱ_n describe the behaviour of the system with regard to the PE period T , while the Floquet multipliers ϱ_n^* describe the behaviour with regard to the period T^* of the cycle. However, both Floquet multipliers are related to each other [11]. The envelope function of the n -th fundamental solution $x_n(t)$ can be defined utilising either set of Floquet multipliers, i.e.

$$|\varrho_n|^{t/T} = |\varrho_n^*|^{t/T^*}. \quad (2.22)$$

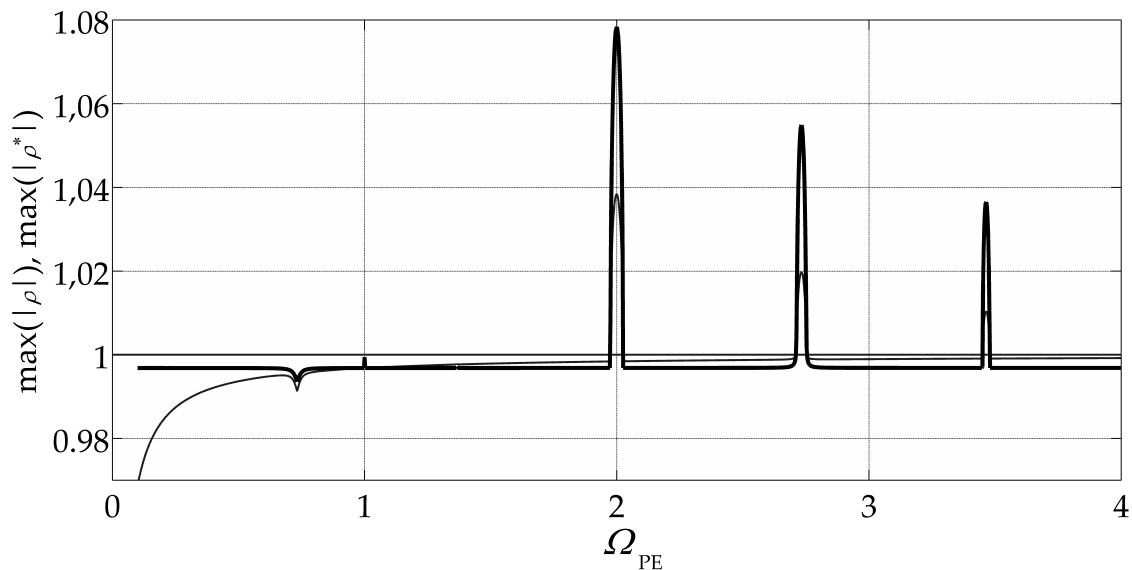


Figure 2.5: Maximum Floquet multipliers $\max(|q|)$ (thin) and $\max(|q^*|)$ (bold) depending on the PE angular frequency Ω_{PE} . The value 1 indicates the stability limit.

Hence the Floquet multipliers can be converted to each other by

$$|q_n| = |q_n^*|^{T/T^*} \Leftrightarrow |q_n^*| = |q_n|^{T^*/T}. \quad (2.23)$$

The maxima of both Floquet multipliers $|q_n|$ and $|q_n^*|$ for the rest position of the system Eq. (2.5) are depicted in **Fig. 2.5**. Five PE frequency intervals become distinct. Three of them are indicated as unstable ($\max(|q_n|) > 1$). These are the PRs $\Omega_{PR,1,1} = 2\omega_1 = 2$ and $\Omega_{PR,2,1} = 2\omega_2 = 3.46$ for which the time series are displayed in **Fig. 2.1**. The PR $\Omega_{PR,1,2} = \omega_1 = 1$ candidate is noticeable but does not destabilise the rest position. The tiny notch at $\Omega_{PAR,12,1} = \omega_2 - \omega_1 = 0.73$ indicates the PAR for which the time series are displayed in **Fig. 2.3**.

Note that $\lim_{\Omega_{PE} \rightarrow 0} (\max(|q_n|)) = -\infty$ due to the normalisation to $T = 2\pi/\Omega_{PE}$ which becomes indefinitely large for $\Omega_{PE} \rightarrow 0$. Hence the entries of $X(t+T)$ and thus the entries of R become indefinitely small. Not only at small Ω_{PE} the diagram becomes hard to interpret. The values of the Floquet multipliers q_n do not necessarily coincide with a faster or slower decrease of the vibrations of the system. They only give qualitative information about the stability but must not be interpreted as a growth or decay rate for the time signal. On the contrary, the Floquet multipliers q_n^* can be interpreted quantitatively. In fact

$$\max(|q_n^*|) \Big|_{\Omega_{PE}=0} = \max(e^{-\omega_i \zeta_i T}), \quad (2.24)$$

where ζ_i is the i -th modes modal damping. If the Floquet multipliers q_n are computed, the conversion Eq. (2.23) can be employed for quantitatively interpretable results.

3 Analytical Investigations of One and Two Degree of Freedom Parametrically Excited Non-Linear Systems

One and two degree of freedom systems with PE are introduced in this chapter and investigated both analytically and semi-analytically. Approximations describing their characteristics at parametric resonance are given, which are validated numerically in Chapter 4.

3.1 One Degree of Freedom System

In this section a 1DOF non-linear PE system is introduced, modelled and analysed (see **Fig. 3.1**). The equation of motion is derived in Section 3.1.1. This equation is normalised to become dimensionless in Section 3.1.2. Limit cycles of this equation are approximated analytically and semi-analytically using an averaging method in Section 3.1.3. The section concludes with a stability analysis and an identification of the type of the bifurcations (Section 3.1.4).

3.1.1 Modelling

We consider a lumped mass model as follows (see **Fig. 3.1**): a rigid body with mass m is linked to the inertial reference frame via two springs with the non-linear stiffness parameters $k_b(x)$ and $k(x, t)$ and a viscoelastic damper with the damping constant c .

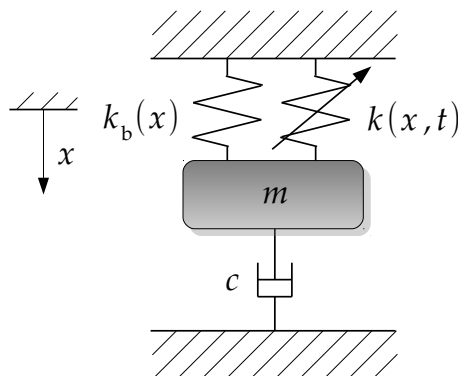


Figure 3.1: Mechanical lumped mass model of the 1DOF system: mass m , stiffness parameters $k_b(x)$ and $k(x, t)$, damping constant c .

Table 3.1: Parameters of Eq. (3.2) as used in numerical analyses

Parameter	Symbol	Value	Unit
Mass	m	$1.22 \cdot 10^{-10}$	kg
Damping Constant	c	$3.88 \cdot 10^{-8}$	$\text{N m}^{-1} \text{s}$
Linear Stiffness Constant	$k_{b,\text{lin}}$	7	N m^{-1}
Non-linear Stiffness Constant	$k_{b,\text{nonlin}}$	$3.6 \cdot 10^{10}$	N m^{-3}
Linear PE Stiffness Constant	$k_{\text{PE},\text{lin}}$	0.146	N m^{-1}
Non-linear PE Stiffness Constant	$k_{\text{PE},\text{nonlin}}$	$-6.4 \cdot 10^9$	N m^{-3}

The stiffness parameters are

$$k_b(x) = k_{b,\text{lin}} + k_{b,\text{nonlin}}x^2, \quad (3.1a)$$

$$k(x, t) = k_{\text{PE}}(1 + \cos(\Omega_{\text{PE}}t)), \quad (3.1b)$$

$$k_{\text{PE}}(x) = k_{\text{PE},\text{lin}} + k_{\text{PE},\text{nonlin}}x^2. \quad (3.1c)$$

The equation of motion becomes

$$\begin{aligned} m\ddot{x} + c\dot{x} + k_b(x)x + k(x, t)x = \\ m\ddot{x} + c\dot{x} + k_{b,\text{lin}}x + k_{b,\text{nonlin}}x^3 + (k_{\text{PE},\text{lin}}x + k_{\text{PE},\text{nonlin}}x^3)(1 + \cos(\Omega_{\text{PE}}t)) = 0. \end{aligned} \quad (3.2)$$

The abbreviation $(\dot{}) = \frac{d}{dt}$ denotes a time derivative. Note that there is no external excitation. Instead of being excited externally the system undergoes parametric excitation (PE) by the time-periodic stiffness $k(x, t)$ (see Section 2.1).

The system studied here was described in [22], pp.31-41. The values of the parameters used in subsequent numerical investigations are listed in **Tab. 3.1**. The system is a microelectromechanical system (MEMS) with a mass m of $122 \mu\text{g}$. The stiffnesses are accordingly small to realise a natural frequency of 38.5 kHz of the linearised system. Applications and functional principles are presented in Chapter 6. Although its parameters specifically refer to a microsystem, the studies and analyses in this and the following two chapters are fundamental and general. They can be applied to any system which can be modelled as shown in **Fig. 3.1**.

3.1.2 Normalisation

For further analysis it is useful to normalise Eq. (3.2). Thereby the number of parameters is reduced and the equation and its parameters become dimensionless. The analysis of the behaviour of this equation therefore becomes easier and findings more general.

Introducing the eigentime $\tau = \Omega_{\text{PE}}t$ gives the relation

$$\frac{d}{dt} = \Omega_{\text{PE}} \frac{d}{d\tau}. \quad (3.3)$$

Table 3.2: Non-dimensional parameters of Eq. (3.7) and their relation to the physical parameters of the 1DOF system. The values listed here are used for illustrating analytical results and for semi-analytical and numerical investigations.

Non-dimensional Parameter	Symbol	Relation to Physical Par.	Value
Linear PE Parameter	ε_{lin}	$\frac{k_{\text{PE,lin}}}{m \Omega^{*2}}$	0.1197
Non-linear PE Parameter	$\varepsilon_{\text{nlin}}$	$\frac{k_{\text{PE,nlin}} x^{*2}}{m \Omega^{*2}}$	$-5.246 \cdot 10^{-3}$
Damping Ratio	ζ	$\frac{c}{2\sqrt{k} m}$	$6.635 \cdot 10^{-4}$
Non-linearity Parameter	κ^2	$\frac{(k_{\text{b,nlin}} + k_{\text{PE,nlin}}) x^{*2}}{m \Omega^{*2}}$	$2.403 \cdot 10^{-2}$
Natural Angular Frequency	ω_0	$\sqrt{\frac{k_{\text{b,lin}} + k_{\text{PE,lin}}}{m \Omega^{*2}}}$	2.420

Scaling Parameter	Symbol	Value
Frequency Scaling Parameter	Ω^*	10^5 s^{-1}
Displacement Scaling Parameter	x^*	10^{-6} m

Hence Eq. (3.2) becomes

$$m \Omega_{\text{PE}}^2 x'' + c \Omega_{\text{PE}} x' + k_{\text{b,lin}} x + k_{\text{b,nlin}} x^3 + (k_{\text{PE,lin}} x + k_{\text{PE,nlin}} x^3)(1 + \cos(\tau)) = 0, \quad (3.4)$$

where $\frac{d}{d\tau} = ()'$ denotes a differentiation with respect to eigentime τ . Further scaling to reference scaling parameters x^* and Ω^* leads to a dimensionless displacement z and a dimensionless PE frequency Ω :

$$z = \frac{x}{x^*} \Rightarrow x^3 = x^{*3} z^3, \quad (3.5)$$

$$\Omega = \frac{\Omega_{\text{PE}}}{\Omega^*}. \quad (3.6)$$

Substituting in Eq. (3.4) results in

$$z'' + 2\zeta \frac{\omega_0}{\Omega} z' + \left(\frac{\omega_0^2}{\Omega^2} + \frac{\varepsilon_{\text{lin}}}{\Omega^2} \cos(\tau) \right) z + \left(\frac{\kappa^2}{\Omega^2} + \frac{\varepsilon_{\text{nlin}}}{\Omega^2} \cos(\tau) \right) z^3 = 0. \quad (3.7)$$

Here ω_0 is the natural angular frequency of the linearised, non-parametrically excited and undamped system. It is scaled so that $\omega_0 = \frac{\omega_n}{\Omega^*}$, where ω_n is the unscaled natural frequency. The damping ratio is denoted ζ . The parameters ε_{lin} and $\varepsilon_{\text{nlin}}$ determine the amplitude of the PE, κ^2 describes the degree of non-linearity. All relations between dimensionless and physical parameters are listed in **Tab. 3.2**.

3.1.3 Analytical and Semi-Analytical Investigation of the Behaviour at Parametric Resonances

In this section the behaviour of the 1DOF system described in Section 3.1.1 at parametric resonances is analysed analytically and semi-analytically.

Simply averaging Eq. (3.7) by integrating over one period of the PE will result in an autonomous differential equation. Hence a free vibration is predicted. While this is true for most cases of the PE frequency Ω this averaging is unable to predict the behaviour of the system at so-called parametric resonances (PRs) (see Section 2.1). Within these frequency bands the trivial solution of PE systems may become unstable depending on the level of damping present. Bifurcated limit cycles branch at the edges of such PR regions. To predict these bifurcations a more sophisticated averaging method is employed. It gives an approximation of the amplitude and phase shift of the vibrations of the oscillating part of the system in the form of a set of algebraic equations. Under certain restrictions these algebraic equations can be solved analytically. They can also be solved numerically without any further restrictions. Results of both methods are presented and discussed.

To obtain analytical results for the behaviour of the 1DOF system at PR the Krylov-Bogolyubov averaging method is employed. Eq. (3.7) is studied within small bands surrounding a certain PE frequency Ω_0 , which will take on values of PR frequencies in the following analysis. Hence the value Ω_0 of the angular PE frequency Ω will be called the PR frequency. The deviation from Ω_0 is assumed to be very small so that the PE frequency Ω can be written as

$$\Omega = \Omega_0 + \varepsilon\sigma + \mathcal{O}(\varepsilon^2), \quad (3.8)$$

where $\varepsilon \ll 1$ is a small disturbance, which is tuned by the detuning factor σ . Since $\varepsilon \ll 1$ the following expressions can be derived:

$$\frac{1}{\Omega} = \frac{1}{\Omega_0 + \varepsilon\sigma + \mathcal{O}(\varepsilon^2)} = \frac{\Omega_0 - \varepsilon\sigma}{\Omega_0^2 + \mathcal{O}(\varepsilon^2)} \quad (3.9a)$$

$$\Rightarrow \frac{1}{\Omega^2} = \frac{1}{\Omega_0^2} - \frac{2\varepsilon\sigma}{\Omega_0^3} + \mathcal{O}(\varepsilon^2). \quad (3.9b)$$

Substituting Eqs. (3.9) in Eq. (3.7) leads to

$$\begin{aligned} z'' + 2\zeta\eta z' + \eta^2 z + \chi^2 z^3 + \frac{1}{\Omega_0^2} [\varepsilon_{\text{lin}} \cos(\tau) - \varepsilon 2\eta\omega_0\sigma] z + \dots \\ + \frac{1}{\Omega_0^2} [\varepsilon_{\text{nonlin}} \cos(\tau) - \varepsilon 2\chi\kappa\sigma] z^3 + \mathcal{O}(\varepsilon^2, \varepsilon\varepsilon_{\text{lin}}, \varepsilon\varepsilon_{\text{nonlin}}, \zeta\varepsilon_{\text{nonlin}}) = 0. \end{aligned} \quad (3.10)$$

for small disturbances of Ω around Ω_0 and under the constraints $\varepsilon_{\text{lin}} \ll 1$, $\varepsilon_{\text{nonlin}} \ll 1$, $\zeta \ll 1$. Here $\eta = \frac{\omega_0}{\Omega_0}$ is the frequency ratio of the natural frequency ω_0 to the PR frequency Ω_0 and $\chi = \frac{\kappa}{\Omega_0}$ the ratio of κ to the PR frequency Ω_0 .

Introduction of polar coordinates for the non-dimensional displacement z and the non-dimensional velocity v gives

$$z = r \cos(\alpha), v = -\eta r \sin(\alpha). \quad (3.11)$$

The amplitude of the vibration $z(\tau)$ is denoted r and the argument of the harmonic function $\alpha = \eta\tau + \psi$. The kinematic constraint $z' = v$ leads to

$$r' \cos(\alpha) - r \sin(\alpha) \alpha' = -\eta r \sin(\alpha) \quad (3.12a)$$

$$\Leftrightarrow \alpha' = \eta + \frac{r' \cos(\alpha)}{r \sin(\alpha)}. \quad (3.12b)$$

Applying Eqs. (3.12) to the second order differential Eq. (3.10) gives the following set of two first order differential equations:

$$r' = -2\zeta\eta r \sin^2(\alpha) + \frac{1}{\Omega_0^2 \eta} [\varepsilon_{\text{lin}} \cos(\tau) - \varepsilon 2\eta\omega_0\sigma] r \cos(\alpha) \sin(\alpha) + \dots \quad (3.13a)$$

$$+ \left(\frac{\chi^2}{\eta} + \frac{1}{\Omega_0^2 \eta} [\varepsilon_{\text{nonlin}} \cos(\tau) - \varepsilon 2\chi\kappa\sigma] \right) r^3 \cos^3(\alpha) \sin(\alpha),$$

$$\psi' = \frac{r' \cos(\alpha)}{r \sin(\alpha)}. \quad (3.13b)$$

This set of differential equations is now averaged over time, integrating over one period of $z = r \cos(\alpha)$, which is $2\pi/\eta$, giving:

$$\bar{r}' = \bar{r}' = \frac{\eta}{2\pi} \int_0^{\frac{2\pi}{\eta}} r' d\tau, \quad (3.14a)$$

$$\bar{\psi}' = \bar{\psi}' = \frac{\eta}{2\pi} \int_0^{\frac{2\pi}{\eta}} \psi' d\tau. \quad (3.14b)$$

At the first PR $\Omega_0 = 2\omega_0$ (see Section 2.1) Eqs. (3.14) become

$$\bar{r}' = \frac{-4\omega_0^2 \zeta + \varepsilon_{\text{lin}} \sin(2\bar{\psi})}{8\omega_0^2} \bar{r} + \frac{\varepsilon_{\text{nonlin}} \sin(2\bar{\psi})}{16\omega_0^2} \bar{r}^3, \quad (3.15a)$$

$$\bar{\psi}' = \frac{-3\chi\varepsilon\kappa\sigma\bar{r}^2 - 2\varepsilon\omega_0\sigma + 6\chi^2\omega_0^2\bar{r}^2 + \varepsilon_{\text{lin}} \cos(2\bar{\psi}) + \cos(2\bar{\psi})\bar{r}^2\varepsilon_{\text{nonlin}}}{8\omega_0^2}. \quad (3.15b)$$

Note that $(\bar{\cdot})'$ describes the averaged change of the variable over one period of the vibration. For a limit cycle this change has to be zero. To find such limit cycles the equations above are set to zero.

Neglecting the damping ($\zeta = 0$), the solutions are (compare [7]¹)

$$\bar{r}_a = 0 \quad \wedge \quad \bar{\psi}_a = \frac{\arccos\left(\frac{2\omega_0 \varepsilon \sigma}{\varepsilon_{\text{lin}}}\right)}{2}, \quad (3.16a)$$

$$\wedge \quad \bar{\psi}_b = \frac{\pi}{2}(1 + 2k), \quad k \in \mathbb{N} \quad \wedge \quad \bar{r}_b = \pm \sqrt{\frac{4\omega_0 \varepsilon \sigma + 2\varepsilon_{\text{lin}}}{-2\varepsilon_{\text{nonlin}} + 3\kappa^2(1 - \frac{\varepsilon \sigma}{\omega_0})}}, \quad (3.16b)$$

$$\wedge \quad \bar{\psi}_c = \pi k, \quad k \in \mathbb{N} \quad \wedge \quad \bar{r}_c = \pm \sqrt{\frac{4\omega_0 \varepsilon \sigma - 2\varepsilon_{\text{lin}}}{2\varepsilon_{\text{nonlin}} + 3\kappa^2(1 - \frac{\varepsilon \sigma}{\omega_0})}}, \quad (3.16c)$$

$$\wedge \quad \bar{r}_d = \pm \sqrt{\frac{-2\varepsilon_{\text{lin}}}{\varepsilon_{\text{nonlin}}}} \quad \wedge \quad \bar{\psi}_d = \frac{\arccos\left(\frac{3\kappa^2}{\varepsilon_{\text{nonlin}}}\left(\frac{\varepsilon \sigma}{\omega_0} - 1\right) - \frac{2\omega_0 \varepsilon \sigma}{\varepsilon_{\text{lin}}}\right)}{2}. \quad (3.16d)$$

Each pair of amplitudes in Eqs. (3.16b-d) represents the same physical response. Because the frequency ratio $\eta = \frac{\omega_0}{\Omega} = \frac{1}{2}$ the period of $z(\tau)$ is $T = 4\pi$ and hence $\bar{r}_{i+}(\tau) = \bar{r}_{i-}(\tau + 2\pi)$. Eqs. (3.16) do, of course, neither depend on ε nor on σ solely, but always on the product $\varepsilon\sigma$ because Ω was defined as $\Omega = \Omega_0 + \varepsilon\sigma$. To minimise the number of parameters one might introduce an abbreviation like $\varepsilon\sigma = \Delta\Omega$. However, some expressions become even more simple for the 1DOF system, if ε is set to $\varepsilon = \varepsilon_{\text{lin}}$. When it comes to 2DOF systems in the following chapters, keeping both parameters ε and σ is still meaningful, as $\varepsilon\sigma$ is very small and handling σ is more convenient.

The limit cycles with the amplitudes \bar{r}_b, \bar{r}_c branch from the trivial solution $\bar{r} = 0$ when the detuning factor σ becomes

$$\sigma = \mp \sigma_b = \mp \frac{\varepsilon_{\text{lin}}}{2\varepsilon\omega_0} \stackrel{\varepsilon = \varepsilon_{\text{lin}}}{=} \mp \frac{1}{2\omega_0}. \quad (3.17)$$

Whether $\bar{r}_b(\sigma)$ and $\bar{r}_c(\sigma)$ have hardening or softening behaviour with respect to the detuning factor, is determined by the value of the denominators, which can be greater or less than zero at the bifurcation point $\sigma = \pm \sigma_b$. Both branches become purely imaginary when the denominator is zero, i.e. when

$$\sigma = \sigma_{p1/p2} = \left(\frac{\pm 3\varepsilon_{\text{nonlin}}}{3\kappa^2} - 1 \right) \frac{\omega_0}{\varepsilon} \quad (3.18)$$

depending on whether they have hardening or softening characteristics.

If the branches intersect, κ^2 has to take on a value so that:

$$r_1 - r_2 = 0 \Big|_{\sigma} \Big|_{\Re(r_1) > 0 \wedge \Re(r_2) > 0}. \quad (3.19)$$

¹Eqs. (3.16b-d) are equivalent to Eqs. (16-19) and Eqs. (22&23) in [7]. However, a different normalisation with different parameters is chosen in [7].

From the above analysis five different cases of κ^2 can be identified:

- $\boxed{\kappa^2 < -\left|\frac{4\varepsilon_{\text{nl}}\omega_0^2}{3\varepsilon_{\text{lin}}}\right|}$: Both branches have softening characteristics. They do not intersect. Where the trivial solution is unstable, there is only one stable solution with amplitude \bar{r}_c and phase shift $\bar{\psi}_c = 0$ (see **Fig. 3.2, a**).
- $\boxed{-\left|\frac{4\varepsilon_{\text{nl}}\omega_0^2}{3\varepsilon_{\text{lin}}}\right| \leq \kappa^2 < -\left|\frac{4\varepsilon_{\text{nl}}\omega_0^2}{3(\varepsilon_{\text{lin}}+2\omega_0^2)}\right|}$: Both branches have softening characteristics. They intersect. Where the trivial solution is unstable, there is only one stable solution with amplitude \bar{r}_c and phase shift $\bar{\psi}_c = 0$ (see **Fig. 3.2, b**).
- $\boxed{-\left|\frac{4\varepsilon_{\text{nl}}\omega_0^2}{3(\varepsilon_{\text{lin}}+2\omega_0^2)}\right| \leq \kappa^2 < \left|\frac{4\varepsilon_{\text{nl}}\omega_0^2}{3(\varepsilon_{\text{lin}}-2\omega_0^2)}\right|}$: The branch \bar{r}_b has a hardening characteristic, but \bar{r}_c has a softening characteristic. Where the trivial solution is unstable, both branches are stable (see **Fig. 3.2, c**).
- $\boxed{\left|\frac{4\varepsilon_{\text{nl}}\omega_0^2}{3(\varepsilon_{\text{lin}}-2\omega_0^2)}\right| \leq \kappa^2 < \left|\frac{4\varepsilon_{\text{nl}}\omega_0^2}{3\varepsilon_{\text{lin}}}\right|}$: Both branches have hardening characteristics. They intersect. Where the trivial solution is unstable, there is only one stable solution with amplitude \bar{r}_b and phase shift $\bar{\psi}_b = \pi/2$ (see **Fig. 3.2, d**).
- $\boxed{\kappa^2 > \left|\frac{4\varepsilon_{\text{nl}}\omega_0^2}{3\varepsilon_{\text{lin}}}\right|}$: Both branches have hardening characteristics. They do not intersect. Where the trivial solution is unstable, there is only one stable solution with amplitude \bar{r}_b and phase shift $\bar{\psi}_b = \pi/2$ (see **Fig. 3.2, e**).

For the parameters shown in **Tab. 3.2** the amplitudes of the bifurcated limit cycles are approximately symmetric about the line $\sigma = 0$, if the sign of κ^2 is changed. Because of the change of sign of ε_{lin} and ε_{nl} in \bar{r}_b and \bar{r}_c such symmetry is only approximate. For the parameters shown in **Tab. 3.2** the limiting cases of κ^2 take on the values shown in **Tab. 3.3**.

Table 3.3: Numerical values for limit cases of κ^2 according to the parameter set in **Tab. 3.2**

Limit Case of κ^2	Numerical Value
$\left \frac{4\epsilon_{\text{nonlin}}\omega_0^2}{3\epsilon_{\text{lin}}} \right $	0.3422
$\left \frac{4\epsilon_{\text{nonlin}}\omega_0^2}{3(\epsilon_{\text{lin}}+2\omega_0^2)} \right $	$3.462 \cdot 10^{-3}$
$\left \frac{4\epsilon_{\text{nonlin}}\omega_0^2}{3(\epsilon_{\text{lin}}-2\omega_0^2)} \right $	$3.533 \cdot 10^{-3}$

In addition to the limit cycles with amplitudes \bar{r}_b and \bar{r}_c , Eq. (3.7) has another approximate limit cycle \bar{r}_d . This branch is important if κ^2 is close to zero. In this case states along \bar{r}_d occur within the range of interest where σ is close to zero. The branches \bar{r}_b and \bar{r}_c are then connected by \bar{r}_d at a state where both branches undergo a change of stability (see Section 3.1.4).

Finding the limit cycles of Eqs. (3.15) becomes more difficult if damping is introduced ($\zeta > 0$). As the set of equations is still algebraic, numerical solutions can be found using the homotopy continuation (see Section 2.2.1) for algebraic equations.

For the case $\zeta > 0$, the accuracy of Eqs. (3.16) for approximating the limit cycles Eqs. (3.15) depends on the degree of damping present (see **Fig. 3.4**). The branches \bar{r}_b and \bar{r}_c are connected horizontally close to values \bar{r}_d and transformed into two loops l_a and l_b (see **Fig. 3.3**). Except for values close to the reversal point of these loops, the difference between the amplitudes of l_a , l_b and \bar{r}_b , \bar{r}_c is small. The phase shift now depends on σ . The difference between the phase shift of l_a , l_b and $\bar{\psi}_b$, $\bar{\psi}_c$ is significant for values close to the turning point of l_a and l_b . Since the phase shift is no longer constant along the bifurcated limit cycles, the complex interdependence between the amplitudes and the phase shifts of the loops of l_a and l_b can best be shown in a three dimensional phase-parameter-space (see **Fig. 3.4**).

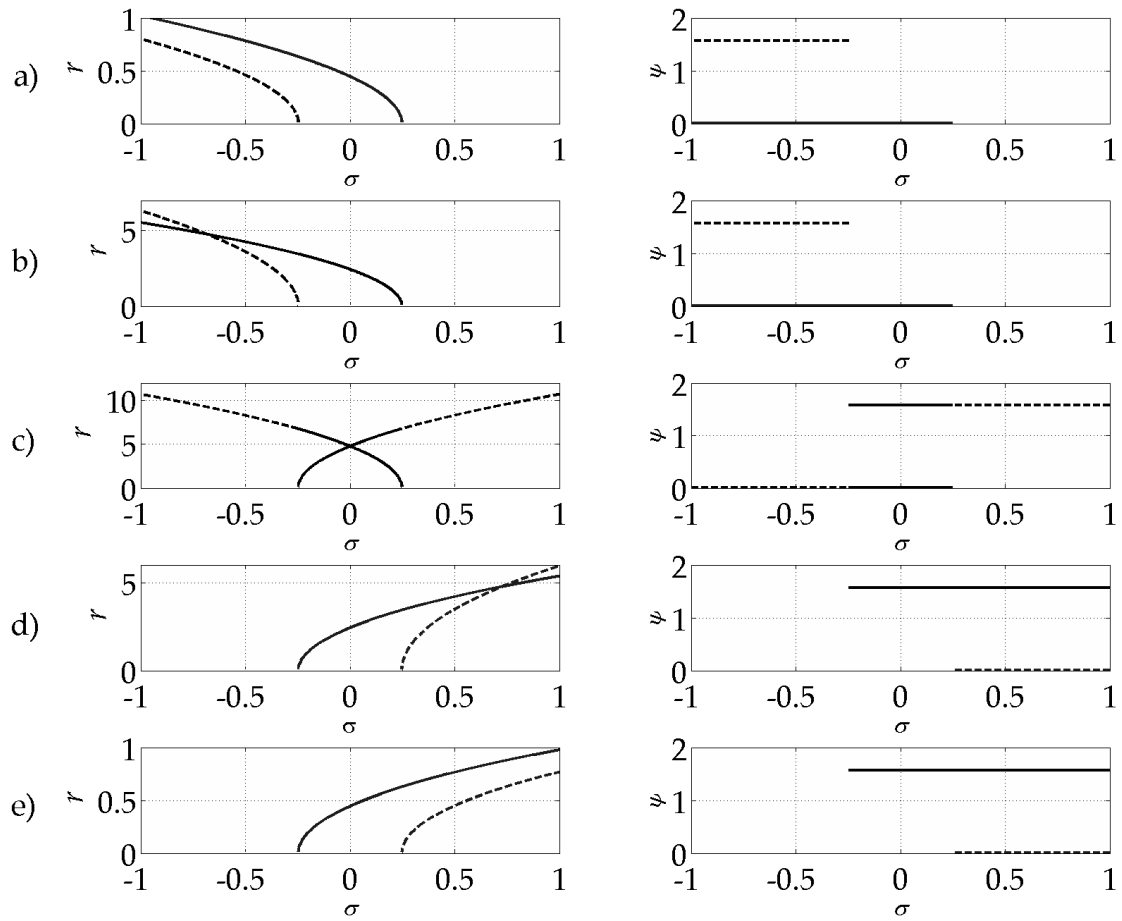


Figure 3.2: Analytical approximations Eqs. (3.16) of the amplitude and phase characteristics of the 1DOF system with parameters shown in **Tab. 3.2** for different values of κ^2 : a) $\kappa^2 = -0.4$, b) $\kappa^2 = -0.01$, c) $\kappa^2 = 0$, d) $\kappa^2 = 0.01$ e) $\kappa^2 = 0.4$. Solid: stable states, dashed: unstable states.

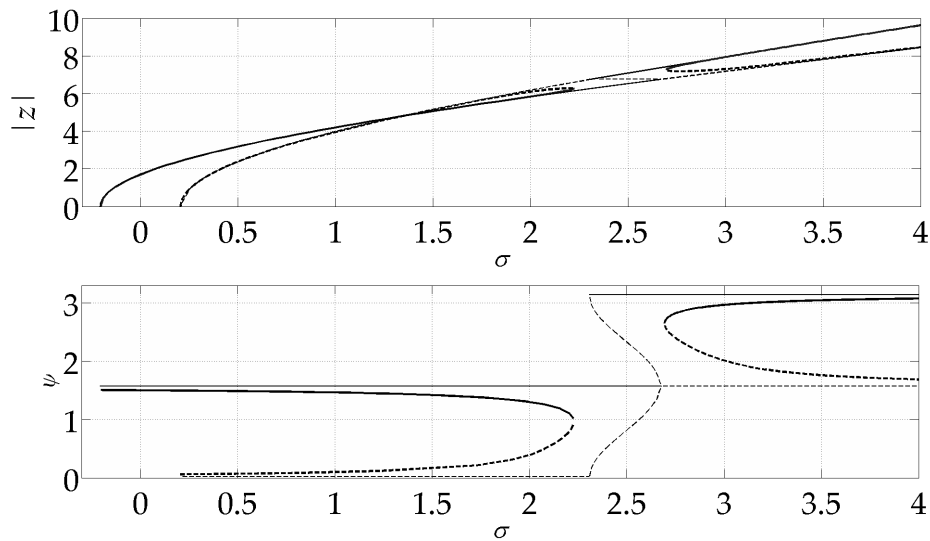


Figure 3.3: Limit cycles of Eqs. (3.15). Thin: undamped system $\zeta = 0$, bold: damped system $\zeta > 0$. Dashed: unstable states, solid: stable states

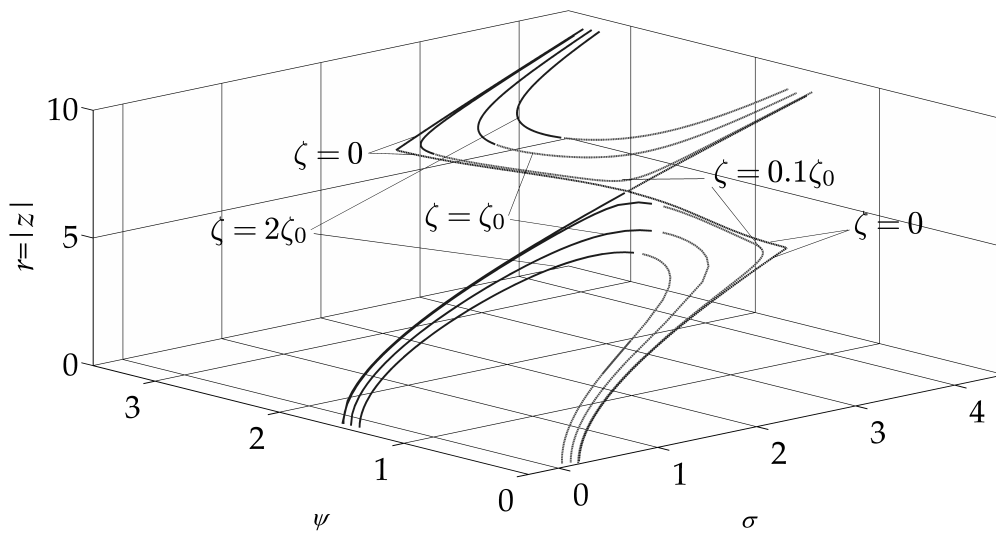


Figure 3.4: Limit cycles of Eqs. (3.15) in the state-parameter-space σ - ψ - r for different damping constants ζ . Solid: stable states, dashed: unstable states. The damping constant $\zeta_0 = 6.635 \cdot 10^{-4}$ refers to the value of ζ in **Tab. 3.2**.

3.1.4 Stability Analysis and Identification of the Type of the Bifurcations

When discussing where branches bifurcate and on which parameters the characteristic of these bifurcations depend, questions about the kind of bifurcation and the stability of the branches remained open. These questions will be addressed in this section.

In order to derive the Jacobian of Eqs. (3.15) these equations have to be linearised:

$$\Delta\bar{r}' = \frac{d\bar{r}'}{d\bar{r}}\Delta\bar{r} + \frac{d\bar{r}'}{d\bar{\psi}}\Delta\bar{\psi} = -\frac{\zeta}{2}\Delta\bar{r} + \frac{\mp\bar{r}_0^3\varepsilon_{\text{nl}} + 2\bar{r}_0\varepsilon_{\text{lin}}}{8\omega_0^2}\Delta\bar{\psi}, \quad (3.20a)$$

$$\Delta\bar{\psi}' = \frac{d\bar{\psi}'}{d\bar{r}}\Delta\bar{r} + \frac{d\bar{\psi}'}{d\bar{\psi}}\Delta\bar{\psi} = \frac{-3\varepsilon/\omega_0\kappa^2\sigma\bar{r}_0 + 3\kappa^2\bar{r}_0 \mp 2\varepsilon_{\text{nl}}\bar{r}_0}{8\omega_0^2}\Delta\bar{r}. \quad (3.20b)$$

Note the change of signs in Eq. (3.20a) depending on whether the equation is linearised at $\bar{\psi}_0 = 0$ or at $\bar{\psi}_0 = \pi/2$. Evaluating the Jacobian

$$J_{\text{bp}} = \begin{pmatrix} \frac{d\bar{r}'}{d\bar{r}} & \frac{d\bar{r}'}{d\bar{\psi}} \\ \frac{d\bar{\psi}'}{d\bar{r}} & \frac{d\bar{\psi}'}{d\bar{\psi}} \end{pmatrix} \quad (3.21)$$

at the branch points $\bar{r} = 0$, $\bar{\psi} = 0 \vee \pi/2$, $\sigma = \mp\sigma_b$ leads to eigenvalues $\lambda = 0$ of multiplicity 2 because both off diagonal elements are zero.

The Jacobian along the bifurcated limit cycles with the amplitudes \bar{r}_b , \bar{r}_c is

$$J_b = \begin{pmatrix} -4\omega_0^2\zeta & \mp\bar{r}_0^3\varepsilon_{\text{nl}} + 2\bar{r}_0\varepsilon_{\text{lin}} \\ (3\kappa^2(1 - \frac{\varepsilon\sigma}{\omega_0}) \mp 2\varepsilon_{\text{nl}})\bar{r}_0 & 0 \end{pmatrix} \frac{1}{8\omega_0^2} \quad (3.22)$$

with negative signs regarding the first branch \bar{r}_b and positive signs regarding the second branch \bar{r}_c . Substituting the averaged Eqs. (3.15) for \bar{r}_0 and evaluating the eigenvalues of the Jacobian J_b , intervals of σ can be found in which a given branch is stable:

- If both branches show hardening characteristics (see **Fig. 3.2,a&b**), \bar{r}_b is stable at $\sigma = [-\sigma_{\text{lim}}, \sigma_{b,2}]$ and \bar{r}_c at $\sigma = [\sigma_{b,3}, \sigma_b]$.
- If one branch has a hardening characteristic and the other one a softening one (see **Fig. 3.2,c**), \bar{r}_b is stable at $\sigma = [-\sigma_b, \sigma_{b,2}]$ and \bar{r}_c at $\sigma = [\sigma_{b,3}, \sigma_b]$.
- If both branches show softening characteristics (see **Fig. 3.2,d&e**), \bar{r}_b is stable at $\sigma = [-\sigma_b, \sigma_{b,2}]$ and \bar{r}_c at $\sigma = [\sigma_{b,3}, \sigma_{\text{lim}}]$.

Additional roots of the characteristic equation can be found. However, these roots are at $|\sigma| \gg 1$ so that $\varepsilon\sigma$ is not longer a small perturbation of Ω_0 . For such values the equations above do not approximate the behaviour of the equations of motion appropriately. The boundary value σ_{lim} limits the range of a meaningful σ . Obviously σ_{lim} depends on the choice of ε . The critical values for σ are

$$\sigma_{b,2} = \frac{\omega_0\varepsilon_{\text{lin}}\varepsilon_{\text{nl}} - 3\kappa^2\omega_0\varepsilon_{\text{lin}}}{2\varepsilon\omega_0^2\varepsilon_{\text{nl}} - 3\kappa^2\varepsilon\varepsilon_{\text{lin}}}, \quad (3.23a)$$

$$\sigma_{b,3} = \frac{-\omega_0\varepsilon_{\text{lin}}\varepsilon_{\text{nl}} - 3\kappa^2\omega_0\varepsilon_{\text{lin}}}{2\varepsilon\omega_0^2\varepsilon_{\text{nl}} - 3\kappa^2\varepsilon\varepsilon_{\text{lin}}}. \quad (3.23b)$$

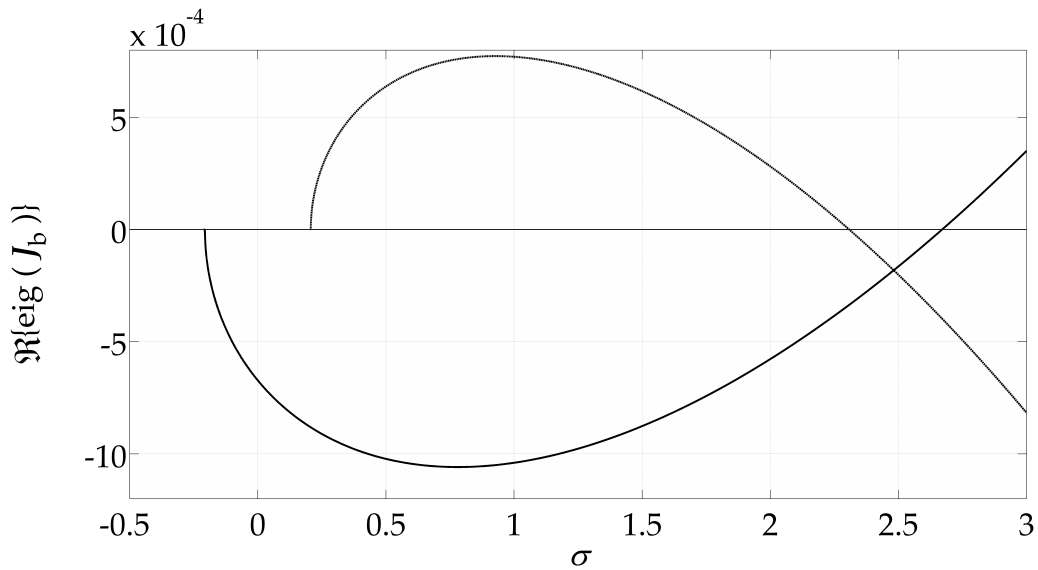


Figure 3.5: Real parts of the eigenvalues of the Jacobian J_b along the branches \bar{r}_b (solid) and \bar{r}_c (dashed) vs. the detuning parameter σ . The branches are stable for $\Re\{\text{eig}_i(J_b)\} < 0$.

Note that

$$\bar{r}_b(\sigma_{b,2}) = \bar{r}_c(\sigma_{b,3}) = \bar{r}_d = \sqrt{\frac{-2\varepsilon_{\text{lin}}}{\varepsilon_{\text{nonlin}}}}. \quad (3.24)$$

This expresses that both branches \bar{r}_b, \bar{r}_c undergo a change of stability at the branch points $\bar{r}_b - \bar{r}_d$ and $\bar{r}_c - \bar{r}_d$ respectively (see **Fig. 3.2**).

For the parameters displayed in **Tab. 3.2** the first branch \bar{r}_b is stable at $\sigma = [-0.207, 2.670]$ while the second branch \bar{r}_c is stable at $\sigma = [2.308, \sigma_{\text{lim}}]$. The dependence of $\Re\{\text{eig}(J_b)\}$ on σ for this specific case is shown graphically in **Fig. 3.5**.

The eigenvalues of the Jacobian of the trivial solution $\bar{r}_a, \bar{\psi}_a$ are zero between the two branch points. This does not give any information about the stability [19]. Nevertheless the stability of the rest position can be analysed evaluating Eqs. (3.15) at Eqs. (3.16a). The phase shift $\bar{\psi}_1 = 1/2 \arccos(\varepsilon/\varepsilon_{\text{lin}} 2\omega_0\sigma)$ with $\sigma \in \{-\sigma_b \leq \sigma \leq \sigma_b\}$ takes on values of $\pi/2 \geq \bar{\psi}_1 \geq 0$. Perturbing Eq. (3.16a) slightly $0 \leq \bar{r}_p \ll 1$ and substituting into Eq. (3.15a) gives

$$\bar{r}' = \frac{-4\omega_0^2\zeta + \varepsilon_{\text{lin}} \sin(2\bar{\psi}_1)}{8\omega_0^2} \bar{r}_p. \quad (3.25)$$

Hence

$$\zeta \stackrel{!}{<} \zeta_{\text{crit}} = 2\varepsilon_{\text{lin}} \quad \forall \quad \bar{r}' \stackrel{!}{>} 0, \quad \sigma | \sigma \in \{-\sigma_b \leq \sigma \leq \sigma_b\}. \quad (3.26)$$

Damping ratios $\zeta > \zeta_{\text{crit}}$ stabilise the trivial solution and annihilate the effect of the PR. Outside of the interval $[-\sigma_b, \sigma_b]$ the trivial solution does not exist in the absence of damping. In that case the solution of the equations of motion is a non-decaying free vibration with the amplitude depending on the initial conditions. If any damping is present the trivial solution does exist outside $[-\sigma_b, \sigma_b]$ and is asymptotically stable for all $\sigma \notin \{-\sigma_b \leq \sigma \leq \sigma_b\}$.

As illustrated the rest position is unstable/stable accordingly to whether the bifurcated limit cycle is stable/unstable. The bifurcations thus have the characteristic of subcritical and supercritical pitchfork bifurcations with the unstable solution as the repelling saddle and the stable one as the attracting node [18]. As the angular frequency of the limit cycles is $\eta = 1/2$, the bifurcations also have a period doubling characteristic.

In analogy to the stability analysis of the trivial solution the off-diagonal elements of the Jacobian are 0 for all states along \bar{r}_d . However, a perturbation analysis similar to the one for \bar{r}_a reveals all states along \bar{r}_d are unstable.

In this section, a 1DOF parametrically excited system was introduced. The equation of motion was derived and normalised. Limit cycles at PR were approximated using analytically and semi-analytically approaches and were discussed for different parameter regimes. The stability of the found limit cycles and the rest position was analysed.

3.2 Two Degree of Freedom System

The 1DOF system introduced in Section 3.1 is extended by a further degree of freedom (see Fig. 3.6). The system's equations of motion are derived in Section 3.2.1. The system's natural frequencies as well as the corresponding modes are computed in Section 3.2.2. The equations of motion are quasi-modally transformed in Section 3.2.3. As a consequence the equations of motion become dimensionless and generally applicable. They are also cast into similar form as for the case of the 1DOF system. Applying results from Section 3.1.3 the behaviour at PRs is approximated analytically for an undamped system and semi-analytically for a damped system in Section 3.2.4.

3.2.1 Modelling

The 1DOF system discussed previously is extended to a 2DOF system by coupling a second body with mass m_2 to the first body via a non-linear spring with the stiffness parameter $k_{12}(x_1, x_2)$ and a viscoelastic damper with the damping constant c_{12} (see Fig. 3.6). The second body is linked to the environment by two springs with non-linear stiffness parameters $k_{02}(x_2)$ and $k_2(x_2, t)$ and a viscoelastic damper with the damping constant c_{02} . For a more general terminology m , k_b , k and c are renamed to m_1 , k_{01} , k_1 and c_{01} .

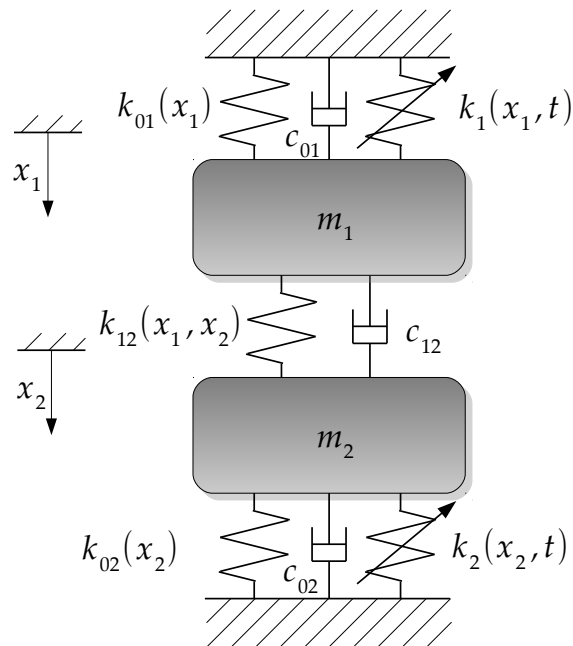


Figure 3.6: Mechanical lumped mass model for the 2DOF system: masses m_1 , m_2 , stiffness parameters $k_{01}(x_1)$, $k_{12}(x_1, x_2)$, $k_{02}(x_2)$ and $k_1(x_1, t)$, $k_2(x_2, t)$ damping constants c_{01} , c_{12} , c_{02} .

The stiffness parameters are

$$k_{ij}(x_i, x_j) = k_{ij,\text{lin}} + k_{ij,\text{nlin}}(x_i - x_j)^2, \quad (3.27a)$$

$$k_i(x_i, t) = k_{\text{PE},i}(x_i)(1 + \cos(\Omega_{\text{PE}}t)), \quad (3.27b)$$

$$k_{\text{PE},i}(x_i) = k_{\text{PE},i,\text{lin}} + k_{\text{PE},i,\text{nlin}}x_i^2. \quad (3.27c)$$

The equations of motion are

$$\mathbf{M}\ddot{\mathbf{x}} + \mathbf{C}\dot{\mathbf{x}} + \mathbf{K}(\mathbf{x})\mathbf{x} + \mathbf{K}_{\text{PE}}(\mathbf{x})\cos(\Omega_{\text{PE}}t)\mathbf{x} = \mathbf{0}. \quad (3.28)$$

The abbreviation $(\dot{}) = \frac{d}{dt}$ denotes a time derivative. As with the 1DOF system, the system is not externally but parametrically excited. The mass matrix \mathbf{M} is

$$\mathbf{M} = \begin{pmatrix} m_1 & \\ & m_2 \end{pmatrix}, \quad (3.29)$$

the damping matrix \mathbf{C} is

$$\mathbf{C} = \begin{pmatrix} c_{01} + c_{12} & -c_{12} \\ -c_{12} & c_{02} + c_{12} \end{pmatrix}. \quad (3.30)$$

The stiffness matrix \mathbf{K} has a linear and a non-linear part

$$\mathbf{K}(\mathbf{x}) = \mathbf{K}_{\text{lin}} + \mathbf{K}_{\text{nlin}}(\mathbf{x}), \quad (3.31)$$

where

$$\mathbf{K}_{\text{lin}} = \begin{pmatrix} k_{01,\text{lin}} + k_{12,\text{lin}} + k_{\text{PE},1,\text{lin}} & -k_{12,\text{lin}} \\ -k_{12,\text{lin}} & k_{02,\text{lin}} + k_{12,\text{lin}} + k_{\text{PE},2,\text{lin}} \end{pmatrix} \quad (3.32)$$

and

$$\mathbf{K}_{\text{nlin}}(x_1, x_2) = \begin{pmatrix} K_{\text{nlin},11}(x_1, x_2) & K_{\text{nlin},12}(x_1, x_2) \\ K_{\text{nlin},21}(x_1, x_2) & K_{\text{nlin},22}(x_1, x_2) \end{pmatrix} \quad (3.33)$$

with the components

$$K_{\text{nlin},11}(x_1, x_2) = (k_{01,\text{nlin}} + k_{12,\text{nlin}} + k_{\text{PE},1,\text{nlin}})x_1^2 + 3k_{12,\text{nlin}}x_2^2, \quad (3.34a)$$

$$K_{\text{nlin},12}(x_1, x_2) = -k_{12,\text{nlin}}(3x_1^2 + x_2^2), \quad (3.34b)$$

$$K_{\text{nlin},21}(x_1, x_2) = -k_{12,\text{nlin}}(x_1^2 + 3x_2^2), \quad (3.34c)$$

$$K_{\text{nlin},22}(x_1, x_2) = (k_{02,\text{nlin}} + k_{12,\text{nlin}} + k_{\text{PE},2,\text{nlin}})x_2^2 + 3k_{12,\text{nlin}}x_1^2. \quad (3.34d)$$

The PE stiffness matrix \mathbf{K}_{PE} is

$$\mathbf{K}_{\text{PE}}(x_1, x_2) = \begin{pmatrix} k_{\text{PE},1,\text{lin}} + k_{\text{PE},1,\text{nlin}}x_1^2 & \\ & k_{\text{PE},2,\text{lin}} + k_{\text{PE},2,\text{nlin}}x_2^2 \end{pmatrix}. \quad (3.35)$$

The system studied here is very similar to a system described by WELTE [22]. However, the modelling is more general and hence more widely applicable here. The values of the parameters in use are listed in **Tab. 3.4**.

Table 3.4: Parameters of Eq. (3.28), the 2DOF system depicted in Fig. 3.6

Parameter	Symbol	Value	Unit
Mass	m_1	$1.22 \cdot 10^{-10}$	kg
	m_2	$2.44 \cdot 10^{-10}$	kg
Damping Constant	c_{01}	$1.94 \cdot 10^{-8}$	$\text{N m}^{-1} \text{s}$
	c_{12}	$0.97 \cdot 10^{-8}$	$\text{N m}^{-1} \text{s}$
	c_{12}	$1.94 \cdot 10^{-8}$	$\text{N m}^{-1} \text{s}$
Linear Stiffness Constant	$k_{01,\text{lin}}$	3.505	N m^{-1}
	$k_{12,\text{lin}}$	1.753	N m^{-1}
	$k_{02,\text{lin}}$	3.505	N m^{-1}
Non-linear Stiffness Constant	$k_{01,\text{nonlin}}$	$18 \cdot 10^9$	N m^{-3}
	$k_{12,\text{nonlin}}$	$9 \cdot 10^9$	N m^{-3}
	$k_{02,\text{nonlin}}$	$18 \cdot 10^9$	N m^{-3}
Linear PE Stiffness Constant	$k_{\text{PE},1,\text{lin}}$	0.2281	N m^{-1}
	$k_{\text{PE},2,\text{lin}}$	0.2281	N m^{-1}
Non-linear PE Stiffness Constant	$k_{\text{PE},1,\text{nonlin}}$	$-1.056 \cdot 10^{10}$	N m^{-3}
	$k_{\text{PE},2,\text{nonlin}}$	$-1.056 \cdot 10^{10}$	N m^{-3}

3.2.2 Modal Analysis

The system's natural frequencies are crucial for further investigations. In order to determine them, in the following a modal analysis is carried out in this section.

With PE disabled Eq. (3.28) becomes

$$M\ddot{x} + C\dot{x} + K(x)x = \mathbf{0}. \quad (3.36)$$

Linearising at $x = [0, 0]^T$ further simplifies Eq. (3.36) to

$$M\ddot{x} + C\dot{x} + K_{\text{lin}}x = \mathbf{0}, \quad (3.37)$$

which can be expressed as a set of first order differential equations:

$$\begin{pmatrix} \mathbf{1} \\ M \end{pmatrix} \begin{pmatrix} \dot{x} \\ \ddot{x} \end{pmatrix} = \begin{pmatrix} & \mathbf{1} \\ -K_{\text{lin}} & -C \end{pmatrix} \begin{pmatrix} x \\ \dot{x} \end{pmatrix} \quad (3.38a)$$

$$\Leftrightarrow \begin{pmatrix} \dot{x} \\ \ddot{x} \end{pmatrix} = \begin{pmatrix} & \mathbf{1} \\ -M^{-1}K_{\text{lin}} & -M^{-1}C \end{pmatrix} \begin{pmatrix} x \\ \dot{x} \end{pmatrix} = J \begin{pmatrix} x \\ \dot{x} \end{pmatrix}. \quad (3.38b)$$

With the ansatz $[x \ \dot{x}]^T = \hat{x}e^{\lambda t}$ the above equation gives the eigenvalue problem

$$(J - \lambda \mathbf{1})v = \mathbf{0}. \quad (3.39)$$

Its eigenvalues $\lambda_i = \mu_i \pm i\omega_i$ are complex conjugates. Their imaginary parts ω_i are the system's natural frequencies. The four complex eigenvectors v_i each have two complex conjugate components $\varphi_{ij} \pm i\chi_{ij}$. Their real parts φ_{ij} are the modes of the damped system.

If no damping is present ($\mathbf{C} = \mathbf{0}$), the eigenvalues λ_i are pure imaginary and the eigenvectors $\boldsymbol{\nu}_i$ real. The eigenvalue problem Eq. (3.39) simplifies to

$$(\mathbf{K}_{\text{lin}} - \omega^2 \mathbf{M}_0) \boldsymbol{\varphi} = \mathbf{0}, \quad (3.40)$$

with $\boldsymbol{\varphi}_i = [\varphi_{i1} \ \varphi_{i2}]^T$.

In this case the natural frequencies are

$$\omega_{1,2} = \sqrt{\frac{m_1 K_{\text{lin},11} + m_2 K_{\text{lin},22}}{2 m_1 m_2} + \dots} \pm \sqrt{\left(\frac{m_1 K_{\text{lin},11} + m_2 K_{\text{lin},22}}{2 m_1 m_2}\right)^2 - \frac{K_{\text{lin},11} K_{\text{lin},22} - k_{12,\text{lin}}^2}{m_1 m_2}} \quad (3.41)$$

and the eigenvectors are

$$\boldsymbol{\varphi}_i^* = \begin{pmatrix} 1 \\ \frac{k_{12,\text{lin}}}{K_{\text{lin},ii} - m_i \omega_i^2} \end{pmatrix}, \quad (3.42)$$

if they are normalised to $\varphi_{i1}^* = 1$.

3.2.3 Quasi-Modal Transformation of the Equations of Motion

Modal decomposition is commonly applied to linear, non-PE systems. The transformation to modal coordinates decouples the n degree of freedom system equations, yielding n uncoupled 1DOF systems. For non-linear and PE systems no such transformation exists. However, the equations can be written in *quasi-modal* form by transformation to the modal coordinates of the linear, non-PE system [8], [11]. Such quasi-modal transformation has several advantages: first of all, each line of the equations of motion becomes similar to the equation of motion of the 1DOF system. Both systems can be compared more readily and similarities become more obvious. Secondly, as explained in Section 2.1.1, at PR mainly one mode is excited. This mode depends on the value of the PE frequency, which has to have the factor $2/n$, $n \in \mathbb{N}$ regarding the natural frequency of this mode. Combining both leads to the most powerful advantage: the quasi-modal transformation enables 2DOF system to be approximated by a 1DOF system at PR. The quasi-modal transformation is explained in this section. Its outcomes are discussed in the next section.

The eigenvectors are normalised so that

$$\boldsymbol{\varphi}_i^T \mathbf{M} \boldsymbol{\varphi}_i = 1. \quad (3.43)$$

These mass normalised eigenvectors $\boldsymbol{\varphi}_i$ form the modal matrix $\boldsymbol{\Phi} = [\boldsymbol{\varphi}_1 \ \boldsymbol{\varphi}_2]$. Hence the displacements x_i can be transformed quasi-modally to the quasi-modal displacements z_i by $\mathbf{x} = \mathbf{x}^* \boldsymbol{\Phi} \mathbf{z}$. The normalisation with \mathbf{x}^* is employed in analogy to the 1DOF system to make the equations of motion dimensionless as well as to provide a sufficient scaling for evaluating the differential equations numerically. As mentioned before, considering a linear, time invariant system (e.g. Eq. (3.37)), the equations of motion are decoupled by such a transformation. Regarding a PE system, this is not the case. The transformation

diagonalises the time invariant matrices, which are the mass and the damping matrix as well as the linear part of the stiffness matrix. But the transformed time variant matrix, the PE stiffness matrix, becomes full. Moreover, z_i are not modal displacements of the system, because these modes are the solution of the eigenvalue problem of the linear, time invariant system only. Hence z_i are called *quasi-modal* displacements. Thus Eq. (3.28) transforms to

$$\Phi^T M \Phi \ddot{z} + \Phi^T C \Phi \dot{z} + \Phi^T K_{\text{lin}} \Phi z + \Phi^T K_{\text{nlin}} \Phi z + \Phi^T K_{\text{PE}} \Phi z \cos(\Omega_{\text{PE}} t) = \mathbf{0}. \quad (3.44)$$

Because of Eq. (3.43) this equation simplifies to

$$\ddot{z} + Z \dot{z} + \Lambda z + \Lambda_{\text{nlin}} z + E z \cos(\Omega_{\text{PE}} t) = \mathbf{0}, \quad (3.45)$$

where Λ is the spectral matrix

$$\Lambda = \begin{pmatrix} \omega_{n1}^2 & \\ & \omega_{n2}^2 \end{pmatrix}. \quad (3.46)$$

The natural angular frequencies ω_{ni} are named such that $\omega_{n1} < \omega_{n2}$. In case of proportional damping with the proportional damping constant δ the quasi-modal damping matrix Z can be written as

$$Z = \delta \Lambda = \begin{pmatrix} \delta \omega_{n1}^2 & \\ & \delta \omega_{n2}^2 \end{pmatrix} = \begin{pmatrix} 2\zeta_1 \omega_{n1} & \\ & 2\zeta_2 \omega_{n2} \end{pmatrix}. \quad (3.47)$$

Here $\zeta_i = \frac{\delta \omega_{ni}}{2}$ are the the quasi-modal damping ratios. Normalising regarding the eigen-time $\tau = \Omega_{\text{PE}} t$ and the dimensionless PE frequency $\Omega = \frac{\Omega_{\text{PE}}}{\Omega^*}$ gives

$$\begin{aligned} z'' + \begin{pmatrix} 2\zeta_1 \frac{\omega_1}{\Omega} & \\ & 2\zeta_2 \frac{\omega_2}{\Omega} \end{pmatrix} z' + \begin{pmatrix} \frac{\omega_1^2}{\Omega^2} & \\ & \frac{\omega_2^2}{\Omega^2} \end{pmatrix} z + \dots \\ + \begin{pmatrix} \frac{\kappa_1^2}{\Omega^2} z_1^2 + \frac{\kappa_{12}^2}{\Omega^2} z_1 z_2 + \frac{\kappa_{13}^2}{\Omega^2} z_2^2 & \frac{\kappa_{14}^2}{\Omega^2} z_1^2 + \frac{\kappa_{15}^2}{\Omega^2} z_1 z_2 + \frac{\kappa_{16}^2}{\Omega^2} z_2^2 \\ \frac{\kappa_{26}^2}{\Omega^2} z_1^2 + \frac{\kappa_{25}^2}{\Omega^2} z_1 z_2 + \frac{\kappa_{24}^2}{\Omega^2} z_2^2 & \frac{\kappa_{23}^2}{\Omega^2} z_1^2 + \frac{\kappa_{22}^2}{\Omega^2} z_1 z_2 + \frac{\kappa_2^2}{\Omega^2} z_2^2 \end{pmatrix} z + \begin{pmatrix} \varepsilon_{1,\text{lin}} & \varepsilon_{12,\text{lin}} \\ \varepsilon_{12,\text{lin}} & \varepsilon_{2,\text{lin}} \end{pmatrix} + \dots \\ + \begin{pmatrix} \varepsilon_{1,\text{nlin}} z_1^2 + \varepsilon_{12,\text{nlin}} z_1 z_2 + \varepsilon_{13,\text{nlin}} z_2^2 & \varepsilon_{4,\text{nlin}} z_1^2 + \varepsilon_{5,\text{nlin}} z_1 z_2 + \varepsilon_{6,\text{nlin}} z_2^2 \\ \varepsilon_{4,\text{nlin}} z_1^2 + \varepsilon_{5,\text{nlin}} z_1 z_2 + \varepsilon_{6,\text{nlin}} z_2^2 & \varepsilon_{23,\text{nlin}} z_1^2 + \varepsilon_{22,\text{nlin}} z_1 z_2 + \varepsilon_{2,\text{nlin}} z_2^2 \end{pmatrix} \dots \\ \frac{1}{\Omega^2} \cos(\tau) z = \mathbf{0}, \end{aligned} \quad (3.48)$$

where $\omega_i = \frac{\omega_{ni}}{\Omega^*}$. Note that both PE matrices are symmetric. The values of the non-dimensional parameters derived from the physical parameters listed in **Tab. 3.4** are listed in **Tab. 3.5**. The naming of the indices of the components becomes clear in Section 3.2.4, where it is shown that the 2DOF model can be reduced to a 1DOF model for predicting the behaviour at parametric resonances.

Table 3.5: Non-dimensional parameters of Eq. (3.48) and their relation to the physical parameters of the 2DOF system. The values listed here are used in Chapter 4 for numerical investigations.

Non-dimensional Parameter	Symbol	Value
Detuning Parameter	ε	0.1
Natural Angular Frequencies	ω_1	1.3628
	ω_2	2.2109
Eigenvectors (see Eq. (3.43))	$\boldsymbol{\varphi}_1$	$\begin{pmatrix} 3.2524 \\ 5.9745 \end{pmatrix} 10^4$
	$\boldsymbol{\varphi}_2$	$\begin{pmatrix} 8.4492 \\ -2.2998 \end{pmatrix} 10^4$
Modal Damping Ratios	ζ_1	$3.7715 \cdot 10^{-4}$
	ζ_2	$6.1187 \cdot 10^{-4}$
Non-linearity Parameters	κ_1^2	$1.0806 \cdot 10^{-5}$
	κ_{12}^2	$1.9328 \cdot 10^{-5}$
	κ_{13}^2	$3.2192 \cdot 10^{-5}$
	κ_{14}^2	$-2.9641 \cdot 10^{-5}$
	κ_{15}^2	$1.1993 \cdot 10^{-5}$
	κ_{16}^2	$-1.6371 \cdot 10^{-5}$
	κ_{26}^2	$-0.34375 \cdot 10^{-5}$
	κ_{25}^2	$-7.4015 \cdot 10^{-5}$
	κ_{24}^2	$-8.5332 \cdot 10^{-5}$
	κ_{23}^2	$11.820 \cdot 10^{-5}$
	κ_{22}^2	$3.6217 \cdot 10^{-5}$
	κ_2^2	$15.827 \cdot 10^{-5}$

Non-dimensional Parameter	Symbol	Value
Linear PE Parameters	$\varepsilon_{1,\text{lin}}$	0.10555
	$\varepsilon_{12,\text{lin}}$	0.031341
	$\varepsilon_{2,\text{lin}}$	0.17490
Non-linear PE Parameters	$\varepsilon_{1,\text{nonlin}}$	$-1.4636 \cdot 10^{-5}$
	$\varepsilon_{12,\text{nonlin}}$	$0.42190 \cdot 10^{-5}$
	$\varepsilon_{13,\text{nonlin}}$	$-0.99681 \cdot 10^{-5}$
	$\varepsilon_{4,\text{nonlin}}$	$0.21095 \cdot 10^{-5}$
	$\varepsilon_{5,\text{nonlin}}$	$-1.9936 \cdot 10^{-5}$
	$\varepsilon_{6,\text{nonlin}}$	$-1.9949 \cdot 10^{-5}$
	$\varepsilon_{23,\text{nonlin}}$	$-0.99681 \cdot 10^{-5}$
	$\varepsilon_{22,\text{nonlin}}$	$-3.9898 \cdot 10^{-5}$
	$\varepsilon_{2,\text{nonlin}}$	$-5.4113 \cdot 10^{-5}$
Scaling Parameter	Symbol	Value
Proportional Damping Constant	δ	$5.535 \cdot 10^{-4} \text{ s}$
Frequency Scaling Parameter	Ω^*	10^5 s^{-1}
Displacement Scaling Parameter	x^*	10^{-6} m

3.2.4 Analytical and Semi-Analytical Investigation of the Behaviour at Parametric Resonances

In this section the behaviour of the 2DOF system described in Section 3.2.1 at parametric resonances is analysed analytically and semi-analytically. Approximations of the amplitudes and phase shifts of the limit cycles of the vibrations in PR are derived.

Allowing only small perturbations $\Omega = \Omega_0 + \varepsilon\sigma$, Eq. (3.48), according to Eq. (3.8) and Eqs. (3.9), can be written as

$$\begin{aligned}
 & \mathbf{z}'' + \begin{pmatrix} 2\zeta_1 \frac{\omega_1}{\Omega_0} & \\ & 2\zeta_2 \frac{\omega_2}{\Omega_0} \end{pmatrix} \mathbf{z}' + \begin{pmatrix} \frac{\omega_1^2}{\Omega_0^2} & \\ & \frac{\omega_2^2}{\Omega_0^2} \end{pmatrix} \mathbf{z} \\
 & + \begin{pmatrix} \frac{\kappa_{12}^2}{\Omega_0^2} z_1^2 + \frac{\kappa_{13}^2}{\Omega_0^2} z_1 z_2 + \frac{\kappa_{14}^2}{\Omega_0^2} z_2^2 & \frac{\kappa_{15}^2}{\Omega_0^2} z_1^2 + \frac{\kappa_{16}^2}{\Omega_0^2} z_1 z_2 + \frac{\kappa_{17}^2}{\Omega_0^2} z_2^2 \\ \frac{\kappa_{26}^2}{\Omega_0^2} z_1^2 + \frac{\kappa_{25}^2}{\Omega_0^2} z_1 z_2 + \frac{\kappa_{24}^2}{\Omega_0^2} z_2^2 & \frac{\kappa_{23}^2}{\Omega_0^2} z_1^2 + \frac{\kappa_{22}^2}{\Omega_0^2} z_1 z_2 + \frac{\kappa_{27}^2}{\Omega_0^2} z_2^2 \end{pmatrix} \mathbf{z} + \begin{pmatrix} \varepsilon_{1,\text{lin}} & \varepsilon_{12,\text{lin}} \\ \varepsilon_{12,\text{lin}} & \varepsilon_{2,\text{lin}} \end{pmatrix} \\
 & + \begin{pmatrix} \varepsilon_{1,\text{nonlin}} z_1^2 + \varepsilon_{12,\text{nonlin}} z_1 z_2 + \varepsilon_{13,\text{nonlin}} z_2^2 & \varepsilon_{4,\text{nonlin}} z_1^2 + \varepsilon_{5,\text{nonlin}} z_1 z_2 + \varepsilon_{6,\text{nonlin}} z_2^2 \\ \varepsilon_{4,\text{nonlin}} z_1^2 + \varepsilon_{5,\text{nonlin}} z_1 z_2 + \varepsilon_{6,\text{nonlin}} z_2^2 & \varepsilon_{23,\text{nonlin}} z_1^2 + \varepsilon_{22,\text{nonlin}} z_1 z_2 + \varepsilon_{2,\text{nonlin}} z_2^2 \end{pmatrix} \frac{1}{\Omega_0^2} \cos(\tau) \mathbf{z} \\
 & - \left(\begin{pmatrix} \omega_1^2 & \\ & \omega_2^2 \end{pmatrix} + \begin{pmatrix} \kappa_{12}^2 z_1^2 + \kappa_{13}^2 z_1 z_2 + \kappa_{14}^2 z_2^2 & \kappa_{15}^2 z_1^2 + \kappa_{16}^2 z_1 z_2 + \kappa_{17}^2 z_2^2 \\ \kappa_{26}^2 z_1^2 + \kappa_{25}^2 z_1 z_2 + \kappa_{24}^2 z_2^2 & \kappa_{23}^2 z_1^2 + \kappa_{22}^2 z_1 z_2 + \kappa_{27}^2 z_2^2 \end{pmatrix} \right) \frac{2\varepsilon\sigma}{\Omega_0^3} \mathbf{z} = \mathbf{0}.
 \end{aligned} \tag{3.49}$$

Regarding the 1DOF system averaging the set of differential equations for the amplitude and phase of the vibration $z(t)$ is very convenient, because at PR the period of all harmonics are integer multiples of each other. Averaging over one period of $z(t)$ calculates the (multiple) mean of each term, many of which are equal to zero. Due to its non-linearity Eq. (3.49) has some mixed terms of harmonics of different frequencies. If these frequencies are not integer multiples of each other, the results of an average for the 2DOF system are too long to be displayed here.

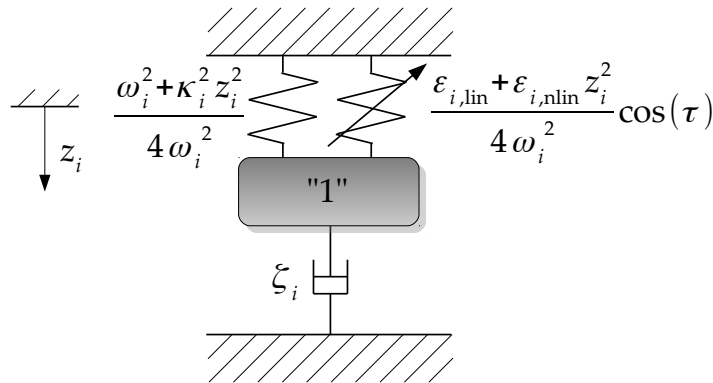


Figure 3.7: Mechanical lumped mass model for the quasi-modally transformed system. The 2DOF system can be approximated by a 1DOF at the corresponding PR: quasi-modal displacement z_i , natural angular frequency ω_i , non-linearity parameter κ_i^2 , linear PE parameter $\varepsilon_{i,\text{lin}}$, non-linear PE parameter $\varepsilon_{i,\text{nonlin}}$, quasi-modal damping ratio ζ_i .

As described in Section 2.1.1, at PRs of multi degree of freedom systems mainly one mode $\omega_i = \frac{n\Omega}{2}$ is excited. Using this knowledge and setting $z = [z_1, 0]^T \vee [0, z_2]^T$ simplifies Eq. (3.49) to a scalar problem:

$$\begin{aligned} z_i'' + 2\zeta_i\eta_i z_i' + \eta_i^2 z_i + \chi_i^2 z_i^3 + \frac{1}{\Omega_0^2} [\varepsilon_{i,\text{lin}} \cos(\tau) - \varepsilon 2\eta_i \omega_i \sigma] z_i + \dots \\ + \frac{1}{\Omega_0^2} [\varepsilon_{i,\text{nl}} \cos(\tau) - \varepsilon 2\chi_i \kappa_i \sigma] z_i^3 + \mathcal{O}(\varepsilon^2, \varepsilon \varepsilon_{i,\text{lin}}, \varepsilon \varepsilon_{i,\text{nl}}, \zeta_i \varepsilon_{i,\text{nl}}) = 0. \end{aligned} \quad (3.50)$$

Here $\eta_i = \omega_i/\Omega_0$ is the frequency ratio between the natural angular frequency and the PE centre frequency. For both PRs $\Omega_0 = 2\omega_1$ and $\Omega_0 = 2\omega_2$ the ratio takes on the value $\eta = 1/2$. The ratio $\chi = \frac{\kappa}{\Omega_0}$ relates the regarding non-linearity parameter to the PE centre frequency.

Being able to approximate Eq. (3.49) with a scalar equation means the quasi-modal 2DOF system can be reduced to a 1DOF system for studying the behaviour at the relevant PR (see **Fig. 3.7**). However, this does not mean a reduction of the original physical model. The bodies of the 2DOF system undergo a vibration which can be approximated by

$$\begin{aligned} x_1 &= \varphi_{11}z_1 + \varphi_{21}z_2 \approx \varphi_{i1}z_i = \varphi_{i1}r_i \cos(\eta_i\tau + \psi_i), \\ x_2 &= \varphi_{12}z_1 + \varphi_{22}z_2 \approx \varphi_{i1}z_i = \varphi_{i1}r_i \cos(\eta_i\tau + \psi_i). \end{aligned} \quad (3.51)$$

Eq. (3.50) has already been averaged in Section 3.1.3 according to Krylov-Bogolyubov for $\Omega_0 = 2\omega_j$. Limit cycles, a stability analysis of these limit cycles and an analysis of the bifurcation points can also be found in that section.

Using the parameters in **Tab. 3.5**, the quasi-modal amplitudes can be calculated at both PRs $\Omega = 2\omega_1$ and $\Omega = 2\omega_2$ (see **Fig. 3.8, 3.9** and **Fig. 3.10, 3.11**). The branches bifurcate at $\mp\sigma_{1b} = \mp 0.387$ at the first PR $\Omega = 2\omega_1$ and at $\mp\sigma_{2b} = \mp 0.396$ at the second PR $\Omega = 2\omega_2$.

Because for the parameters used here $\kappa_2^2 > \kappa_1^2$, the branches have stronger softening characteristic at the second PR than they have at the first PR. Consequently the vibrations of both bodies undergo stronger excitation at the first PR than they do at the second PR. Considering damping the first loop at the first PR closes near $\bar{r}_{1d} = 120.1$ and the first loop at the second PR closes near $\bar{r}_{2d} = 80.4$.

Modal damping is generally larger in higher modes. Hence differences between the analytical approximation neglecting damping and the semi-analytical one including damping are larger in higher modes. For the parameters used here the second modal damping ζ_2 is almost twice as large as the first modal damping ζ_1 . The difference between the analytical approximation and the semi-analytical one is accordingly larger for the second PR than it is for the first PR.

Within the instability band of the rest position the amplitudes of the branched limit cycles predicted by the analytical and by the semi-analytical approximation agree closely.

In this section, the behaviour of a 2DOF system described in Section 3.2.1 was estimated analytically and semi-analytically presenting approximations of the amplitudes and phase shifts of the limit cycles of the vibrations at PR. It was shown that the 2DOF system can be modelled as a 1DOF system at PRs. The solution of the system equation of this 1DOF was studied in Section 3.1, leading to analytical and semi-analytical approximations of the amplitudes and phase shifts of possible limit cycles. The dependencies of the amplitudes and phase shifts on the system parameters were studied. Stability analyses of the rest position and the detected limit cycles were carried out.

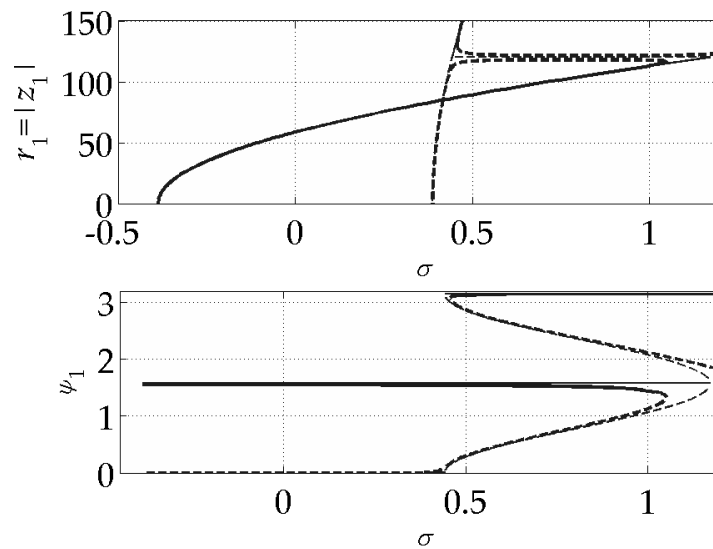


Figure 3.8: Limit cycles of the first quasi-modal vibration z_1 for parameters as stated in **Tab. 3.5** at the first PR ($\Omega_0 = 2\omega_1$). The amplitude is denoted with r_1 , the phase shift with ψ_1 . Bold: with damping, thin: without damping, Solid: stable states, dashed: unstable states.

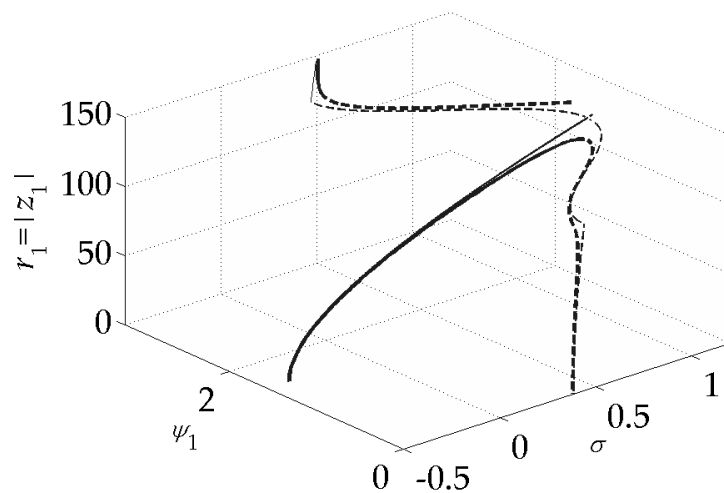


Figure 3.9: Limit cycles of the first quasi-modal vibration z_1 in the state-parameter-space σ - ψ_1 - $|r_1|$ for parameters as stated in **Tab. 3.5** at the first PR ($\Omega_0 = 2\omega_1$). Bold: with damping, thin: without damping. Solid: stable states, dashed: unstable states.

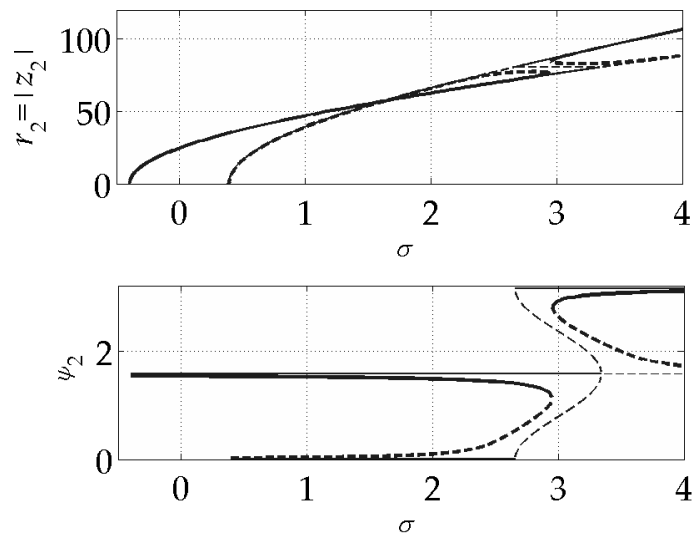


Figure 3.10: Limit cycles of the second quasi-modal vibration z_2 for parameters as stated in **Tab. 3.5** at the second PR ($\Omega_0 = 2\omega_2$). The amplitude is denoted with r_2 , the phase shift with ψ_2 . Bold: with damping, thin: without damping. Solid: stable states, dashed: unstable states.

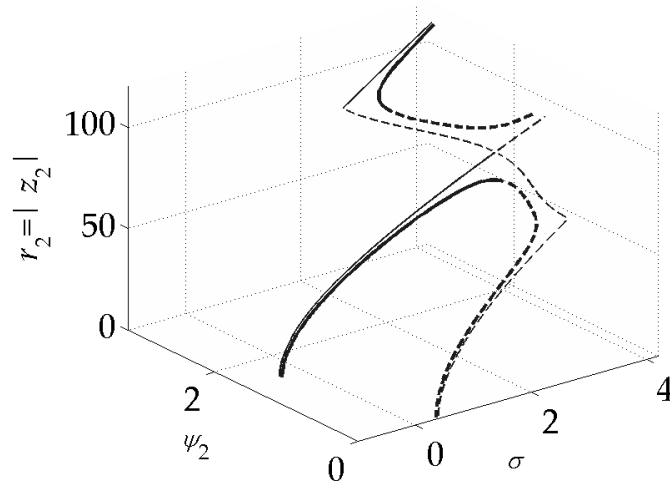


Figure 3.11: Limit cycles of the second quasi-modal vibration z_2 in the state-parameter-space σ - ψ_2 - $|r_2|$ for parameters as stated in **Tab. 3.5** at the second PR ($\Omega_0 = 2\omega_2$). Bold: with damping, thin: without damping. Solid: stable states, dashed: unstable states.

4 Numerical Investigations of One and Two Degree of Freedom Parametrically Excited Non-Linear Systems

In Chapter 3, two mechanical lumped mass systems, a non-linear 1DOF system and a non-linear 2DOF system, were introduced. Both systems undergo PE. This PE destabilises the rest position of those systems at certain PE frequencies (see Section 2.1.1). The amplitudes of the vibrations may be limited due to non-linearities. In such cases stable limit cycles can be found. In the previous chapter limit cycles of the vibrations of the systems in PRs were approximated analytically and semi-analytically. These results are verified in this section by numerical methods. Furthermore the basins of attraction of the stable limit cycles are investigated.

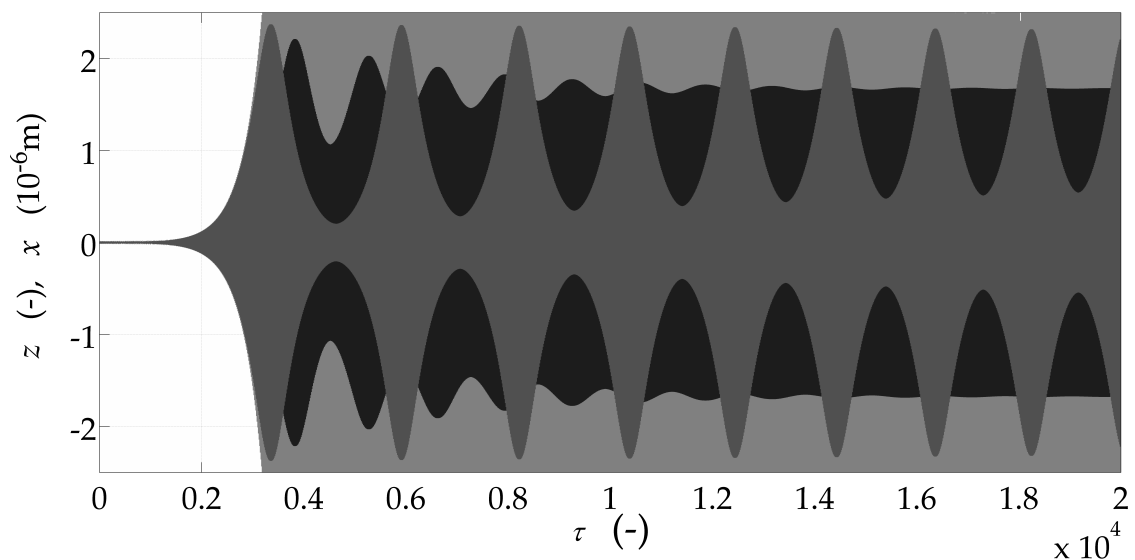


Figure 4.1: Time series of $z(\tau)$ at $\Omega = 2\omega_0$ starting with initial conditions $r_0 = 10^{-3}$, $\psi_0 = 0$. Grey, solid (background): linearised, undamped system (Mathieu's equation), $\kappa = \varepsilon_{\text{nl}} = \zeta = 0$. Black: parameters as stated in **Tab. 3.2**. Grey, semi-transparent (foreground): undamped system, $\zeta = 0$.

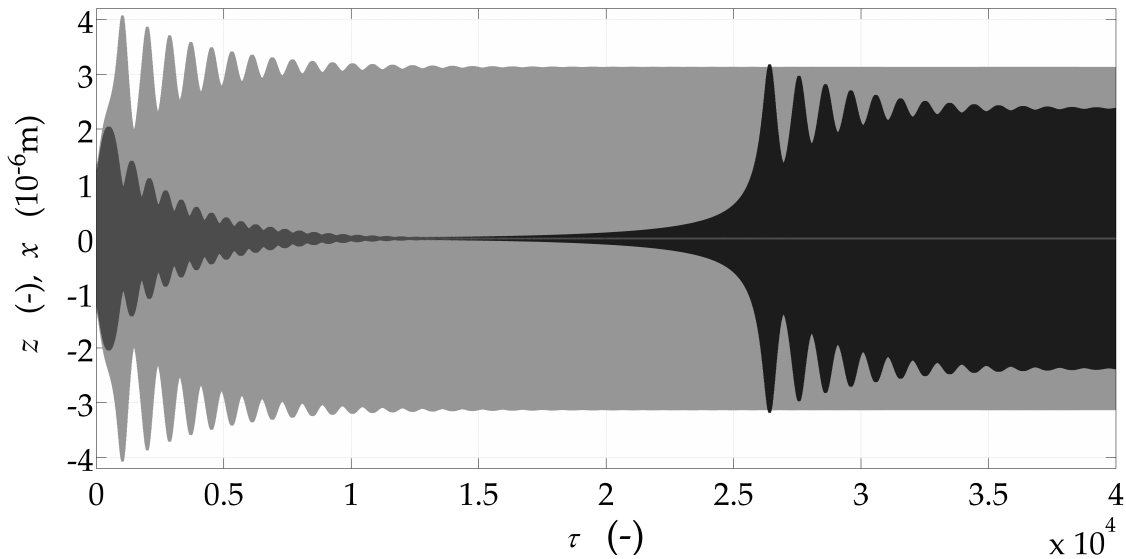


Figure 4.2: Time series of $z(\tau)$ at different Ω starting with different initial conditions. Light grey (background): $\sigma = 0.5$, $r_0 = 1.3$, $\psi_0 = 1.49$. Dark grey (foreground): $\sigma = 0.5$, $r = 1.2$, $\psi = 1.49$. Black: $\sigma = 0.205$, $r_0 = 10^{-3}$, $\psi_0 = 0$.

4.1 Numerical Investigations of the One Degree of Freedom System

In this section the results of Section 3.1.3 predicting the behaviour of the 1DOF system introduced in Section 3.1.1 are validated numerically. Simulating the behaviour of Eq. (3.7) over a timespan of $\tau = 20 \cdot 10^3$ gives a basic understanding of the effect of the non-linear terms in Eq. (3.7) (see Fig. 4.1). Linearising the system and neglecting the damping (setting $\zeta = 0$) lead to Mathieu's equation. Simulating at the centre frequency of the PR means the system will be repelled by the unstable rest position (grey, solid graph in Fig. 4.1). Since the system has been linearised a branched solution does not exist leaving the amplitudes of the vibration $z(\tau)$ to increase infinitely. Setting the non-linear terms— κ^2 and ε_{nlm} —to the values in Tab. 3.2 changes the behaviour significantly (grey, semi-transparent graph in Fig. 4.1): Since there is no damping present ($\zeta = 0$) the amplitude of the vibration first increases as quickly as for Mathieu's equation. But due to the non-linear terms a branched stable limit cycle exists and the amplitude of the vibration $z(\tau)$ is bounded. The amplitude of this stable steady state is $r = |z| = 1.70$, which coincides with the analytical approximation of the amplitude of the branched limit cycle in Section 3.1.3. The system converges to this state with modulated amplitudes first overshooting the amplitude of the stable limit cycle. Adding damping makes the system proceed towards the branched stable limit cycle faster (black graph in Fig. 4.1). The amplitude asymptotes to $r = |z| = 1.70$ as predicted in Section 3.1.3 by both the analytical and the semi-analytical approximation. The frequency of the modulation of the amplitude also increases.

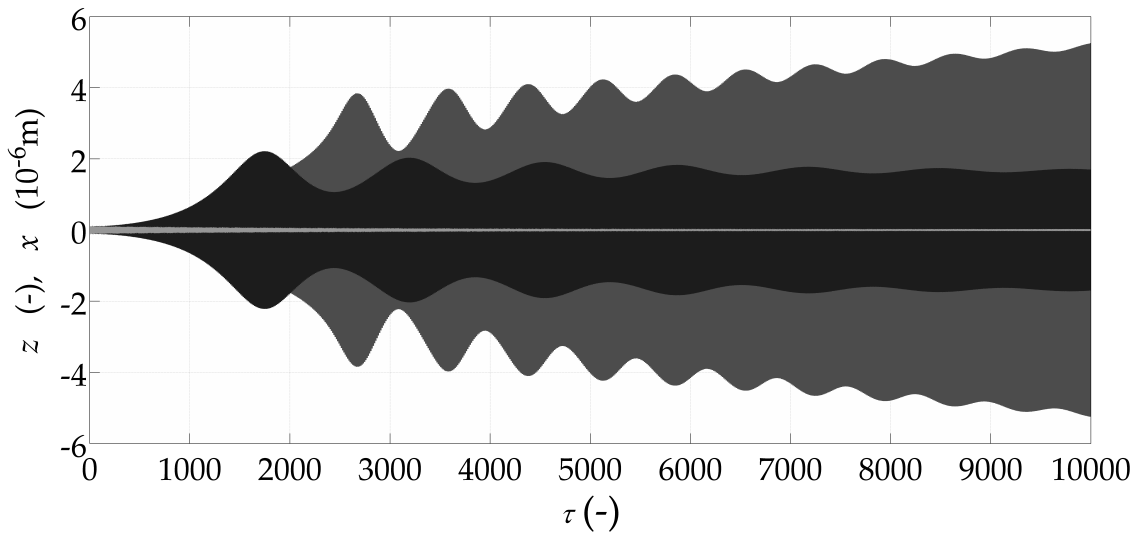


Figure 4.3: Time series of $z(\tau)$. Initial conditions: $r_0 = 0.1$, $\psi_0 = 0$. Black: $\sigma = 0$, light grey (foreground): $\sigma = 2$, dark grey (background): $\sigma = \sigma(\tau) = 2 \cdot 10^{-4}\tau$.

This behaviour does not change much qualitatively by increasing the PE frequency Ω towards the edge of the instability band of the trivial solution (black graph in Fig. 4.2). The system tends to the stable state much slower than for a value of Ω closer to the centre of the instability band. The amplitude of the stable limit cycle is predicted in Section 3.1.3 to be $r = |z| = 2.41$ by both the analytical and the semi-analytical approximation which agrees closely with the simulations carried out here.

The sharp transition between the basins of attraction of the trivial and the non-trivial stable states can also be validated by time simulation. For $\Omega = 2\omega_0 + 0.5\varepsilon$, a frequency outside the instability band of the branched solution, the motion can asymptote to either of the stable states—the trivial and the non-trivial—depending only on the initial conditions. For example, for the initial conditions $r = 1.2$, $\psi = 1.49$ the system converges to the trivial solution, but for the initial conditions $r = 1.3$, $\psi = 1.49$ the system converges to the non-trivial solution (grey graphs in Fig. 4.2).

A slow detuning of the PE frequency by $\sigma(\tau)$ shows how important the analyses of bifurcated limit cycles are, even for values of σ far away from the instability band of the trivial solution (see Fig. 4.3): Starting from initial conditions slightly disturbed from the rest position for a constant $\sigma = 0$, the system is attracted to the limit cycle $r = 1.70$, $\psi = 1.50$. For a constant $\sigma = 2$ the system is attracted to the rest position $r = 0$. But detuning the PE frequency slowly with $\sigma(\tau) = 2 \cdot 10^{-4}\tau$ makes the system follow the first branch leading to $r = 5.26$ for $\sigma(\tau) = 2$. This exemplifies that with a time dependent PE frequency, the system can be attracted to bifurcated limit cycles even at PE frequencies with a stable rest position.

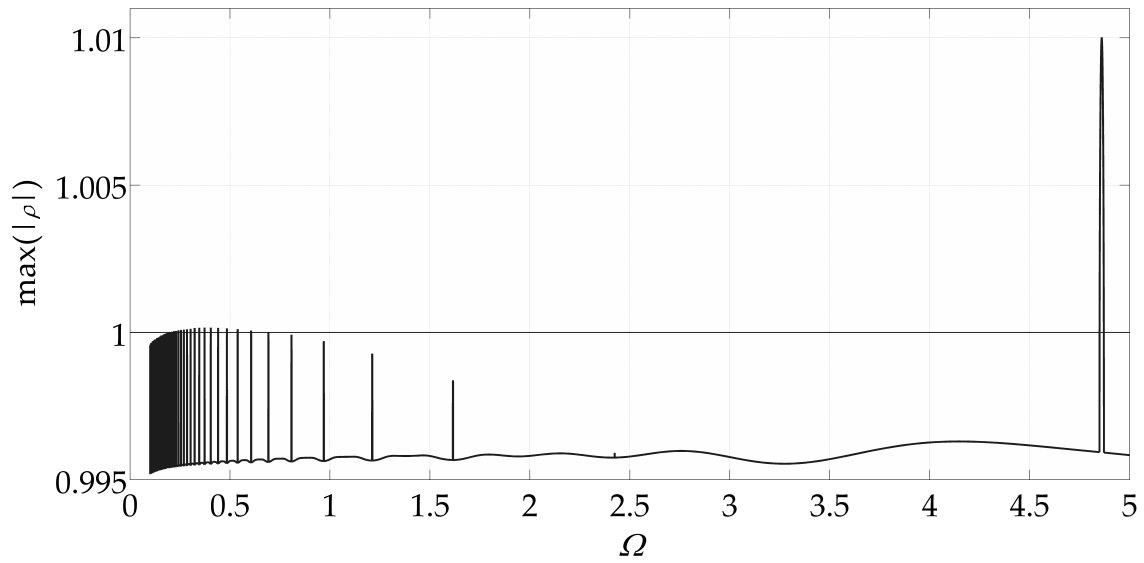


Figure 4.4: $\max(|\rho|)$ for the trivial solution $r = 0$. The trivial solution is unstable within a band around $\Omega_0 = 2\omega_0$.

A Floquet analysis reveals that the PR $\Omega = 2\omega_0$ is the only practically important instability of the rest position (see Fig. 4.4). Note that, as explained in Section 2.3, the Floquet multipliers have been normalised to the PE period T in order to compute quantitatively comparable values. As plotted, some further PR candidates may cause a $\max(\Re\{|\rho|\}) > 1$. The peaks are so narrow that the exact height might not be depicted correctly in all cases. However, in practice the bandwidth of these instability bands is too narrow to induce PR.

4.1.1 Numerical Results by a Continuation Method

As explained in Section 2.2.2 the limit cycles of solutions of differential equations can be found numerically employing numerical continuation. The MATLAB-based package MATCONT is used here. MATCONT can only handle first order differential equations and cannot handle harmonic terms. Thus Eq. (3.7) has to be rewritten as

$$z' = v, \quad (4.1a)$$

$$v' = -2\zeta \frac{\omega_0}{\Omega} v - \left(\frac{\omega_0^2}{\Omega^2} + \frac{\varepsilon_{\text{lin}}}{\Omega^2} c \right) z - \left(\frac{\kappa^2}{\Omega^2} + \frac{\varepsilon_{\text{nl}}}{\Omega^2} c \right) z^3 = 0, \quad (4.1b)$$

$$s' = s + c - s(s^2 + c^2), \quad (4.1c)$$

$$c' = c - s - c(s^2 + c^2). \quad (4.1d)$$

By path following MATCONT will find limit cycles. The amplitude $r = |z|$ of the limit cycles is calculated directly by $\max(z)$. At each state MATCONT will compute one periodic orbit in the z - v space. Neither s nor z necessarily have to be maximal for $\tau^* = \tau - \tau_{\text{start}} = 0$ (see Fig. 4.5). Since the PE has half the period of $z(\tau^*)$, defining a user function `psi1=acos(c)` calculates twice the effective phase shift $\psi_1^* = \psi_{1/2}$ of

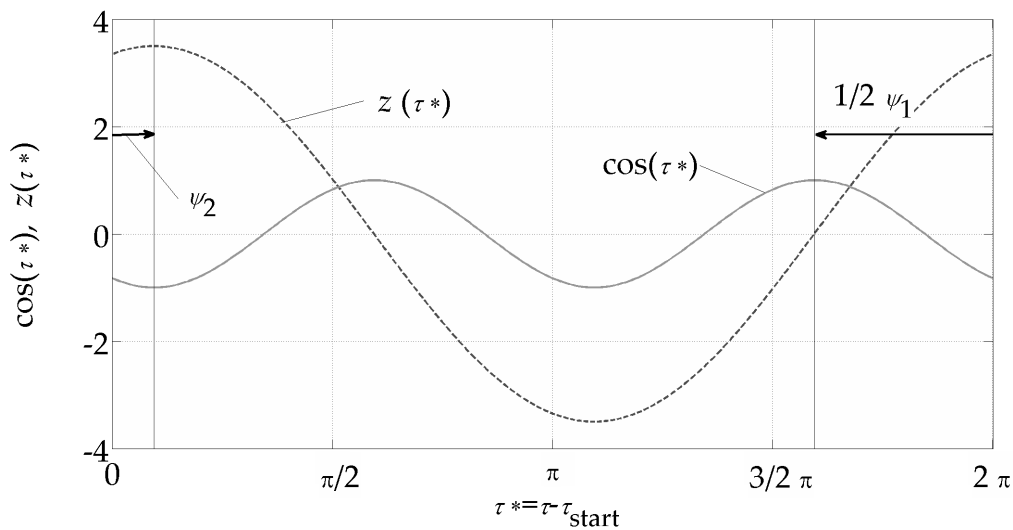


Figure 4.5: Periodic orbits for $c(\tau^*) = \cos(\tau^*)$ and $z(\tau^*)$. The phase shift between c and z is $\psi = \psi_1/2 - \psi_2 = \psi_1/2 + |\psi_2|$ because ψ_2 is negative.

$\cos(2(\tau + \psi_1^*))$ regarding $\tau^* = 0$. The phase shift of z regarding $\tau^* = 0$ can be computed from the results for z : its magnitude is $\text{psi2ABS} = \text{acos}(z_n(1)/\max(z_n))$ for the n th computed state. The phase shift between both harmonics is $\text{psi} = \text{psi1}/2 + \text{psi2ABS}$ because ψ_1 is positive and ψ_2 is negative. The bifurcated limit cycles are shown graphically in **Fig. 4.6** and **Fig. 4.7**. The stability of each state along the paths can be evaluated simultaneously while finding the limit cycles by computing their Floquet multipliers. It reveals the same stability behaviour as the analytic approach: the first loop is stable starting from the first branching $\sigma = -0.207$ until its reversal point, the second loop is stable starting from its reversal point for the states with larger amplitudes and phase shifts.

For large values of σ the approximations overestimate the amplitudes of the vibrations. This is because the approximations are only valid for small σ . When the amplitudes become large, the influence of the non-linear terms is underestimated by the approximation. The purely analytic approximation overestimates the amplitude of the stable limit cycle by 3.4% and the amplitude of the unstable limit cycle by 2.4% at $\sigma = 1.5$. The phase shift of the stable limit cycle is overestimated by 0.14 and the phase shift of the unstable limit cycle is underestimated by 0.15 at $\sigma = 1.5$. For the same reason that the amplitudes are overestimated, the transition between the loops is predicted by the approximations to happen at smaller values for σ than it actually does. In fact, the maxima and minima of the amplitude of the loops are the same in terms of numerical accuracy. The values of ψ at the reversal points of the phase shift loops also coincide. This means the numerically calculated loops are more stretched in the σ direction than the semi-analytically computed ones.

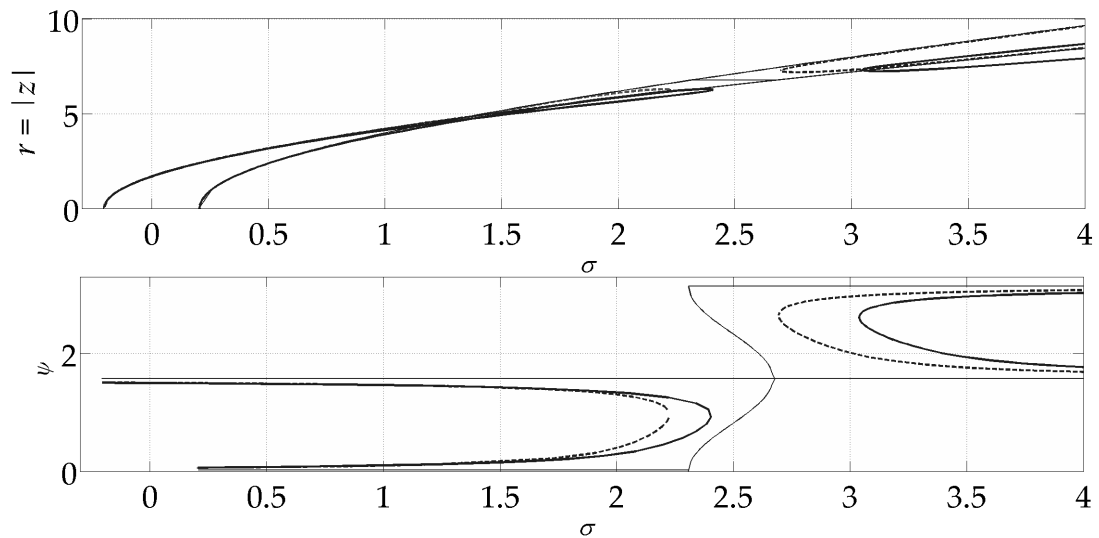


Figure 4.6: Limit cycles of Eqs. (3.15), Eqs. (4.1). Thin: analytical solution, bold and dashed: semi-analytical solution, bold and solid: numerical solution.

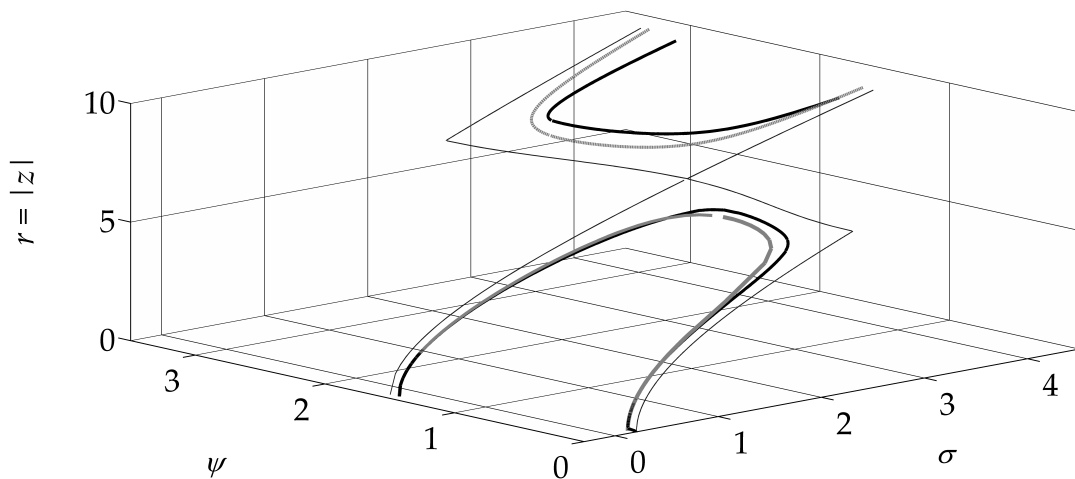


Figure 4.7: Limit cycles of Eqs. (3.15), Eqs. (4.1) in the phase parameter space. Thin: analytical solution, bold and grey: semi-analytical solution, bold and black: numerical solution.

4.1.2 Poincaré Maps and Borders of Basins of Attraction

At parameter values for which more than one stable solution exists, the question arises for a certain state whether the system is attracted to this or another stable state. A first approach to answer this question is to consider Poincaré maps which are plots of the projections of a system's trajectories into Poincaré sections. Latter are $(n - 1)$ -dimensional transversal hyperspaces with respect to the trajectories in the n -dimensional phase space. This means that for fixed σ the state space is observed periodically at $\tau = 4k\pi$. These maps can be derived numerically by iteration of the initial conditions and integration over one period of $z(\tau)$. The differences between the initial conditions and the final values are depicted as arrows (see **Fig. 4.9 - Fig. 4.16**). Due to the frequency ratio $\eta = 1/2$ the phase shift ψ is periodic in π (see **Fig. 4.8**). Because of a display problem of the arrow grid the Poincaré maps only extend to 3 instead of π .

Regarding the r - ψ phase space in the parameter range $\sigma_b \leq \sigma \leq 2$, two fixed points can be identified: one is a stable attractor (node), the other one is an unstable attractor (saddle point). The system is attracted by the saddle point from two opposing directions but repelled from the orthogonal directions. The line $r = 0$ also is a stable attractor (see **Fig. 4.9 - Fig. 4.12**). Studying a damped system the trivial steady state is stable for all $\sigma \notin \{-\sigma_b \leq \sigma \leq \sigma_b\}$. However, as this is an equilibrium and not a limit cycle, the phase shift can take on any value. Hence the trivial steady state is a line in the r - ψ phase space and a plane in the r - ψ - σ phase parameter space.

The attractors found coincide with the previously discussed results of the numerical path following of the first loop. If $\sigma > \sigma_b$ the trivial solution is stable as well as the states along the first branch. For values of σ smaller than the intersection of the branches the node has a larger amplitude than the saddle point. For values of σ greater than the intersection of the branches the node has a smaller amplitude than the saddle point.

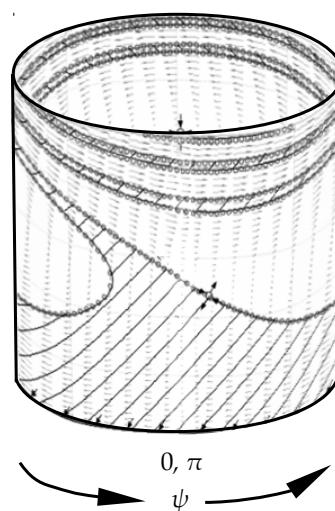


Figure 4.8: Coiled Poincaré map. The Poincaré maps are periodic in π .

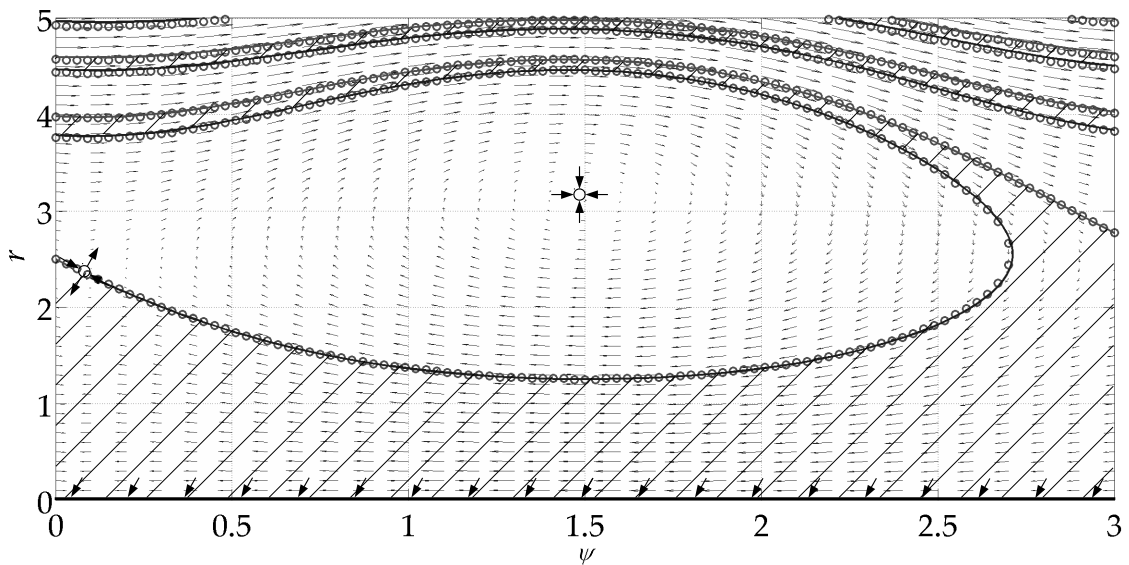


Figure 4.9: Poincaré map, ψ - r phase space, $\sigma = 0.5$. Two stable attractors: $[1.49, 3.16]$ and $[-, 0]$. One unstable attractor (saddle point): $[0.07, 2.42]$. Hatched: basin of attraction of the trivial solution. Limit of basins of attraction by numerical scanning (circles) and by backward time integration (line).

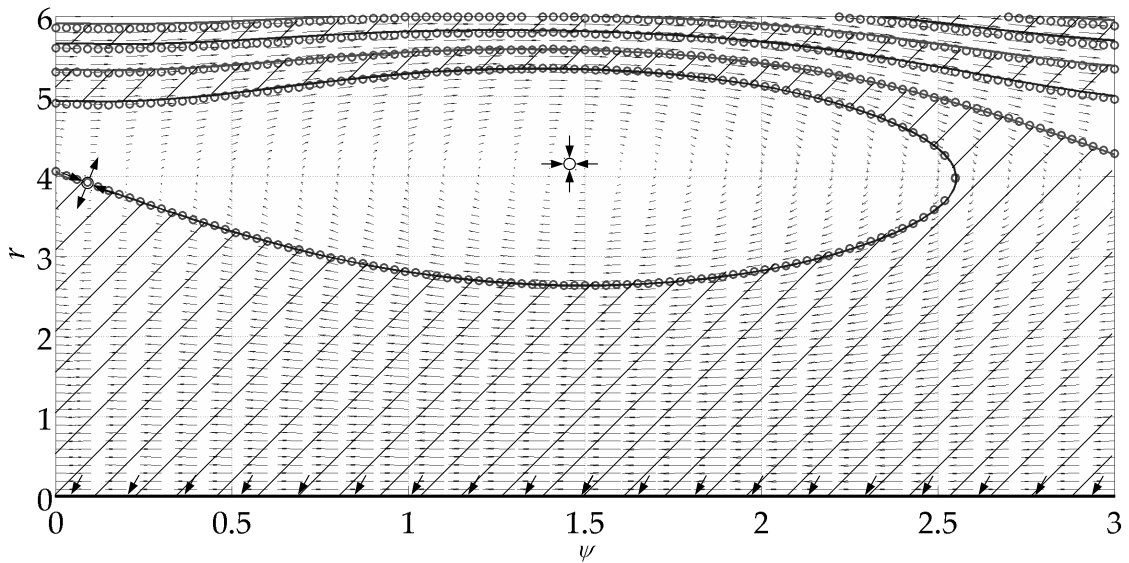


Figure 4.10: Poincaré map, ψ - r phase space, $\sigma = 1$. Two stable attractors: $[1.46, 4.15]$ and $[-, 0]$. One unstable attractor (saddle point): $[0.10, 3.90]$. Hatched: basin of attraction of the trivial solution. Limit of basins of attraction by numerical scanning (circles) and by backward time integration (line).

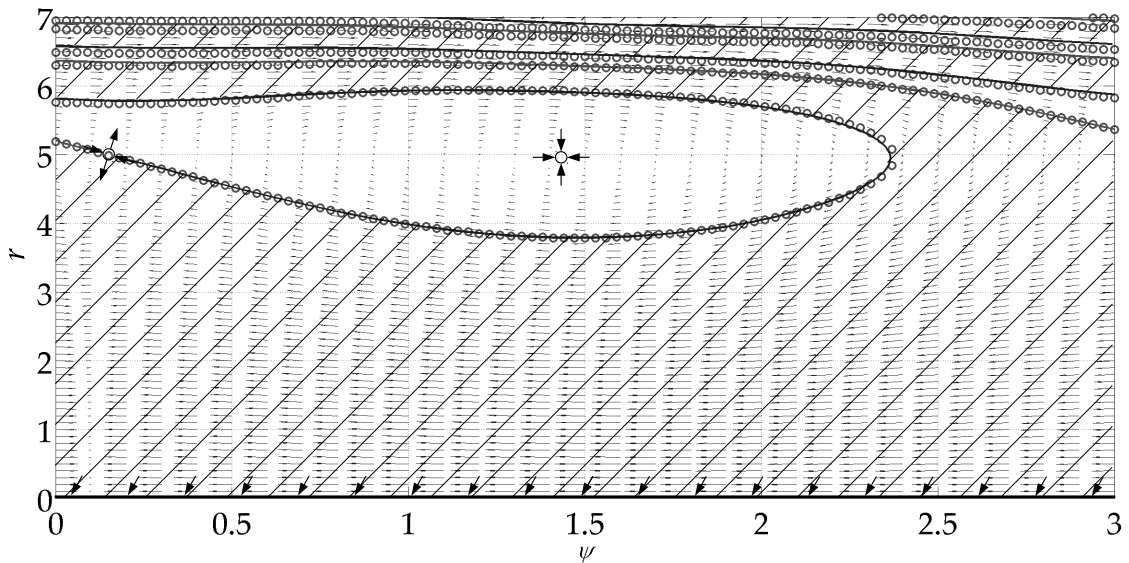


Figure 4.11: Poincaré map, ψ - r phase space, $\sigma = 1.5$. Two stable attractors: $[1.43, 4.94]$ and $[-, 0]$. One unstable attractor (saddle point): $[0.15, 4.99]$. Hatched: basin of attraction of the trivial solution. Limit of basins of attraction by numerical scanning (circles) and by backward time integration (line).

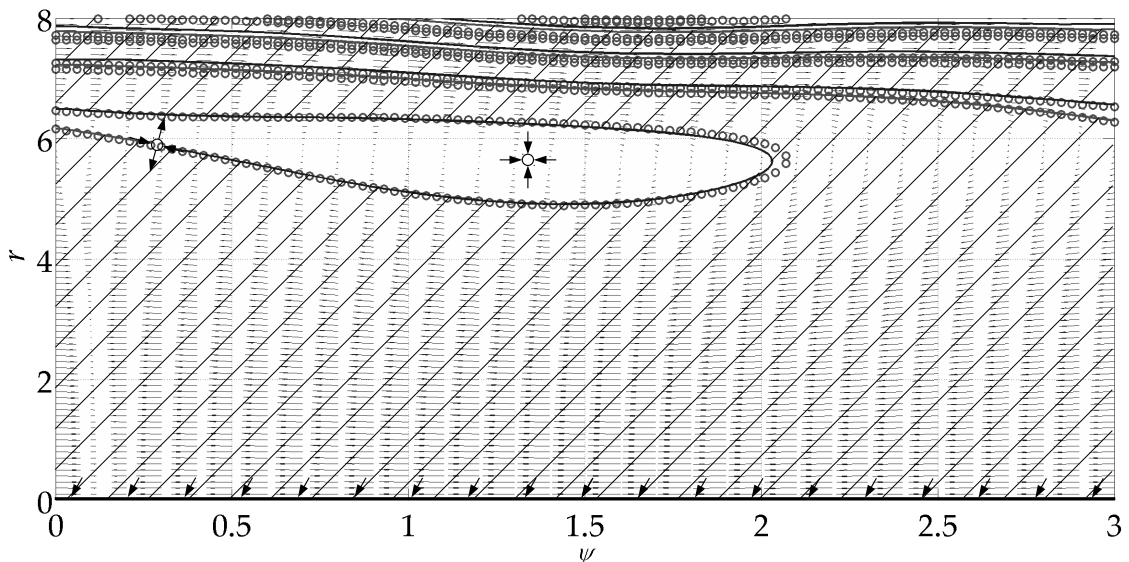


Figure 4.12: Poincaré map, ψ - r phase space, $\sigma = 2$. Two stable attractors: $[1.34, 5.65]$ and $[-, 0]$. One unstable attractor (saddle point): $[0.29, 5.87]$. Hatched: basin of attraction of the trivial solution. Limit of basins of attraction by numerical scanning (circles) and by backward time integration (line).

Although attractors can be identified from the Poincaré maps, without further investigation it is hard to tell by which state the system is attracted. The borders of the basins of attraction of each stable attractor have to be identified. This can be achieved by scanning the parameter space: The equation of motion is integrated over a sufficient time span for fixed σ iterating over initial values for r and ψ . Each initial value is then examined regarding which attractor is approached. The results are depicted as circles in Fig. 4.9 - Fig. 4.16. Despite the fact that this approach leads to satisfying results it has several disadvantages: first of all, it is computationally expensive because, depending on the resolution, a large number of states has to be examined. Secondly, the distance between two found points along the border depends on the gradient of the border at these states and the chosen resolution of the scanning. Although a relatively high resolution might be chosen regarding one axis, the resolution of the border may be insufficient, where the gradient of the border is orthogonal to this axis. Where the gradient of the border of the basins of attraction is in parallel to this axis, the resolution may be unnecessarily high. A more sophisticated approach, which aims at dealing with both problems, is integrating backwards in time starting at a point close to the border of the basins of attraction. Since on each side of the border the system will approach a stable attractor over time, going backwards in time the system's state will converge to the border. Since the system is attracted by the saddle point from two directions but repelled regarding the orthogonal directions, obviously the saddle point lies on the border between two basins of attraction. In fact, the border between the basins of attraction is the saddle point's stable manifold [23]. Hence a state nearby is a good initial value for a backward integration. In order to observe states in the Poincaré sectional plane a fixed time step integration has to be employed. Problems regarding step size control arise. Here the maximum step size was controlled by a globally allowed maximum difference between any state of the solution and a solution with half the step size.

Within the investigated parameter and variable ranges, both methods give satisfying and similar results. Adding the border of the basins of attraction to the Poincaré maps the behaviour of the system becomes more clear: for any state in the parameter range $\sigma_b \leq \sigma \leq 2$ with an amplitude larger than that of the node, the phase shift will increase steadily while the amplitude will oscillate decreasingly around the node. This coincides with the simulations studied previously. In the case where the system is attracted by the node, the phase shift will stop increasing steadily at one point and both amplitude and phase shift will converge to the attractor in an oscillatory manner. The system's state is trapped in an area close to the node by the repelling characteristic of the saddle point. Starting with large amplitudes, if the system is not attracted by the node, it is attracted first by the saddle point. The system is repelled then forcing the phase shift to decrease steadily, while the amplitude keeps modulating decreasingly and eventually approaches $r = 0$ asymptotically.

The difference in the results between the scanning and the backward integration increases towards the final values of the backward integration, because integration errors sum up. The node lies in an area with larger amplitude gradients and higher modulation

frequencies the more σ is increased. Here, an arbitrary example for illustration is given: The modulation frequency is 1.19 times larger for $\sigma = 1$ than it is for $\sigma = 0.5$. This means that for constant accuracy of the integration, the step size has to be decreased while increasing σ . Due to limited computational capacity the step size has not been decreased appropriately. The step size control was set to lower accuracy for larger values of σ . This causes the differences between the scanning and the backward integration to increase for increasing σ .

Transforming the r - ψ phase space into

$$z_0 = r \cos(4k\pi + \psi), \quad (4.2a)$$

$$z'_0 = -\frac{1}{2}r \sin(4k\pi + \psi) \quad (4.2b)$$

gives another perspective to the problem (see **Fig. 4.13** - **Fig. 4.16**). The trivial solution $r = 0$, $\psi = -$ shrinks to the node $z_0 = 0$, $z'_0 = 0$. Due to the harmonics, both non-trivial attractors duplicate to conjugate couples. Because of the extreme differences within the observed region the length l_{real} of the vectors between initial and final values (arrows in Poincaré maps) was scaled to the plotted length $l_{\text{plot}} = l_{\text{real}}^{4/5}$.

No matter which phase space variables are employed to observe the system, it becomes clear that the non-trivial node is very dominant at values of σ close to the second branch point $\sigma = \sigma_b$. The distance between the border of the basins of attraction and the trivial stable attractor is small. States with amplitudes larger than that of the non-trivial node are mainly attracted by this state (see **Fig. 4.9** and **Fig. 4.13**). For increasing values of σ , the trivial attractor becomes more dominant. The distance between the border of the basins of attraction and the trivial attractor increases. States with amplitudes larger than that of the non-trivial node become more likely to be attracted by the trivial attractor (see **Fig. 4.12** and **Fig. 4.16**).

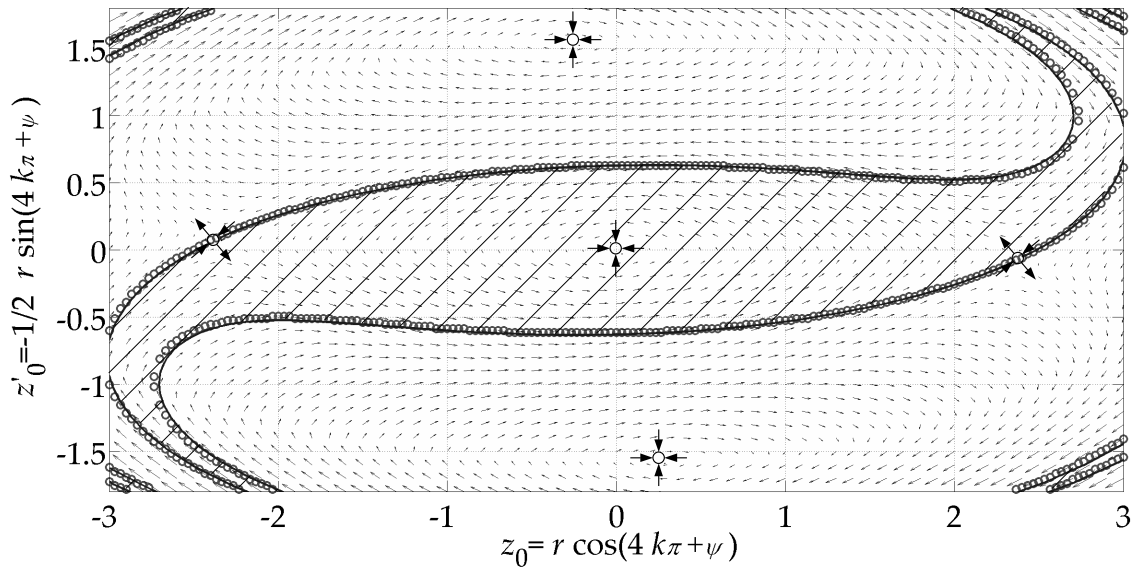


Figure 4.13: Poincaré map, z - z' phase space, $\sigma = 0.5$. Three nodes: $[\pm 0.26, \mp 1.58]$ and $[0, 0]$. Two saddle points: $[\pm 2.41, \mp 0.09]$. Hatched: basin of attraction of the trivial solution. Limit of basins of attraction by numerical scanning (circles) and by backward time integration (line).

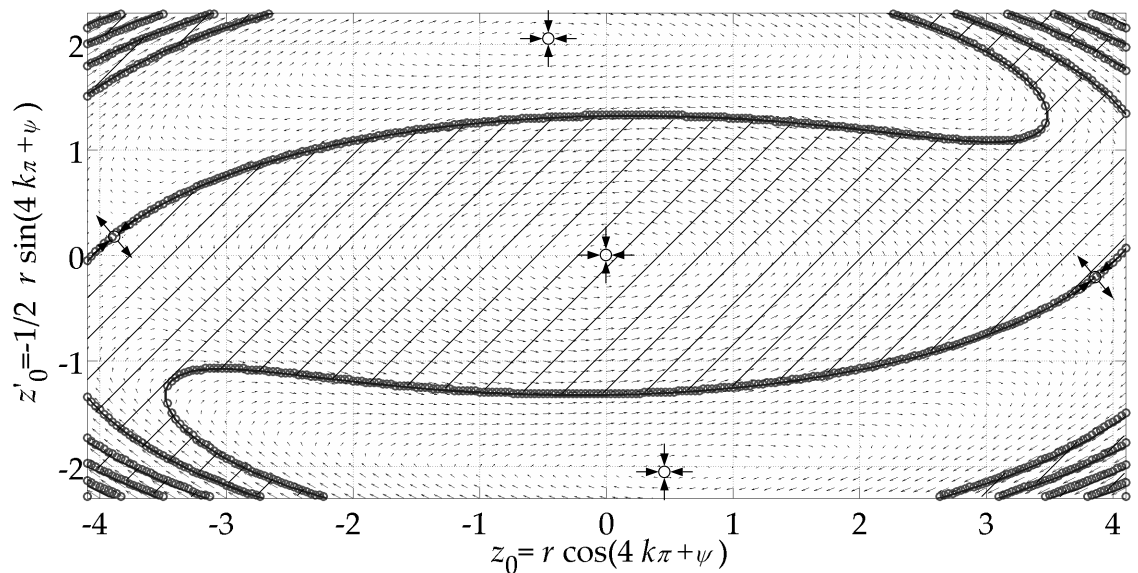


Figure 4.14: Poincaré map, z - z' phase space, $\sigma = 1$. Three nodes: $[\pm 0.46, \mp 2.06]$ and $[0, 0]$. Two saddle points: $[\pm 3.88, \mp 0.20]$. Hatched: basin of attraction of the trivial solution. Limit of basins of attraction by numerical scanning (circles) and by backward time integration (line).

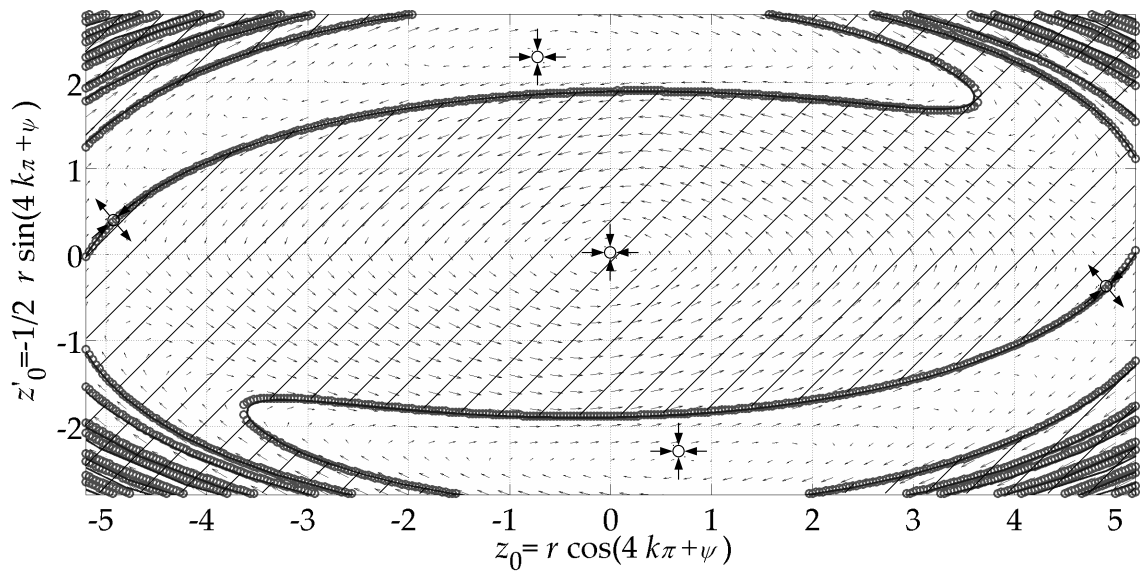


Figure 4.15: Poincaré map, z - z' phase space, $\sigma = 1.5$. Three nodes: $[\pm 0.69, \mp 2.45]$ and $[0, 0]$. Two saddle points: $[\pm 4.93, \mp 0.37]$. Hatched: basin of attraction of the trivial solution. Limit of basins of attraction by numerical scanning (circles) and by backward time integration (line).

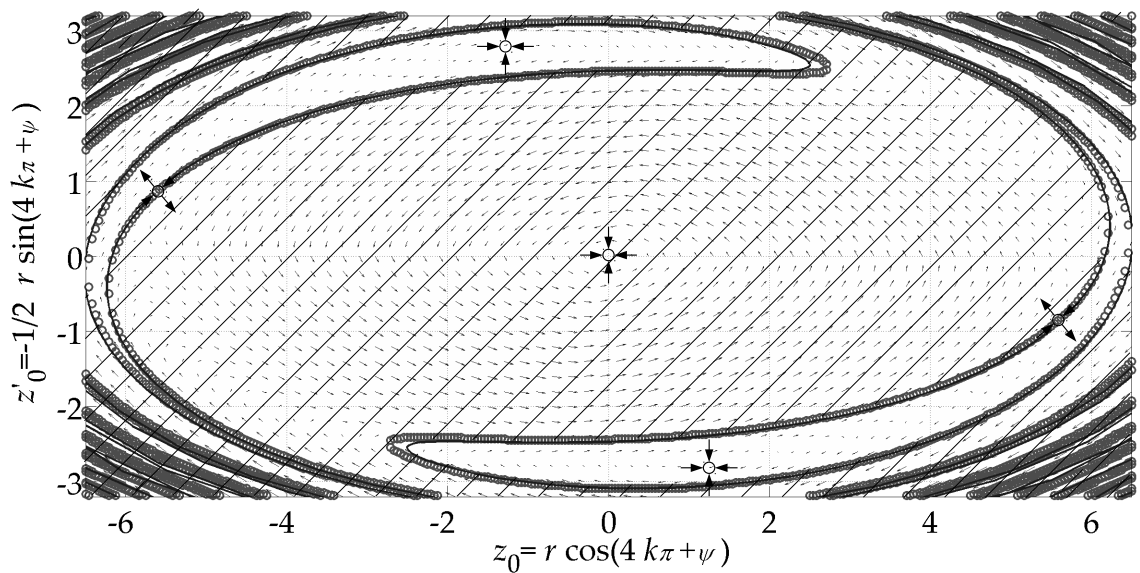


Figure 4.16: Poincaré map, z - z' phase space, $\sigma = 2$. Three nodes: $[\pm 1.29, \mp 2.75]$ and $[0, 0]$. Two saddle points: $[\pm 5.63, \mp 0.84]$. Hatched: basin of attraction of the trivial solution. Limit of basins of attraction by numerical scanning (circles) and by backward time integration (line).

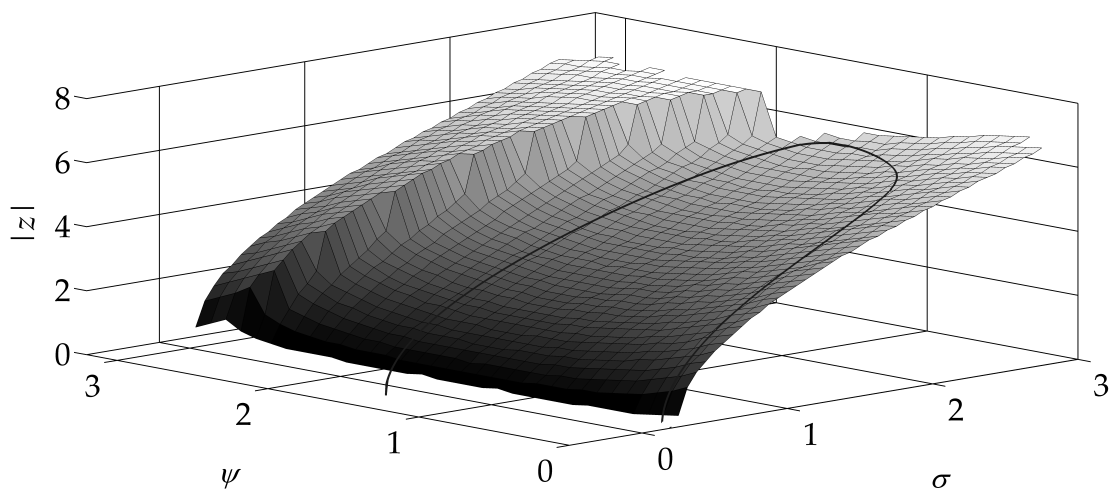


Figure 4.17: Lowest border (surface grid) between the basins of attraction of the bifurcated limit cycle (line) and stable trivial solution (rest position) ($[>0.223,-,0]$ plane) in the σ - ψ - z parameter-phase-space.

Plotting the lowest border between the basins of attraction of the stable non-trivial, branched solution and the trivial solutions in the z - ψ - σ phase parameter space gives a better understanding of the dependence of this border on σ . The degree of the ability of the non-trivial node to attract the system determines how likely it is that, for PE frequencies with $\sigma > \sigma_b$, the system may not be attracted by the trivial solution after some initial disturbance, but will approach the non-trivial solution. The characteristic regarding this behaviour may be of vital interest in order to ensure that the system does not approach branched attractors for PE frequencies outside the instability band of the trivial attractor.

To be able to compare the power of the trivial solution to attract the system for different parameter sets the following measure P is introduced

$$P = \frac{r_{\text{border}}}{|z|} \Big|_{\sigma=2\sigma_b}. \quad (4.3)$$

Here r_{border} is the amplitude of z at the lowest border of the basin of attraction between the non-trivial and the trivial attractor at the same phase shift ψ as the non-trivial attractor. P measures how close the lowest border of the basin of attraction between the non-trivial and the trivial attractor is to the non-trivial attractor. It can take on values within the interval $[0; 1]$. A value $P = 0$ means that the space of the basin of attraction of the trivial attractor is zero. A value $P = 1$ means the space of the basin of attraction of the non-trivial attractor is zero. Hence P is a measure of how likely it is for system to be attracted by the trivial attractor starting from a small but non-zero amplitude. For the parameter set studied here this measure takes on the value $P = 0.28$.

In this section, the behaviour of a 1DOF system described in Section 3.1.1 was analysed numerically at PR using a continuation method. The results were compared to analytical and semi-analytical approximations obtained in Section 3.1.3. The relevance of the found attractors was discussed by investigating their basins of attraction.

4.2 Numerical Investigations of the Two Degree of Freedom System

The 1DOF system investigated in Section 4.1 was extended to a 2DOF system in Section 3.2.1. As before for the 1DOF system, the rest position's stability is investigated first showing the values for PE frequencies of parametric resonances and anti-resonances. Time simulations clarify the behaviour at different PE frequencies and for various parameter regimes and initial conditions. The analytical and semi-analytical approximations of limit cycles at PR in Section 3.2 are validated numerically. In particular, the accuracy of the quasi-modally reduced model is discussed. The borders of the basins of attraction of the detected limit cycles are computed numerically.

As explained in Section 2.1, a 2DOF system behaves quantitatively different to a 1DOF system. In analogy to the Floquet analysis of the 1DOF system, the PRs at $\Omega = 2\omega_1$ and $\Omega = 2\omega_2$ can be identified (see **Fig. 4.18**). The same as for the 1DOF system, a normalisation with respect to the PE period T of the Floquet multipliers was employed (see Section 2.3). As the maximum Floquet multiplier has almost the same magnitude at the first and second PR, the system will be repelled by the trivial steady state equally fast at both PRs. However, this does not give information about the amplitudes of the branched solutions. Another instability band becomes apparent at $\Omega = \omega_1 + \omega_2$, which is the first parametric combination resonance (PCR). This can be validated by time simulations (see **Fig. 4.19**). In contrast to PRs, at PCRs both modes are excited. As the amplitudes of both quasi-modes z_1 and z_2 are the same order of magnitude, both quasi-modes influence the physical displacements x_1 and x_2 similarly. The resulting interferences lead to time series which, in contrast to the behaviour at PRs, cannot be approximated with a modulated cosine. The PR candidate at $\Omega = \omega_1$ has some effect (see **Fig. 4.18**), in the way that here the system is attracted by the trivial solution slower than at slightly larger or smaller PE frequencies. However, as indicated by the maximum Floquet multiplier $\max(\Re\{|q|\}) < 1$, the PE frequency $\Omega = \omega_1$ does not destabilise the trivial solution.

As explained in Section 2.1.2, in contrast to the 1DOF system, the 2DOF system also experiences a parametric anti resonance (PAR) at a PE frequency $\Omega = \omega_2 - \omega_1 = 0.8481$. The value of the maximum Floquet multiplier of the trivial solution is slightly smaller than compared to a PE frequency outside the PAR (see **Fig. 4.18**). This indicates a faster attraction of the system by the trivial solution from a disturbed state (see **Fig. 4.20**). However, the effect of the PAR is not very distinct regarding the displacement x_1 of the first body. It is more visible regarding the displacement x_2 of the second body. With the initial conditions $z_1 = z_2 = [1, 0]^T$ the amplitudes of the displacement x_2 of the second body decay 1.58 times faster at PAR than without PE. Considering the quasi-modes z_1 and z_2 , the periodic energy transfer between them becomes visible by the modulation of both time series. The amplitude of the first quasi-mode z_1 decays faster, the amplitude of the second quasi-mode z_2 decays slower compared to no PE or PE outside PAR. The higher modal damping ζ_2 is used more effectively and the energy is dissipated faster.

The analytical and semi-analytical approximations in Section 3.2.4 suggest that the borders of the basins of attraction of the first and second stable limit cycles come to lie close to each other for the first PR $\Omega = 2\omega_1$ (see **Fig. 3.8** and **Fig. 3.9**). Indeed, not only the borders of these two, but the borders of all three basins of attraction are very close to each other at this PR. Starting with same amplitudes $r_0 = [140, 0]^T$ and varying the initial phase shift $\psi_0 = [\{0.4, 0.5, 0.6\}, 0]^T$ slightly, the system ends up on the three different states (see **Fig. 4.21**).

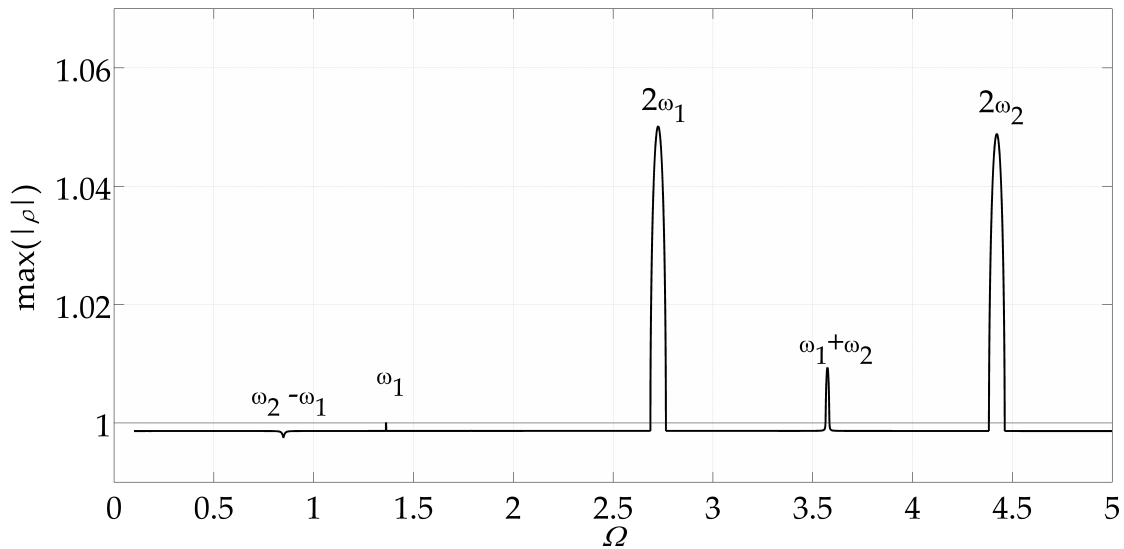


Figure 4.18: Maximum Floquet multiplier $\max(|\rho|)$ for the trivial solution $r_1 = r_2 = 0$. The trivial solution is unstable within a band around $\Omega = 2\omega_1$, $\Omega = 2\omega_2$ and $\Omega = \omega_1 + \omega_2$ (PRs). Note the parametric anti-resonance at $\Omega = \omega_2 - \omega_1$.

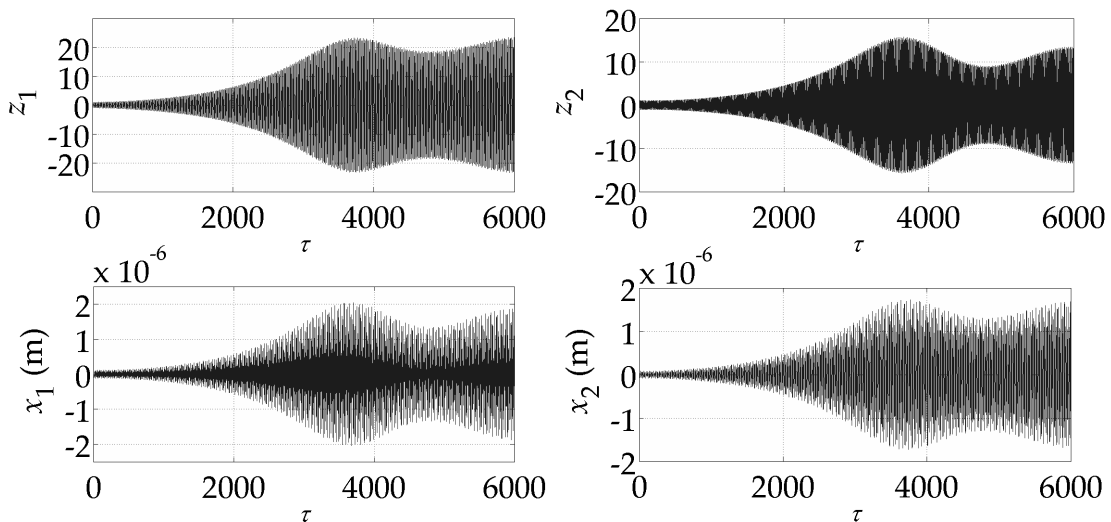


Figure 4.19: Time series at PCR ($\Omega = \omega_1 + \omega_2 = 3.5737$) and initial conditions $z_1 = z_2 = [1, 0]^T$. Quasi-modal displacements z_1 and z_2 and physical displacements x_1 and x_2 .

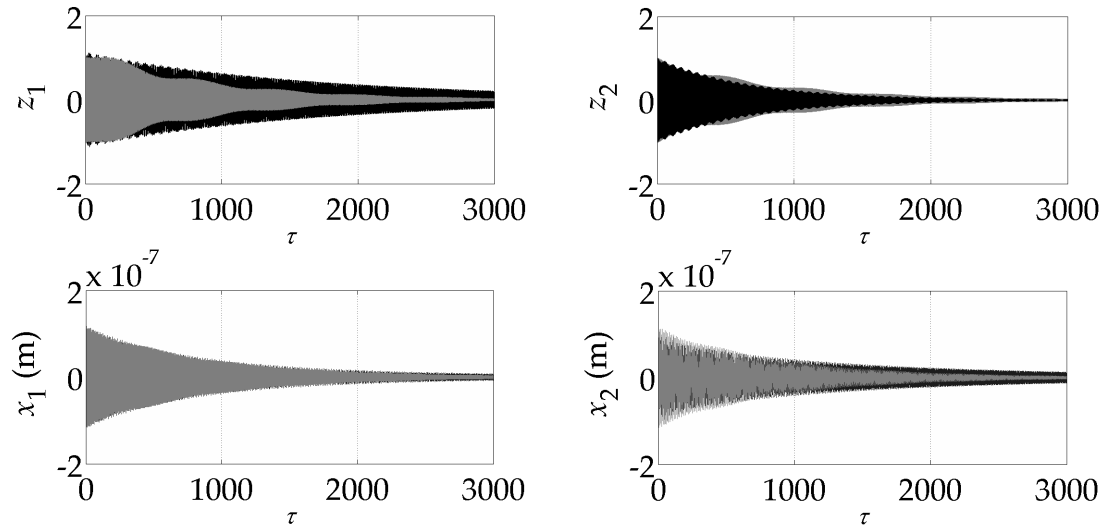


Figure 4.20: Time series at PAR $\Omega = \omega_2 - \omega_1 = 0.8481$ (grey) and at $\Omega = 0.95$ (black) for comparison. Initial conditions $z_1 = z_2 = [1, 0]^T$. Quasi-modal displacements z_1 and z_2 and physical displacements x_1 and x_2 .

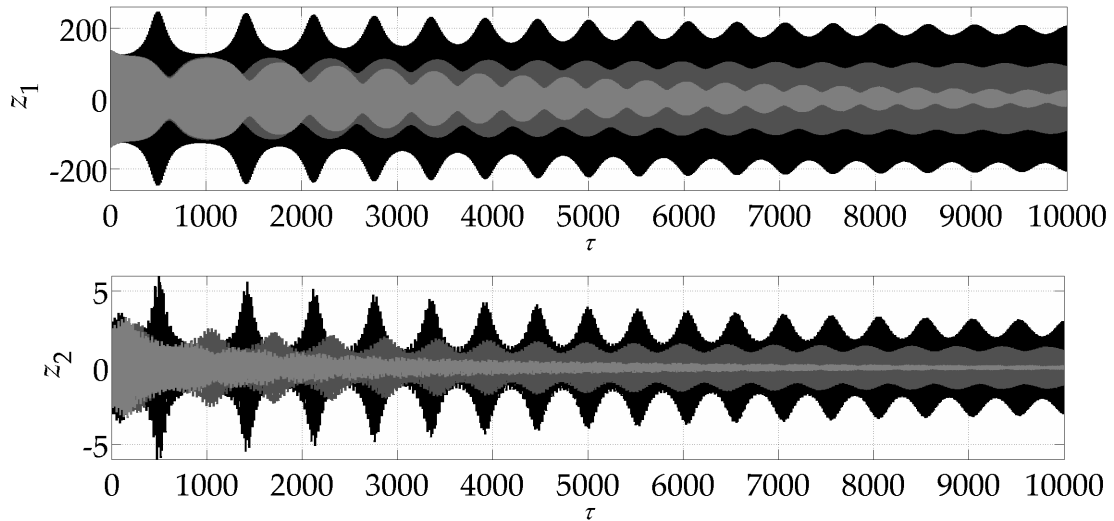


Figure 4.21: Time series at first PR ($\Omega_0 = 2\omega_1$), $\sigma = 0.6$. Initial conditions: $r_0 = [140, 0]^T$, $\psi_0 = [\{0.4, 0.5, 0.6\}, 0]^T$. Starting with $\psi_{1,0} = 0.4$ the system is attracted by the first non-trivial stable attractor (dark grey), starting with $\psi_{1,0} = 0.5$ by the trivial steady state (light grey) and starting with $\psi_{1,0} = 0.6$ by the second non-trivial stable attractor (black).

4.2.1 Numerical Results by a Continuation Method

Employing the MATLAB-based package MATCONT, the results depicted in **Fig. 4.24** - **Fig. 4.27** can be found numerically. If these results are compared to results of numerical continuations for the appropriately reduced 1DOF systems (see Section 3.2.4) an extremely good agreement can be observed regarding the first PR ($\Omega_0 = 2\omega_1$) and slightly worse agreement regarding the second PR ($\Omega_0 = 2\omega_2$) (see **Fig. 4.22** and **Fig. 4.23**). The maximum difference for $|z_1|$ at the first PR between the 1DOF and the 2DOF model is -0.93%. The maximum difference for $|\psi_1|$ at the first PR between the 1DOF and the 2DOF model is -0.74%. The maximum difference for $|z_2|$ at the second PR between the 1DOF and the 2DOF model is 3.3%. The maximum difference for $|\psi_2|$ at the second PR between the 1DOF and the 2DOF model is 9.5%. The largest differences occur at the reversal points of the loops. Apart from these reversal points the results match within the numerical limits. This validates the accuracy of the 1DOF modelling approach. The transition from one loop to the other is predicted to happen at smaller σ by the 1DOF model than by the 2DOF model. This effect is stronger regarding the second PR. To explain this behaviour one has to remember that for modelling the 2DOF system as a 1DOF system, not only terms of the more weakly excited quasi-mode but also mixed terms, where both first and second quasi-mode occur, are neglected. As can be seen by the strong softening behaviour (compare σ ranges in **Fig. 4.22** and **Fig. 4.23**) regarding the second PR, non-linear terms have a more significant influence on the second PR than they have on the first one. This can be expounded by the growing error by neglecting mixed terms when having larger amplitudes of the vibration. The effect explains both the growth of the deviation between amplitudes

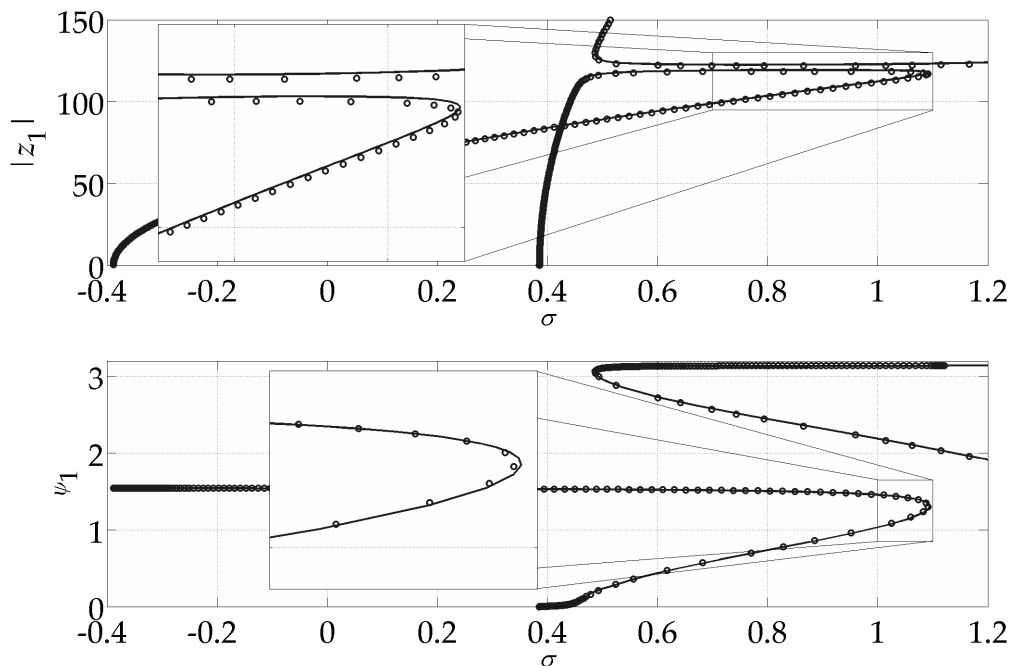


Figure 4.22: Numerical continuation, first quasi-mode z_1 , first PR ($\Omega_0 = 2\omega_1$). 2DOF system (line) and reduced 1DOF model (circles).

for the 1DOF and the 2DOF model and the inaccuracies regarding the transition between the loops.

In analogy to the 1DOF system, for both resonances each first loop is stable starting from the first branching $\sigma = -0.387/\sigma = -0.396$ until its reversal point. The second loops are stable starting from their reversal points for the states with larger amplitudes and phase shifts. This is in agreement with the previously obtained analytic and semi-analytic results.

Amplitude and phase shift of the first quasi-mode z_1 at the first PR found by the analytical, the semi-analytical and the numerical methods agree very well within the instability band of the trivial solution (see **Fig. 4.24**). For larger values of σ , the amplitudes of the stable states differ more from each other. This inaccuracy does not result from approximating the 2DOF system with an 1DOF model as shown earlier, but solely because the influence of higher order terms was neglected in the analytical and the semi-analytical approach. Hence the non-linear softening behaviour is underestimated for large values of z_1 .

In the same manner as for the first quasi-mode z_1 , amplitude and phase shift of the second quasi-mode z_2 at the first PR detected by the different methods also match very well (see **Fig. 4.25**). Again, the amplitudes of the stable states differ more from each other for larger values of σ . Other than for the first quasi-mode, this inaccuracy of the analytical and the semi-analytical method partly results from approximating the 2DOF system with an 1DOF model as shown earlier. In addition the influence of higher order terms was neglected in the analytical and semi-analytical approach. Once more, the non-linear softening behaviour is underestimated, this time for large values of z_2 .

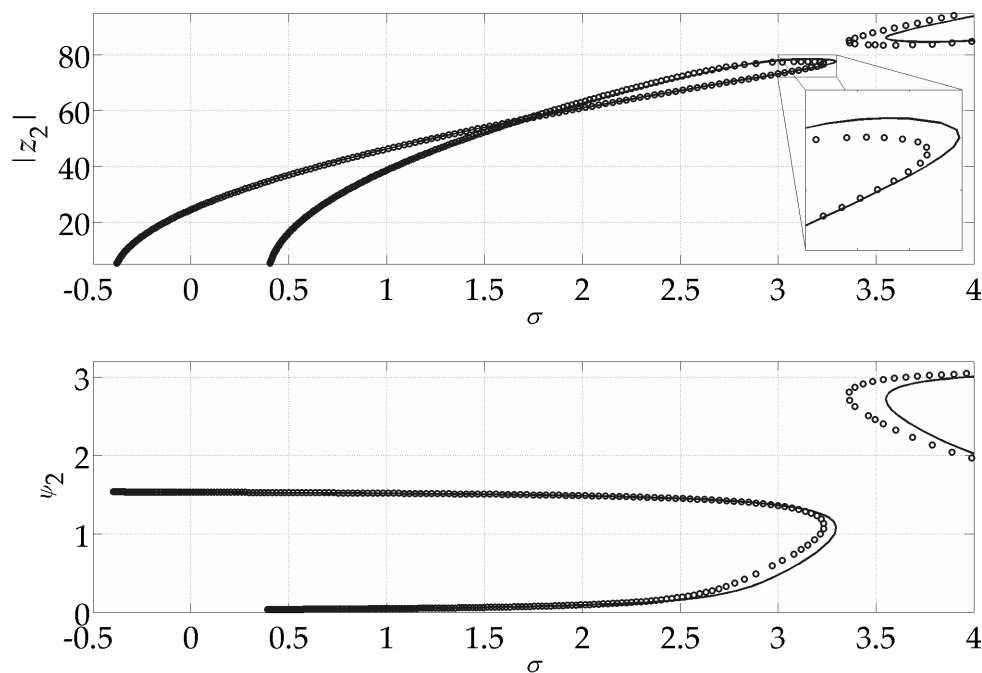


Figure 4.23: Numerical continuation, second quasi-mode z_2 , second PR ($\Omega_0 = 2\omega_2$). 2DOF system (line) and reduced 1DOF model (circles).

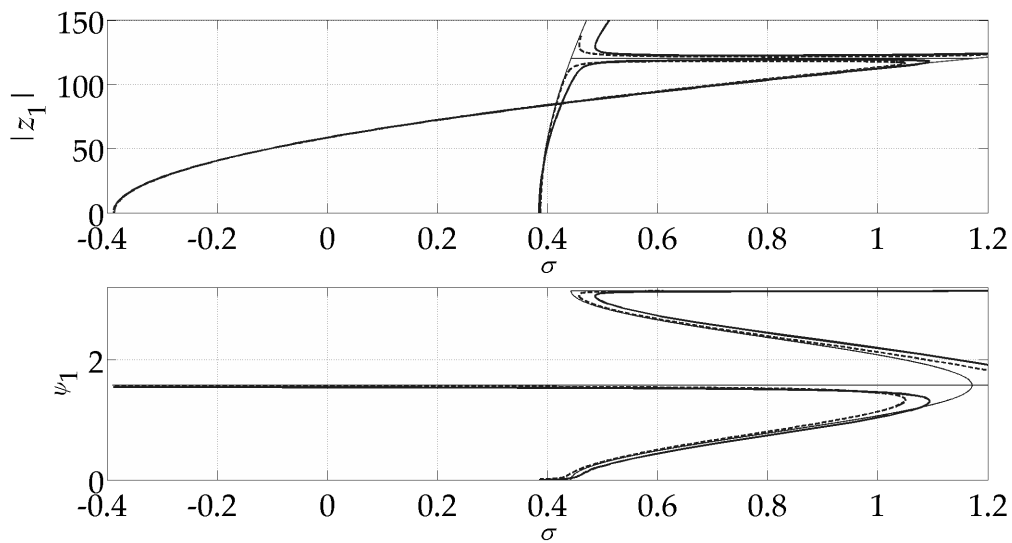


Figure 4.24: Limit cycles of Eqs. (3.48) for the first quasi-mode $z_1(\tau)$ at $\Omega_0 = 2\omega_1$. Thin: analytical approximation, bold and dashed: semi-analytical approximation, bold and solid: numerical solution.

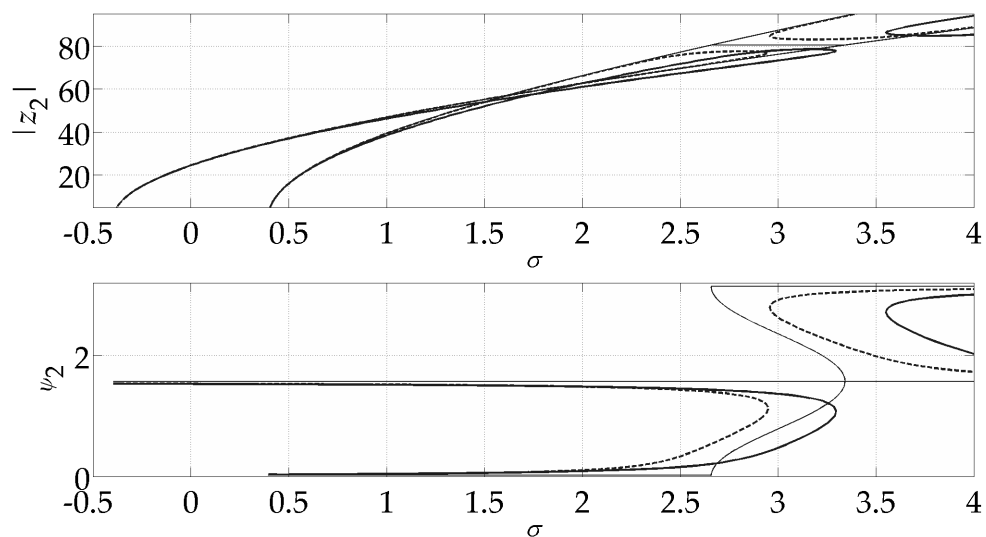


Figure 4.25: Limit cycles of Eqs. (3.48) for the second quasi-mode $z_2(\tau)$ at $\Omega_0 = 2\omega_2$. Thin: analytical approximation, bold and dashed: semi-analytical approximation, bold and solid: numerical solution.

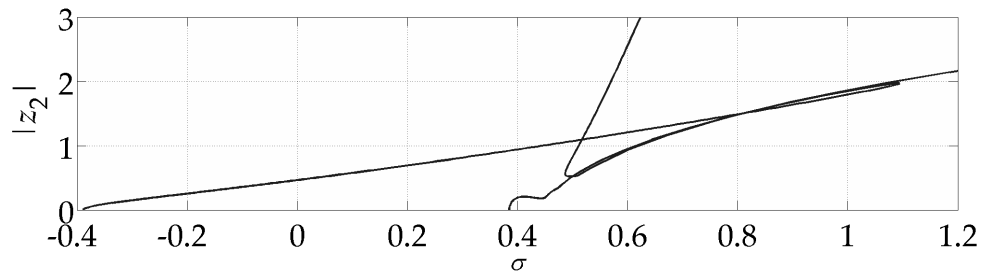


Figure 4.26: Amplitudes of the limit cycles of Eqs. (3.48) for the second quasi-mode $z_2(\tau)$ at the first PR ($\Omega_0 = 2\omega_1$) by numerical continuation.

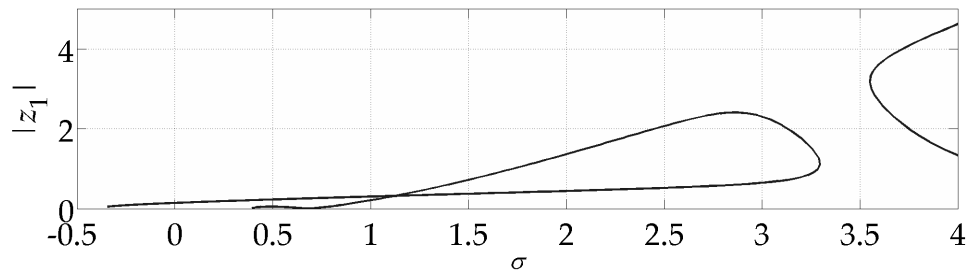


Figure 4.27: Amplitudes of the limit cycles of Eqs. (3.48) for the first quasi-mode $z_1(\tau)$ at the second PR ($\Omega_0 = 2\omega_2$) by numerical continuation.

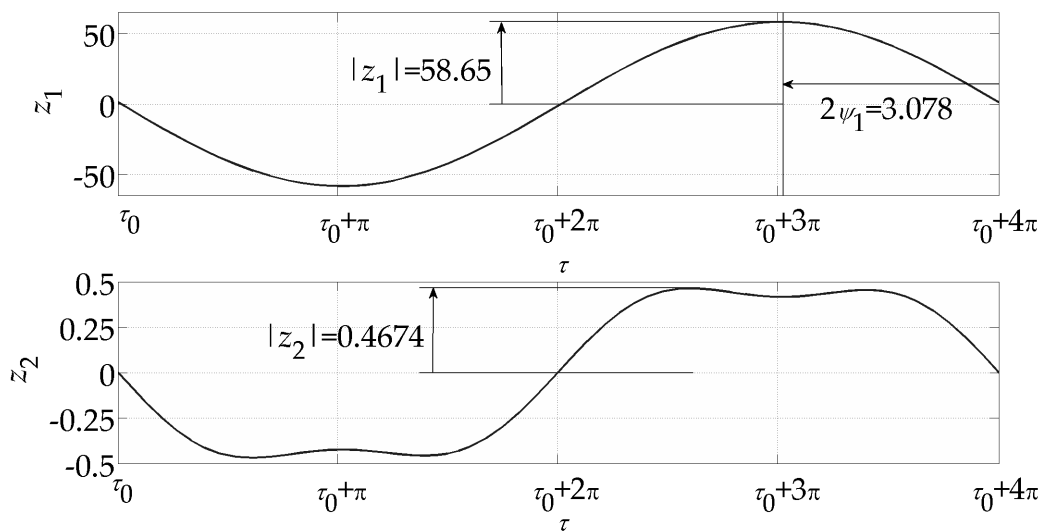


Figure 4.28: Both quasi-modes z_1 and z_2 at stable limit cycles at the first PR ($\Omega_0 = 2\omega_1$), $\sigma = 0$. Note the presence of at least two harmonics regarding the second quasi-mode.

Regarding the weakly excited quasi-modes, complex branches are found using the numerical continuation (see **Fig. 4.26** and **Fig. 4.27**). The amplitudes are very small compared to the amplitudes of the more strongly excited quasi-mode. As can be found by investigating the time series of the quasi-modes at the first PR (see **Fig. 4.28**) the period of the second quasi-mode is the same as the one of the first quasi-mode and not $\frac{\omega_1}{\omega_2}$ times smaller, as one may expect. Also, at least two frequencies are present in the oscillation. Hence the phase shift cannot be computed by the scheme as described in Section 4.1.1. The presence of two frequencies and the unexpected periodicity regarding the second quasi-mode both show the limits of the quasi-modal transformation. Nevertheless, the numerical continuation is capable of finding the amplitudes of the stable orbits of both z_1 and z_2 . Note that studying the behaviour of the the system in the z_i - σ projection of the phase parameter space can be very misleading. Since no information of the phase shift is given, both loops of the second quasi-mode at first PR seem to overlap partly (see **Fig. 4.26**). This is not necessarily the case, because even if the amplitudes are similar, this may not hold for the phase shift.

As for the 1DOF system, the bifurcated limit cycles at both PRs can be displayed best in a three dimensional reduced phase parameter space (see **Fig. 4.29** and **Fig. 4.29**). Nevertheless, while such a plot is completely sufficient regarding the 1DOF system, it is not for the 2DOF. Each state of the system could only be displayed sufficiently in a five dimensional phase parameter space. In addition to graphical problems such display is not possible because the phase shift of the less excited quasi-mode cannot be determined satisfactorily. However, the less excited quasi-modes play an insignificant role only, and displaying the results in a reduced phase parameter space at least gives information for the amplitude and the phase shift at the same time.

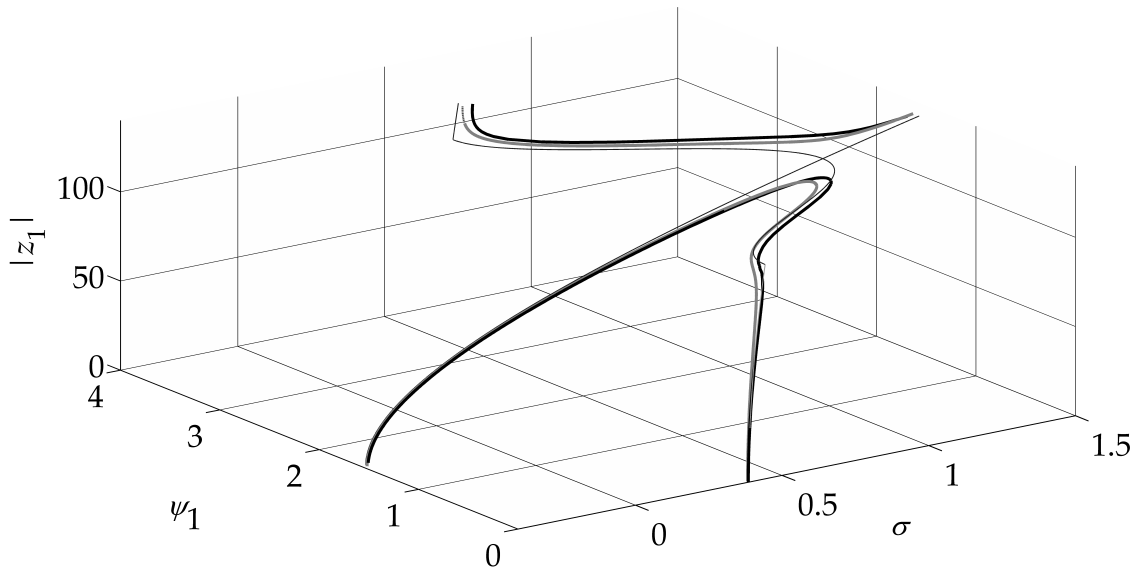


Figure 4.29: Limit cycles of Eqs. (3.48) for the first quasi-mode $z_1(\tau)$ at $\Omega_0 = 2\omega_1$. Thin: analytical approximation, bold and dashed: semi-analytical approximation, bold and solid: numerical solution.

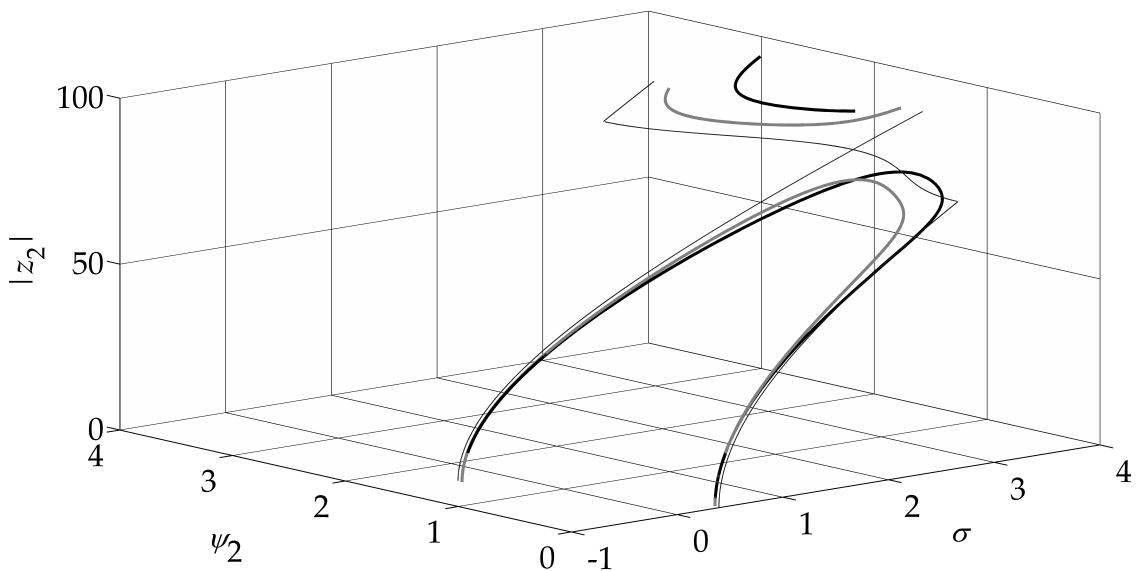


Figure 4.30: Limit cycles of Eqs. (3.48) for the second quasi-mode $z_2(\tau)$ at $\Omega_0 = 2\omega_2$. Thin: analytical approximation, bold and dashed: semi-analytical approximation, bold and solid: numerical solution.

4.2.2 Poincaré Maps and Borders of Basins of Attraction

In analogy to the 1DOF system, Poincaré maps for certain values of the PE frequency provide information about the attraction of the stable states. Here however, the Poincaré maps are not only a projection of the state space into the Poincaré space which only comprises states at times $\tau = 4k\pi$. In contrast to the 1DOF system, the five-dimensional state space has to be reduced first to a three dimensional state space which ignores the less excited quasi-mode. The Poincaré maps give information on the slow frequency modulation, but not about changes of the phase shift nor of the amplitude within one period 4π .

Borders of the basins of attraction can be computed by iteration over the phase space and by backwards integration (see Section 4.1.2). Together with the Poincaré maps they give sufficient information by which state the system will be attracted depending on the initial state.

Regarding the first PR ($\Omega_0 = 2\omega_1$) for $\sigma = 0$ only one stable attractor (node) can be found (see Fig. 4.31). It is the state of the first branched solution. The trivial solution is unstable at this frequency and thus provides two unstable attractors (saddle points) $[\frac{1}{4}\pi, 0]$ and $[\frac{3}{4}\pi, 0]$. As the non-trivial attractor is the only stable attractor the system is attracted by this state starting from all possible initial conditions. Increasing σ beyond the second branch point stabilises the trivial solution (see Fig. 4.32). Also, the unstable part of the branched solution becomes visible as a saddle point. The system now is attracted by the trivial attractor starting with certain initial conditions. This basin of attraction is very small compared to the basin of attraction of the non-trivial attractor. Starting from most states with amplitudes larger than the amplitude of the saddle point the amplitude decreases and the phase shift increases steadily. The system is attracted by the saddle point first and once repelled by it, approaches the node asymptotically in an oscillatory

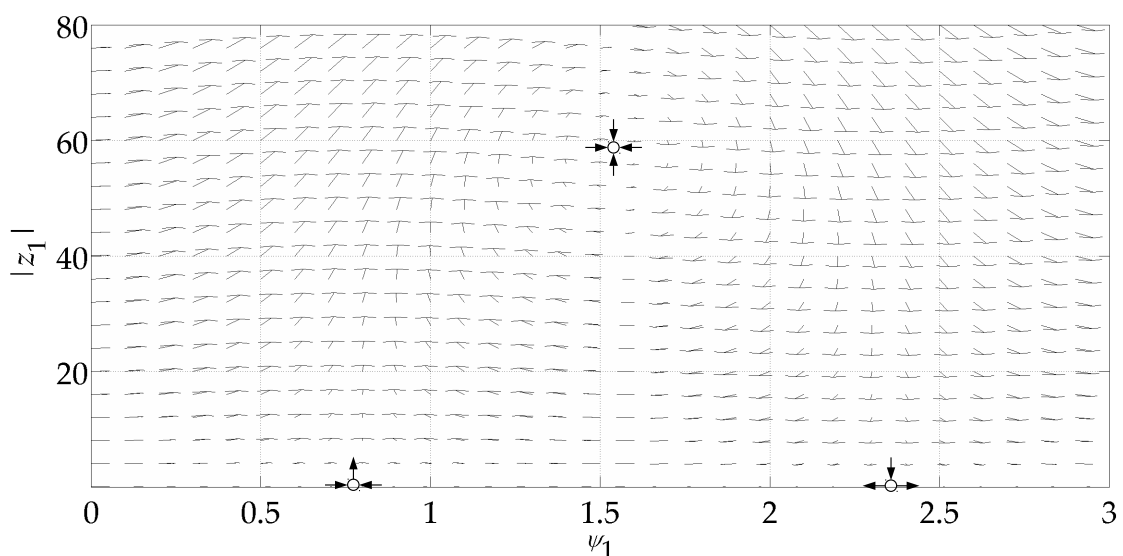


Figure 4.31: Poincaré map, first PR ($\Omega_0 = 2\omega_1$), ψ_1 - r_1 phase space, $\sigma = 0$. One stable attractor: $[1.54, 58.65]$. Two unstable attractors: $[0.79, 0]$ and $[2.36, 0]$.

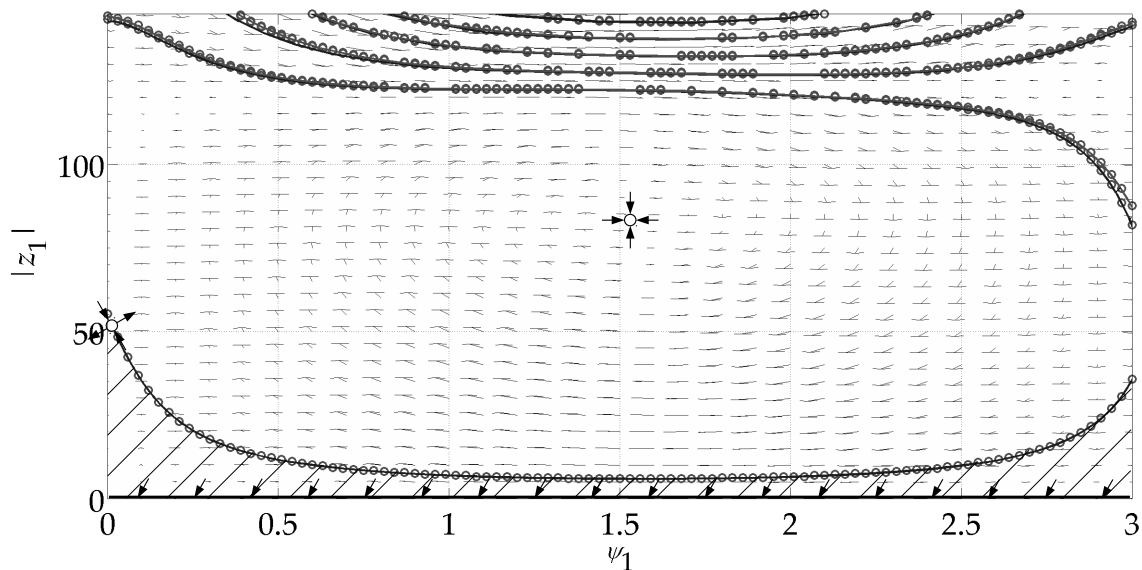


Figure 4.32: Poincaré map, first PR ($\Omega_0 = 2\omega_1$), ψ_1 - r_1 phase space, $\sigma = 0.4$. Two stable attractors: $[1.53, 83.98]$ and $[-, 0]$. One unstable attractor: $[0.01, 51.28]$. Hatched: basin of attraction of the trivial attractor. Limit of basins of attraction by numerical scanning (circles) and by backward time integration (line).

manner. Both amplitude and phase shift oscillate around the amplitude and the phase shift of the stable non-linear attractor until this state is reached.

Increasing σ leads to having two further attractors (see **Fig. 4.33**). Close to the amplitude of the first saddle point another one can be found lying on the border of the basin of attraction of the large amplitude node. This node is not displayed on the Poincaré map. The basin of attraction of the trivial attractor is larger than for smaller σ . However, the system is attracted by the large amplitude node starting from most states with amplitudes larger than the one of the second saddle point.

Larger values of σ will result in the basin of attraction of the low amplitude node becoming less important (see **Fig. 4.34**). The trivial attractor will attract the system from most states with amplitudes smaller than the amplitude of the second saddle point, while the second node will attract the system from most other states.

In analogy to the first PR, at the second PR within $[-\sigma_b; \sigma_b]$ only one stable attractor exists (see **Fig. 4.35**). The trivial solution is unstable resulting in two unstable attractors $[\frac{1}{4}\pi, 0]$ and $[\frac{3}{4}\pi, 0]$. The system is attracted by the non-trivial stable attractor from all states. Increasing σ beyond the second branch point stabilises the trivial solution (see **Fig. 4.36**). Having crossed the second branch point, the unstable part of the first loop is visible as a saddle point. Further increasing σ lets the basin of attraction of the trivial solution become more important (see **Fig. 4.37** to **Fig. 4.39**). Due to the stronger softening characteristic the maximum number of coexisting solutions is three for the second PR. Hence there is only one non-trivial stable attractor for all σ .

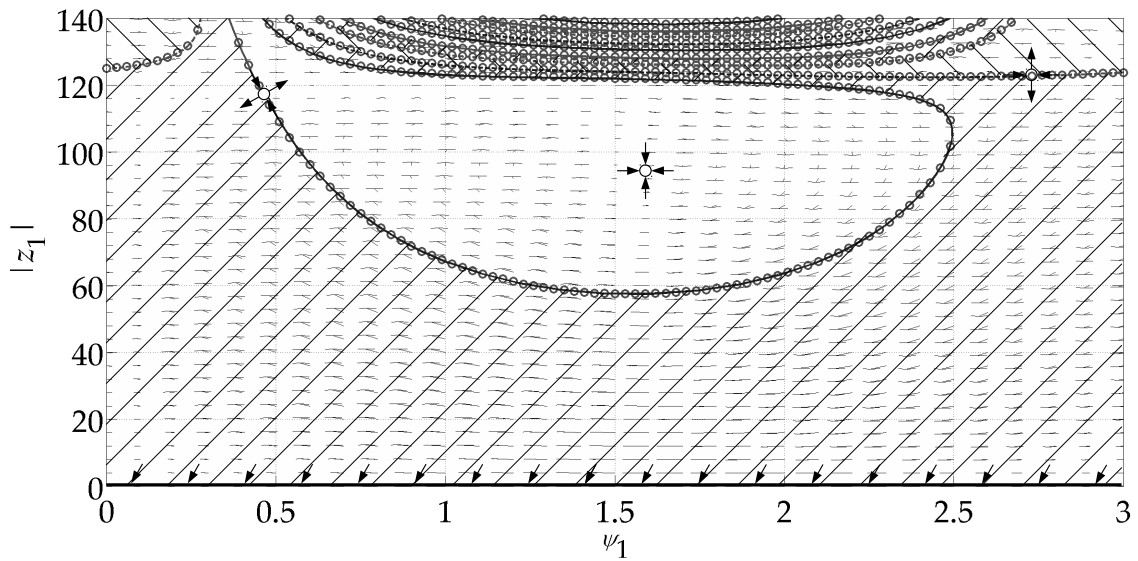


Figure 4.33: Poincaré map, first PR ($\Omega_0 = 2\omega_1$), ψ_1 - r_1 phase space, $\sigma = 0.6$. Two stable attractors: $[1.52, 94.28]$ and $[-, 0]$. Two unstable attractors (saddle points): $[0.44, 118.54]$ and $[2.73, 122.84]$. Hatched $+45^\circ$: basin of attraction of the trivial attractor. Hatched -45° : basin of attraction of the node $[3.13, 195.42]$. Limit of basins of attraction by numerical scanning (circles) and by backward time integration (line).

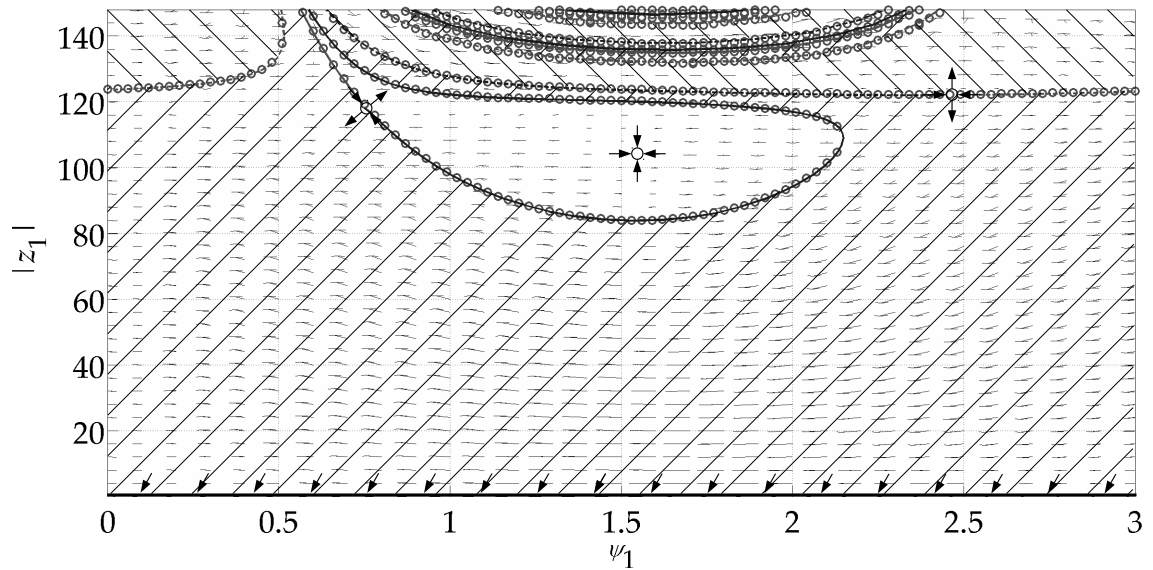


Figure 4.34: Poincaré map, first PR ($\Omega_0 = 2\omega_1$), ψ_1 - r_1 phase space, $\sigma = 0.8$. Two stable attractors: $[1.51, 103.67]$ and $[-, 0]$. Two unstable attractors (saddle points): $[0.73, 119.23]$ and $[2.44, 122.54]$. Hatched $+45^\circ$: basin of attraction of the trivial attractor. Hatched -45° : basin of attraction of the node $[3.14, 267.62]$. Limit of basins of attraction by numerical scanning (circles) and by backward time integration (line).

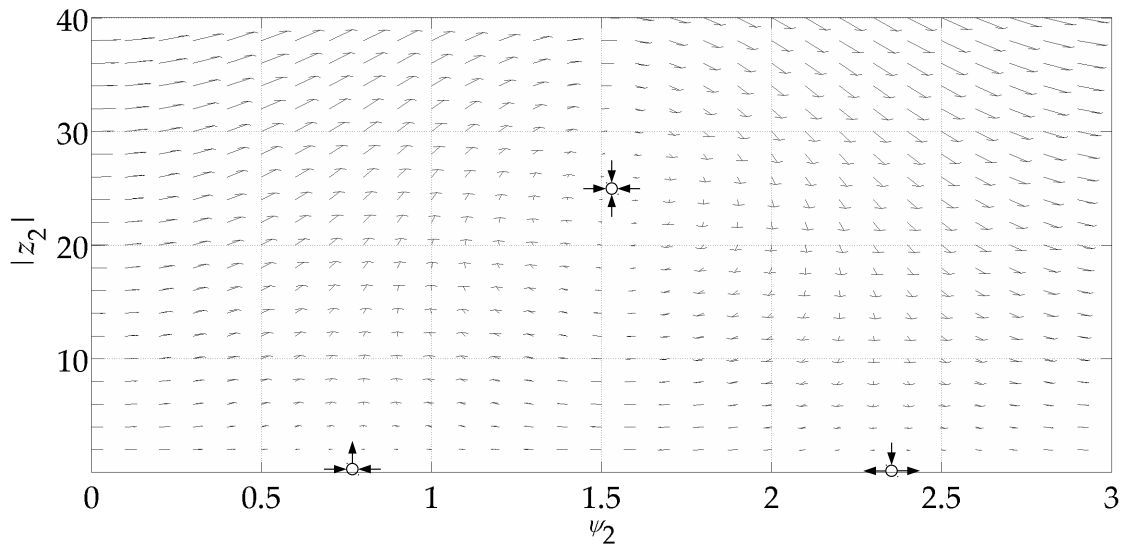


Figure 4.35: Poincaré map, second PR ($\Omega_0 = 2\omega_2$), ψ_2 - r_2 phase space, $\sigma = 0$. One stable attractor: $[1.53, 24.42]$. Two unstable attractors: $[\cdot 79, 0]$ and $[2.36, 0]$.

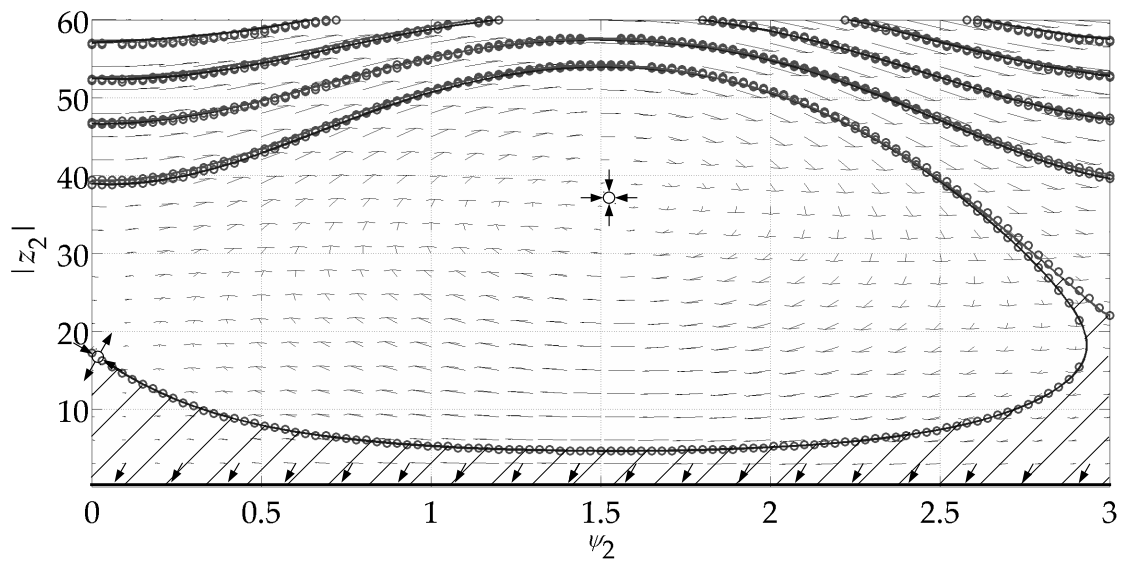


Figure 4.36: Poincaré map, second PR ($\Omega_0 = 2\omega_2$), ψ_2 - r_2 phase space, $\sigma = 0.5$. Two stable attractors: $[1.52, 36.88]$ and $[-, 0]$. One saddle point: $[0.04, 16.11]$. Hatched: basin of attraction of the trivial attractor. Limit of basins of attraction by numerical scanning (circles) and by backward time integration (line).

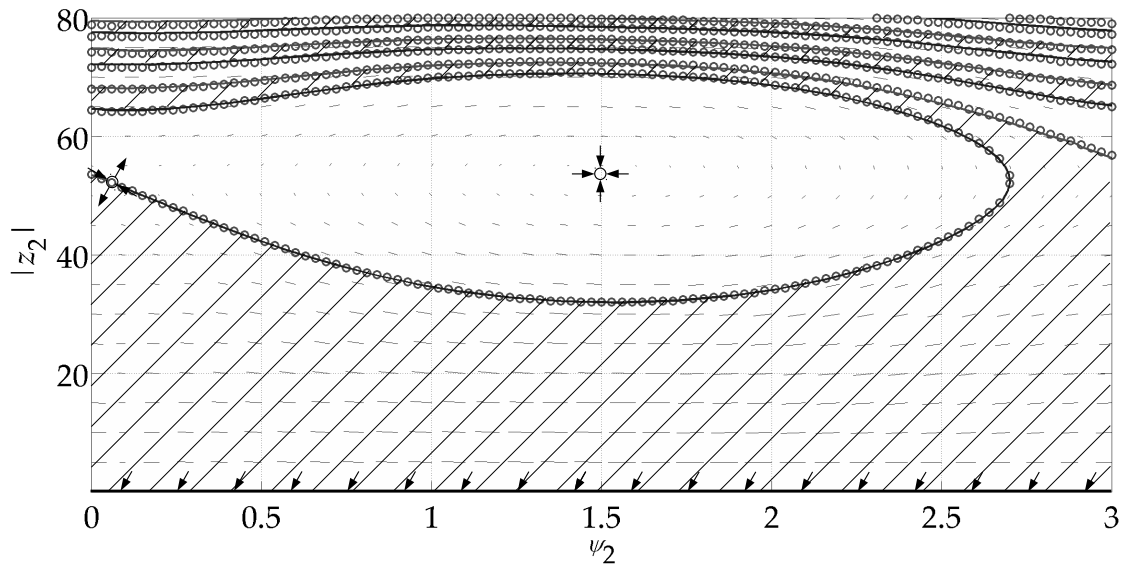


Figure 4.37: Poincaré map, second PR ($\Omega_0 = 2\omega_2$), ψ_2 - r_2 phase space, $\sigma = 1.5$. Two stable attractors: $[1.50, 54.02]$ and $[-, 0]$. One saddle point: $[0.06, 52.06]$. Hatched: basin of attraction of the trivial attractor. Limit of basins of attraction by numerical scanning (circles) and by backward time integration (line).

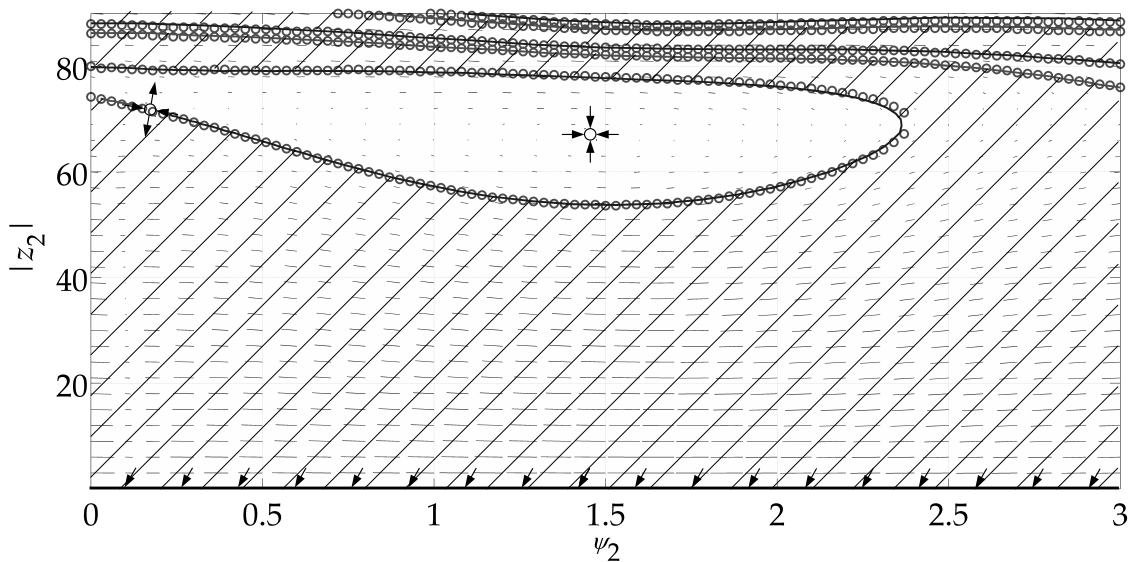


Figure 4.38: Poincaré map, second PR ($\Omega_0 = 2\omega_2$), ψ_2 - r_2 phase space, $\sigma = 2.5$. Two stable attractors: $[1.45, 67.24]$ and $[-, 0]$. One saddle point: $[0.16, 71.71]$. Hatched: basin of attraction of the trivial attractor. Limit of basins of attraction by numerical scanning (circles) and by backward time integration (line).

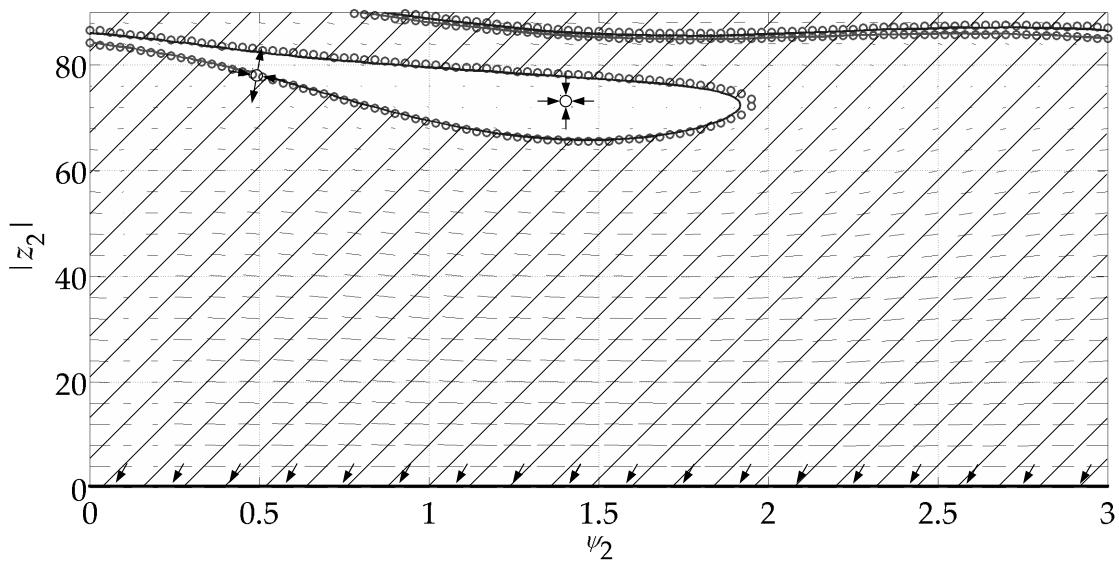


Figure 4.39: Poincaré map, second PR ($\Omega_0 = 2\omega_2$), ψ_2 - r_2 phase space, $\sigma = 3$. Two stable attractors: $[1.37, 73.20]$ and $[-, 0]$. One saddle point: $[0.48, 78.09]$. Hatched: basin of attraction of the trivial attractor. Limit of basins of attraction by numerical scanning (circles) and by backward time integration (line).

By analogy to Section 4.1.2, the reduced r_i - ψ_i phase spaces of the Poincaré maps are transformed to z_i - z'_i phase spaces according to Eqs. (4.2). This transformation doubles the node to a conjugate pair. The two saddle points of Fig. 4.31 shrink to one (see Fig. 4.40). Its manifold separates the basins of attraction of each of the conjugate nodes. The stable node doubles to a conjugate pair. The non-trivial attractors are closer to the trivial attractor in this transformation. The basin of attraction of the large amplitude node is better visible for larger values of σ . Hence the probability of each attractor to attract the system from random initial conditions becomes more clear in the z_i - z'_i phase spaces.

Increasing σ beyond the second branch point stabilises the trivial solution, which is a fixed point instead of a line in this phase space (see Fig. 4.41). The same as for the stable non-trivial solution, the unstable one also appears as a conjugate pair. Further increasing σ shows more fixed points, two conjugate pairs for the stable and the unstable states along the second loop (see Fig. 4.42 and Fig. 4.43). The almost symmetrical appearance about the horizontal axis is because all non-trivial attractors are visible as conjugate pairs and because the nodes have phase shifts close to $\pi/2$ and π . The dominance of the large amplitude nodes for large values of σ becomes apparent.

For the second PR, the Poincaré maps in the z'_2 - z_2 phase space look very similar to the ones of the first PR for small values of σ , except for smaller amplitudes of the node (see Fig. 4.44 and Fig. 4.45). For larger values of σ , the amplitude of the node increases, the phase shift decreases: the attractor moves away from the vertical axis. The basin of attraction of the trivial attractor increases. In contrast to the first PR, due to the more pronounced softening behaviour not more than five attractors appear (see Fig. 4.46 to Fig. 4.48).

No matter which phase space is investigated the difference between the scanning and the backward integration increases towards the final values of the backward integration, because errors in the integration build up. In the same manner as for the 1DOF system, states around the saddle point have higher modulation frequencies, the more σ is increased. To limit computation times the step size has not been decreased sufficiently to guarantee constant accuracy while increasing σ . The step size control was set to lower accuracy for larger values of σ . This causes the differences between the scanning and the backward integration methods to increase slightly for increasing σ .

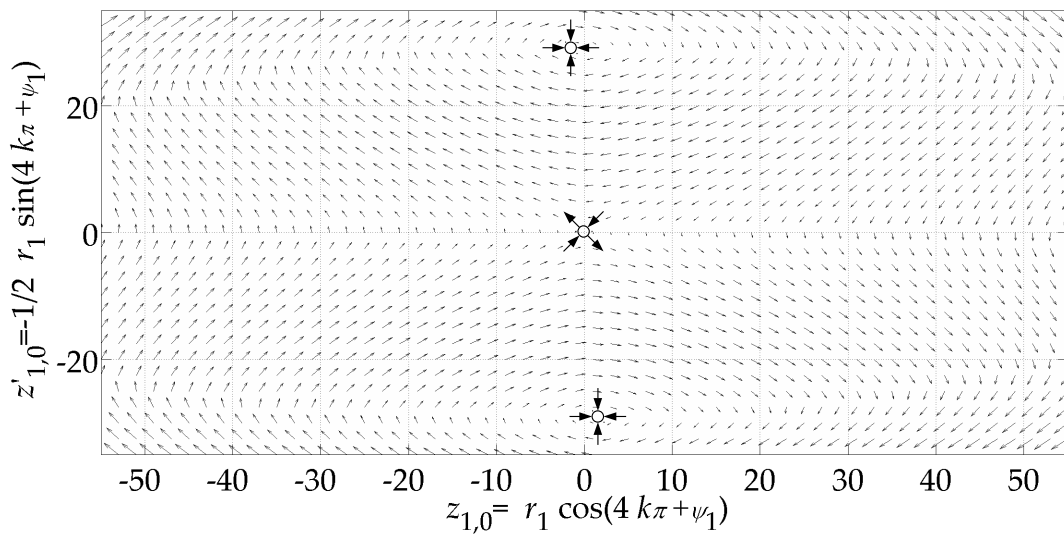


Figure 4.40: Poincaré map, first PR ($\Omega_0 = 2\omega_1$), z_1 - z'_1 phase space, $\sigma = 0$. Two nodes: $[\pm 1.81, \mp 29.31]$. One saddle point: $[0, 0]$.

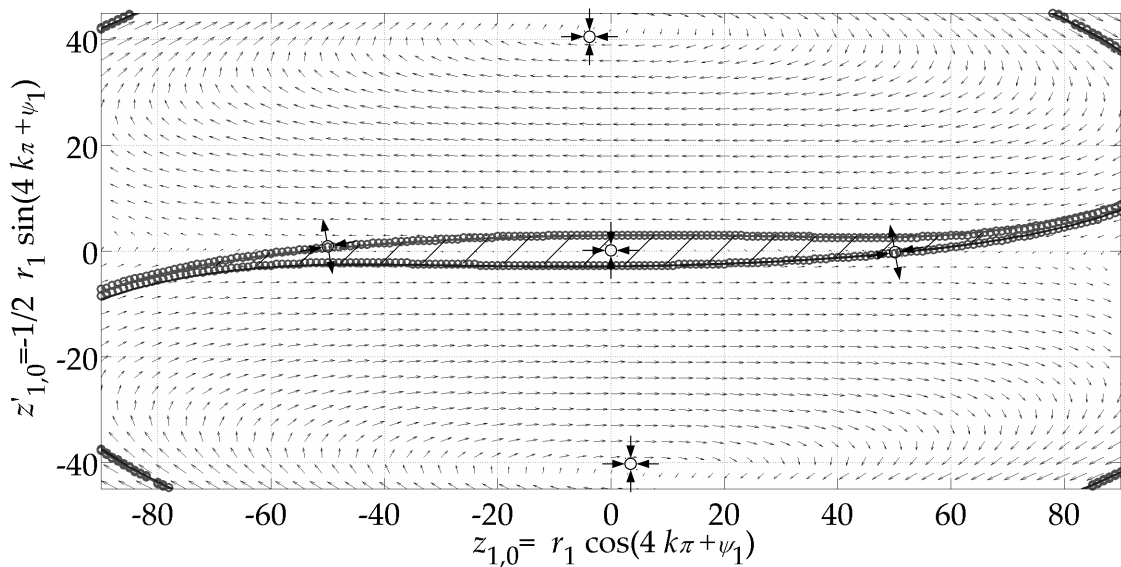


Figure 4.41: Poincaré map, first PR ($\Omega_0 = 2\omega_1$), z_1 - z'_1 phase space, $\sigma = 0.4$. Three stable attractors: $[0, 0]$ and $[\pm 3.43, \mp 41.96]$. Two unstable attractors: $[\pm 51.28, \mp 0.26]$. Hatched: basin of attraction of the trivial attractor. Limit of zones of attraction by numerical scanning (circles) and by backward time integration (line).

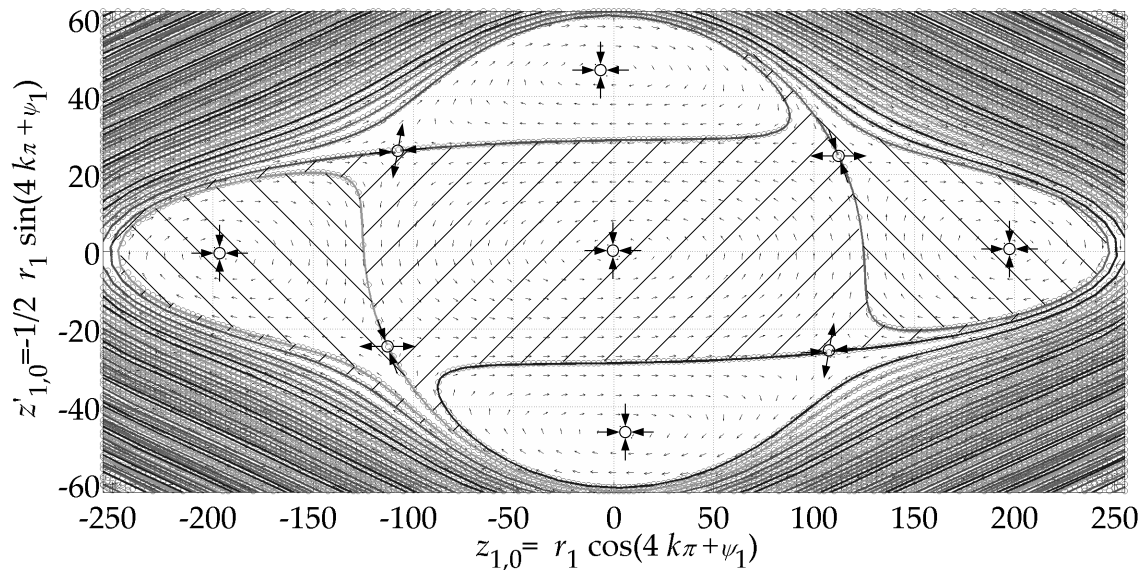


Figure 4.42: Poincaré map, first PR ($\Omega_0 = 2\omega_1$), z_1 - z'_1 phase space, $\sigma = 0.6$. Five nodes: $[0, 0]$, $[\pm 4.79, \mp 47.08]$, $[\pm 1.13, \mp 195.41]$. Four saddle points: $[\pm 107.25, \mp 25.25]$, $[\mp 112.58, \mp 24.57]$. Hatched $+45^\circ$: attracted by the trivial attractor. Hatched -45° : attracted by the node $[\mp 195.41, \mp 1.13]$.

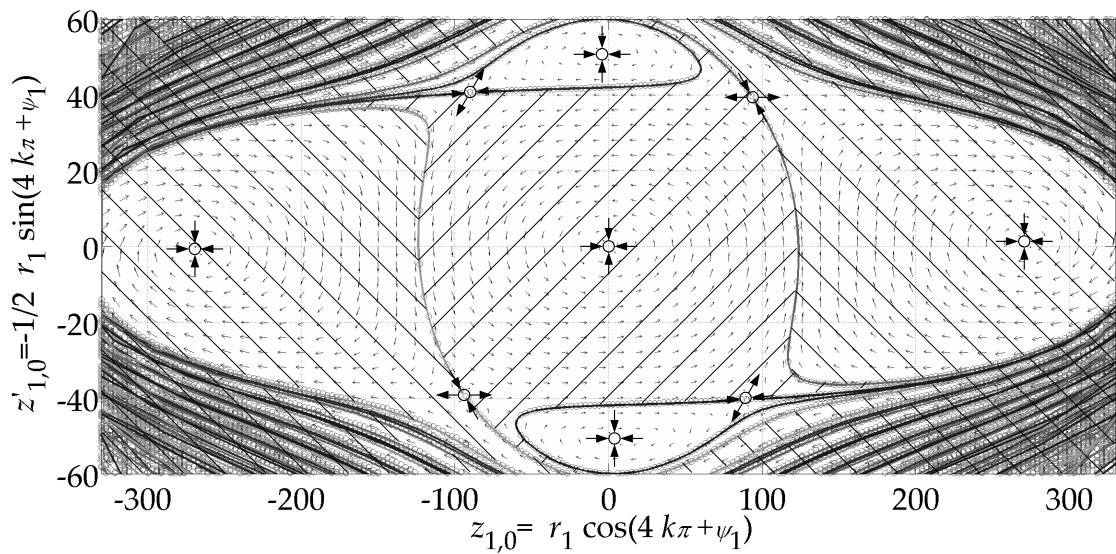


Figure 4.43: Poincaré map, first PR ($\Omega_0 = 2\omega_1$), z_1 - z'_1 phase space, $\sigma = 0.8$. Five nodes: $[0, 0]$, $[\pm 6.30, \mp 51.74]$, $[\pm 0.21, \mp 267.62]$. Four saddle points: $[\pm 88.85, \mp 39.76]$, $[\mp 93.60, \mp 39.55]$. Hatched $+45^\circ$: attracted by the trivial attractor. Hatched -45° : attracted by the node $[\mp 267.62, \mp 0.21]$.

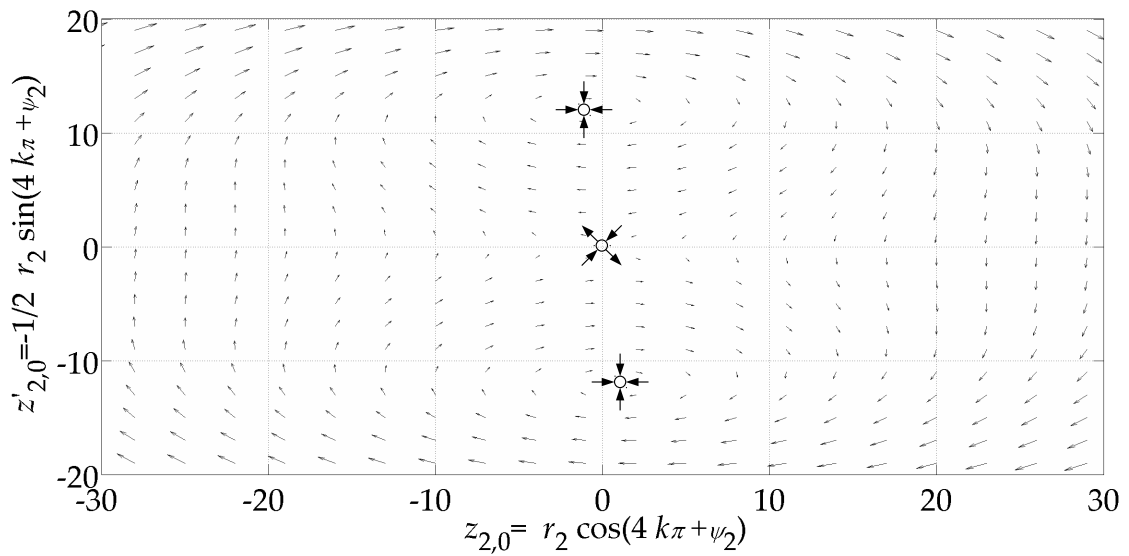


Figure 4.44: Poincaré map, second PR ($\Omega_0 = 2\omega_2$), z_2 - z'_2 phase space, $\sigma = 0$. Two nodes: $[\pm 1.00, \mp 12.20]$. One saddle point: $[0, 0]$.

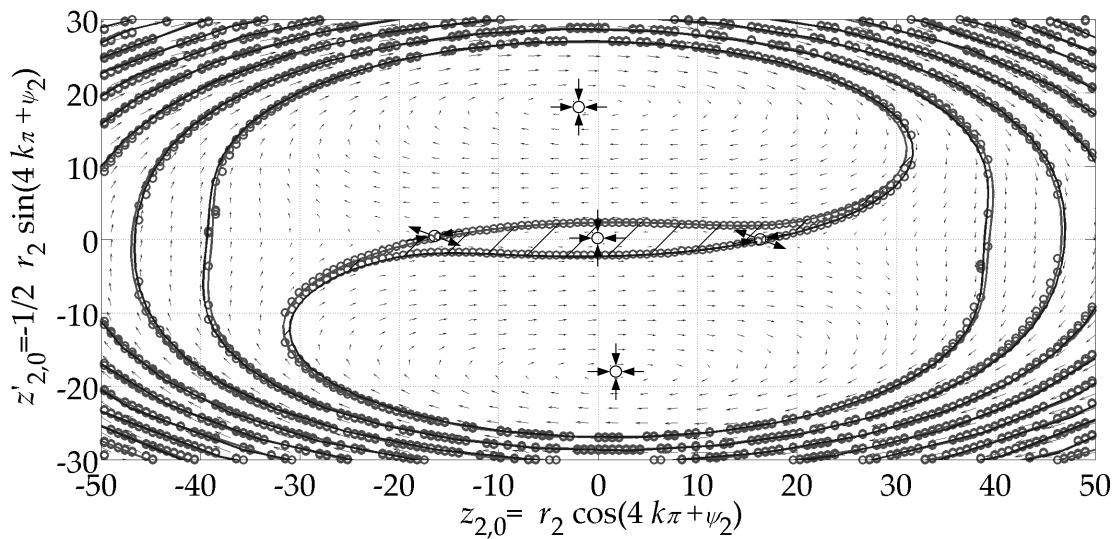


Figure 4.45: Poincaré map, second PR ($\Omega_0 = 2\omega_2$), z_2 - z'_2 phase space, $\sigma = 0.5$. Three nodes: $[0, 0]$ and $[\pm 1.87, \mp 18.42]$. Two saddle points: $[\pm 16.01, \mp 0.32]$. Hatched: basin of attraction of the trivial attractor. Limit of zones of attraction by numerical scanning (circles) and by backward time integration (line).

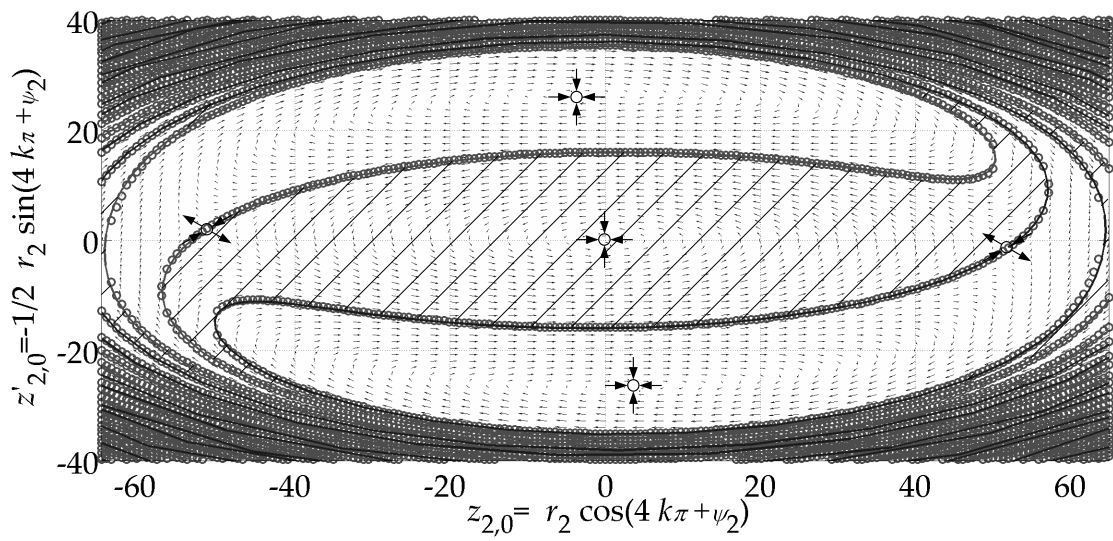


Figure 4.46: Poincaré map, second PR ($\Omega_0 = 2\omega_2$), z_2 - z'_2 phase space, $\sigma = 1.5$. Three stable attractors (nodes): $[0, 0]$ and $[\pm 3.82, \mp 26.94]$. Two unstable attractors (saddle points): $[\pm 51.97, \mp 1.56]$. Hatched: basin of attraction of the trivial attractor.

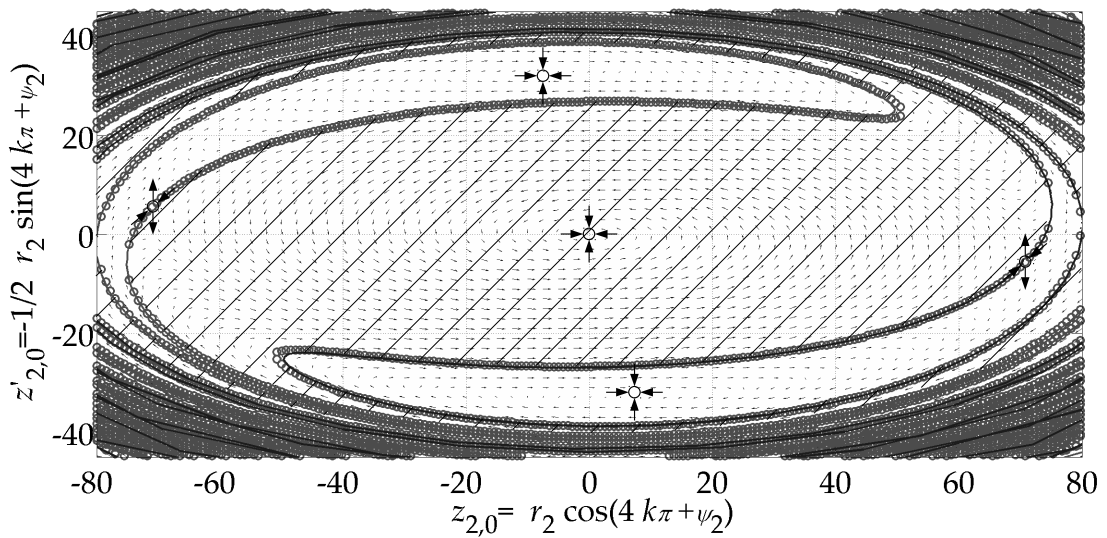


Figure 4.47: Poincaré map, second PR ($\Omega_0 = 2\omega_2$), z_2 - z'_2 phase space, $\sigma = 2.5$. Three stable attractors (nodes): $[0, 0]$ and $[\pm 8.10, \mp 33.38]$. Two unstable attractors (saddle points): $[\pm 70.79, \mp 5.71]$. Hatched: basin of attraction of the trivial attractor.

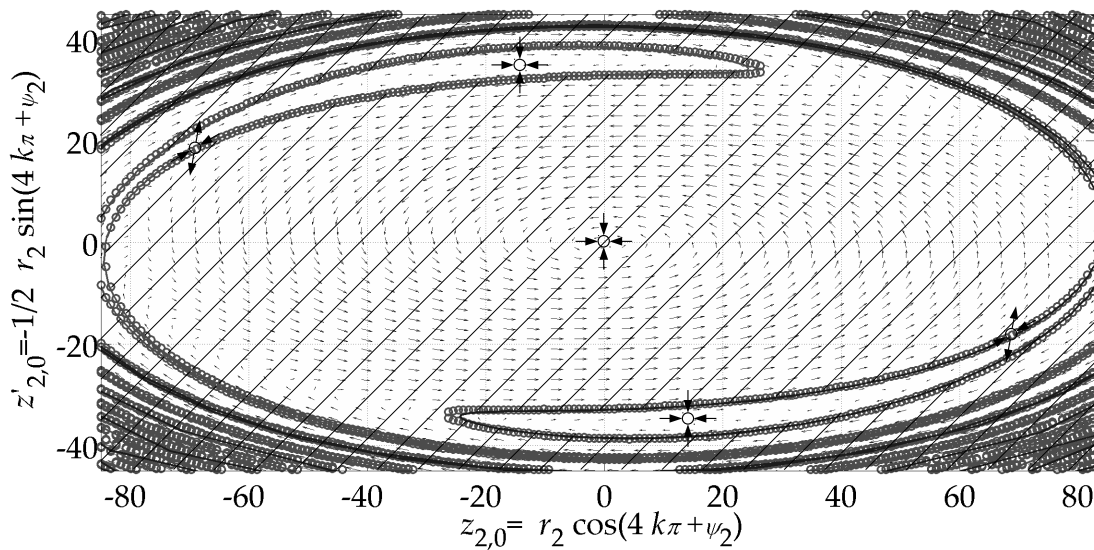


Figure 4.48: Poincaré map, second PR ($\Omega_0 = 2\omega_2$), z_2 - z_2' phase space, $\sigma = 3$. Three nodes: $[0, 0]$ and $[\pm 14.60, \mp 35.86]$. Two saddle points: $[\pm 69.27, \mp 18.03]$. Hatched: basin of attraction of the trivial attractor. Limit of zones of attraction by numerical scanning (circles) and by backward time integration (line).

As explained in Section 4.1.2, by scanning not only the phase space but also the parameter space within a certain range of σ , the lowest border of the basin of attraction of the trivial solution can be displayed (see Fig. 4.49 and Fig. 4.50). These plots are a good qualitative measure of how powerful the trivial solution is in attracting the system. For a quantitative comparison the measure $P = \frac{r_{\text{border}}}{|z|} \Big|_{\sigma=2\sigma_b}$ introduced in Section 4.1.2 is employed. For the first PR it takes on the value $P = 0.77$, while for the second PR it takes on the value $P = 0.32$. Hence, in relative numbers, the basin of attraction of the trivial attractor grows faster when increasing σ at the first than at the second PR. For PE frequencies larger than the second branch point, the system is more likely to be attracted by non-trivial states for the second PR than for the first PR when the initial conditions are a slight perturbation from the trivial stable state.

In this chapter 1DOF and 2DOF PE non-linear systems introduced in Section 3.1.1 and Section 3.2.1 were investigated numerically. The results of time simulations and numerical path following of limit cycles at PR were compared to analytical and semi-analytical approximations in Section 3.1.3. The quasi-modally reduced model derived in Section 3.2.4 was proven to be highly accurate within the PR. Basins of attractions of the computed stable states were analysed and their relevance was discussed.

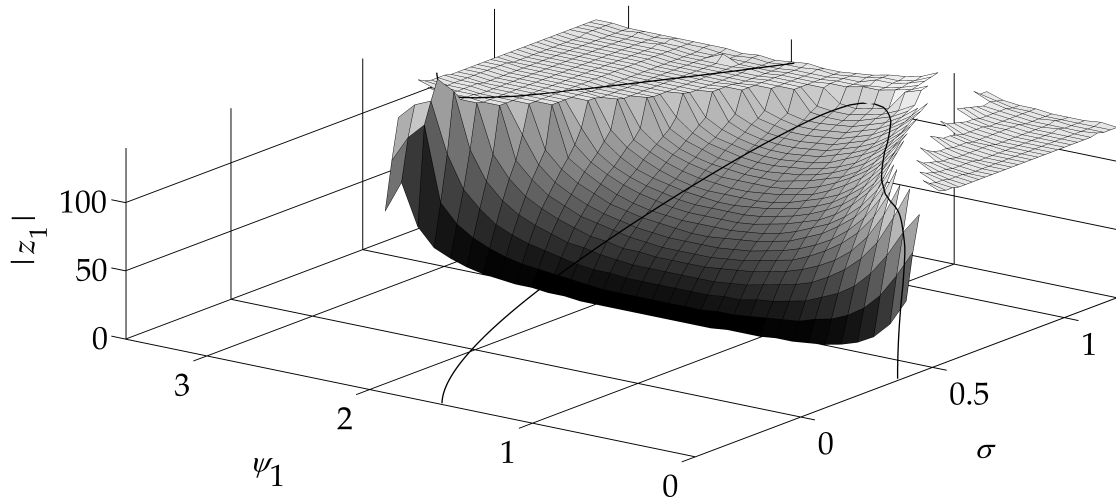


Figure 4.49: Lowest border (surface grid) between the basins of attraction of the non-trivial stable steady states (line) and the trivial stable steady states ($[>0.387,-,0]$ plane) in the σ - ψ_1 - z_1 parameter-phase-space. First PR ($\Omega_0 = 2\omega_1$).

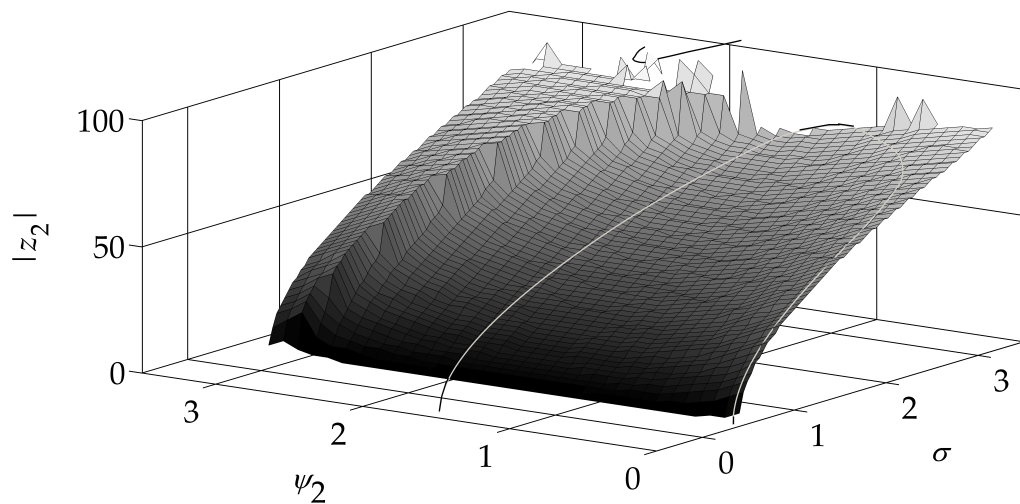


Figure 4.50: Lowest border (surface grid) between the basins of attraction of the non-trivial stable steady states (line) and the trivial stable steady states ($[>0.396,-,0]$ plane) in the σ - ψ_2 - z_2 parameter-phase-space. Second PR ($\Omega_0 = 2\omega_2$).

5 Manipulating the Characteristics of a One and a Two Degree of Freedom Parametrically Excited Non-Linear System

In the previous chapters 1DOF and 2DOF PE non-linear systems were introduced and studied. Analytical results were validated with numerical methods employing a parameter set stated in **Tab. 3.2**. The parameters' values led to certain characteristics of the bifurcated limit cycles at PR. This chapter deals with tuning these parameters in order to fulfil possible requirements such as desired shape of the amplitude characteristics, maximum amplitude at PR and phase shifts of the stable limit cycles at PR. First the 1DOF system is investigated in Section 5.1 and the results are then applied to the 2DOF system in Section 5.2. This procedure is not straightforward since the bifurcation's characteristics depend in a complicated and non-linear manner on the parameter values.

Within the scope of analytical analyses for the 1DOF system—especially in the case of non-steady PE—the chapter follows study results by RHOADS ET AL. [7, 25]. Subsequently, applying these results to the 2DOF system is addressed.

Finally the basins of attraction of analytically, semi-analytically and numerically detected attractors are discussed for a manipulated 1DOF and for a manipulated 2DOF system.

5.1 Manipulating the Characteristics of the 1DOF System

In Section 5.1.1 the parameters of the 1DOF system introduced in Section 3.1 are tuned to fulfil desired features of the characteristics of the bifurcated limit cycles. For this results from Section 3.1.3 can be employed. In Section 5.1.2 a non-steady PE is introduced. Thereby, the PE magnitude may increase or decrease slowly compared to the PE frequency. This behaviour is introduced to cover systems where the PE magnitude can not be controlled by the system's design but is an external input for the system. Problems arise because the width of the PR, the centre of the PR, the hardening/softening-behaviour of the amplitude characteristics and hence the phase shift of the stable limit cycles all may depend on the PE magnitude. The interdependencies of the parameters is investigated and possible strategies to handle the above difficulties are presented.

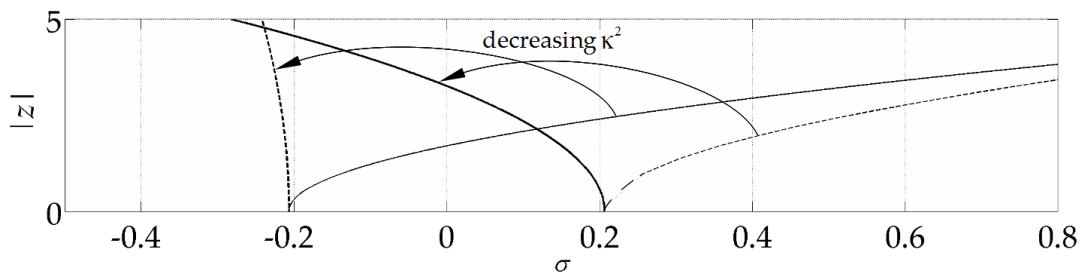


Figure 5.1: By manipulating the non-linearity parameter κ^2 , the limit cycles' characteristics can be changed qualitatively. Solid: stable limit cycles; hatched: unstable limit cycles.

5.1.1 Steady Parametric Excitation

In Section 3.1 it was shown that the qualitative behaviour of the bifurcated limit cycles at PR only depends on the non-linearity parameter κ^2 . Indeed, the maximum amplitude of the bifurcated limit cycles is not determined only by κ^2 , but by different parameters as well, as is the bandwidth of the PR. However, the value of κ^2 determines whether the branches have hardening or softening characteristics (see **Fig. 5.1**: decreasing κ^2 changes the hardening/softening characteristics and the stability of the limit cycles associated with each branch of the curve). Hence κ^2 also defines whether the stable non-trivial solution has a phase shift ψ close to 0 or close to $\pi/2$.

In Section 3.1 and Section 4.1 a parameter set is discussed for which the two bifurcated limit cycles both have hardening characteristics. This means that the stable, non-trivial solution at PR has a phase shift $\psi \approx \pi/2$. For certain applications it might be desirable to eliminate this phase shift. Furthermore, increasing the amplitude of the stable non-trivial solution at PR might be necessary. Below is demonstrated how to define κ^2 for a maximum amplitude if the phase shift ψ has to be close to zero and all other parameters remain as stated in **Tab. 3.2**.

As deduced in Section 3.1, κ^2 has to take on the value $\kappa^2 = - \left| \frac{4\epsilon_{\text{non}}\omega_0^2}{3(\epsilon_{\text{lin}} + 2\omega_0^2)} \right| = -3.46 \cdot 10^{-3}$ to fulfil the task outlined above. However, the value $\kappa^2 = -4 \cdot 10^{-3}$ is chosen to guarantee a softening characteristic of both branches even with small numerical differences between actual and design values. Note that the value of κ^2 can be varied by modifying $k_{\text{b,non}}$ and $k_{\text{PE,non}}$. However, varying $k_{\text{PE,non}}$ will change the value of ϵ_{non} , the value of a parameter which was used to determine the value of κ^2 . Hence, with the conditional equations used here, κ^2 has to be tuned by setting $k_{\text{b,non}}$ appropriately.

With the modified parameter set the system shows a behaviour as presented in **Fig. 5.2**. Within the PR ($\sigma = [-0.2066; 0.2066]$) the analytical, the semi-analytical and the numerical solutions agree well. For the range of σ studied here, the semi-analytical and the numerical solutions are in good agreement even for values of σ outside of the PR. The maximum amplitude at PR is $r = |z| = 4.6$, which is 1.92 times higher than for the parameter set in Section 4.1.

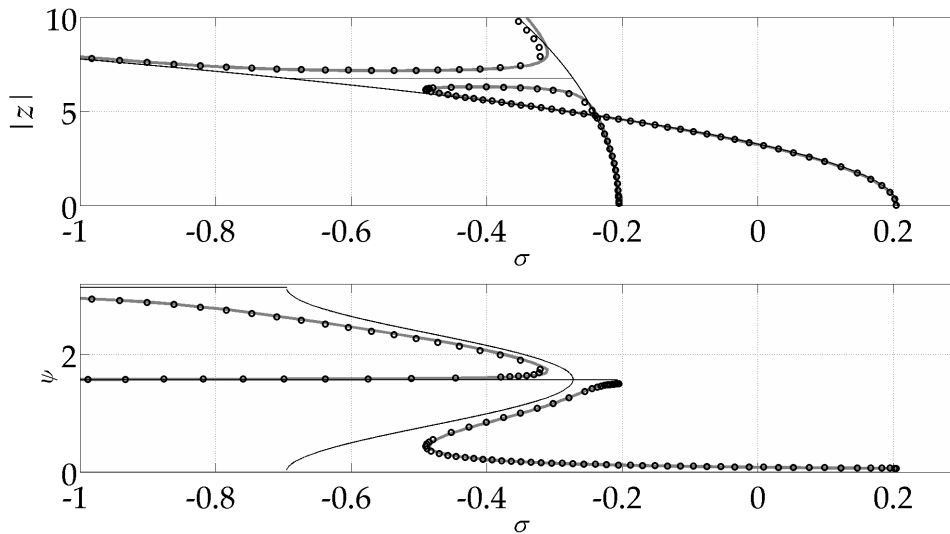


Figure 5.2: Limit cycles of Eqs. (3.15), Eqs. (4.1) for $\kappa^2 = -4 \cdot 10^{-3}$. Thin, black: analytical solution; bold, grey: semi-analytical solution; circles: numerical solution.

Comparing the Poincaré maps for $\sigma = -0.3$ and $\sigma = -0.4$ (see **Fig. 5.3-Fig. 5.6**) to the ones in Section 4.1 it becomes clear that the stability of the branches and their phase shifts have changed: the node has a very small phase shift only—the saddle has a phase shift close to $\pi/2$. This also means that for large values of r the system is attracted by decreasing values of ψ . Only for values of r close to the trivial attractor the system is attracted by increasing values of ψ . The direction of rotation in the phase space has changed globally. Where it is clockwise for the original system it is anti-clockwise for the system presented here and vice versa.

Studying the behaviour at $\sigma = -0.3$ (see **Fig. 5.3**), except for the trivial attractor, only two attractors can be identified: the node at $r = 5.12$, $\psi = 0.15$ and the saddle at $r = 6.13$, $\psi = 1.16$. It becomes clear that by approaching the case $\kappa^2 = -3.46 \cdot 10^{-3}$, the bifurcation point $\sigma_{b,2}$ of \bar{r}_c and \bar{r}_d lies close to $-\sigma_b$. The basin of attraction of the second node already looms in the centre of **Fig. 5.3** due to the large slopes of the amplitude characteristics: the border of the basin of attraction between the node and the trivial attractor has a local maximum in terms of r for $\psi = 1.61$. Diverging from the PR as much as $\sigma = -0.4$ the first non-trivial attractors both increase slightly in terms of r and move towards each other in terms of ψ (see **Fig. 5.4**). The two additional attractors, which could already be anticipated in **Fig. 5.3**, become visible: the node at $r = 12.21$, $\psi = 1.61$ and the saddle at $r = 7.25$, $\psi = 2.08$. Compared to $\sigma = -0.3$ the basin of attraction of the trivial attractor has increased, that of the first node has decreased.

By analogy to Section 4.1.2, the reduced ψ - r phase space of the Poincaré maps is transformed to the z - z' phase space according to Eqs. (4.2). This transformation means that each node and saddle of **Fig. 5.3** and **Fig. 5.4** appears as a conjugate pair. The trivial attractor also shrinks to a node. Hence, at $\sigma = -0.3$ in **Fig. 5.5** three nodes are visible: $[\pm 5.06, \mp 0.38]$ and $[0, 0]$.

Decreasing σ to $\sigma = -0.4$ in **Fig. 5.6** two more nodes can be identified, which lie on the second loop. The basin of attraction of the trivial attractor has extended compared to $\sigma = -0.3$. The basin of attraction of the first non-trivial attractor has diminished.

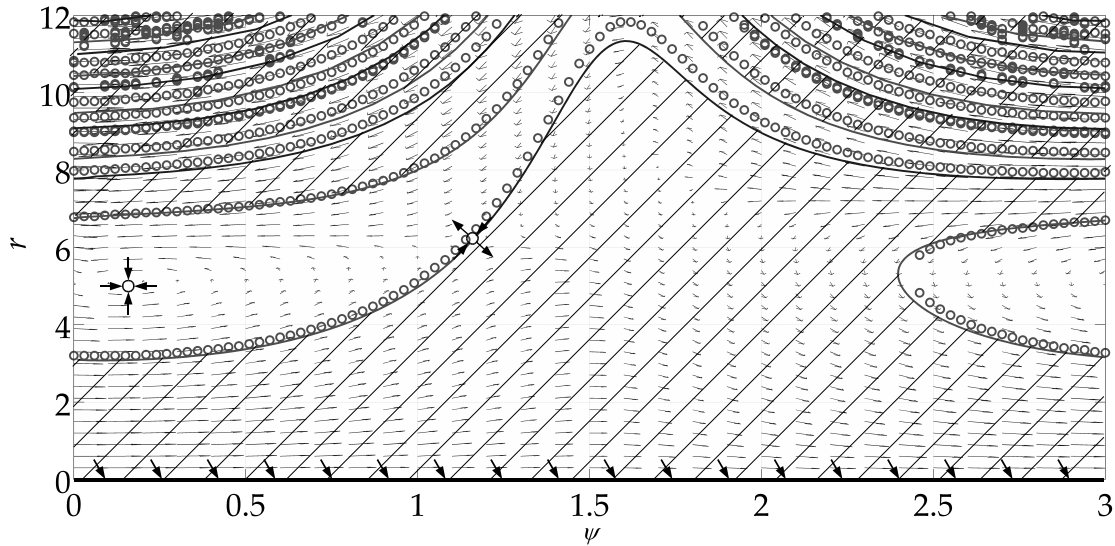


Figure 5.3: Poincaré map, ψ - r phase space, $\sigma = -0.3$. Two stable attractors: $[0.15, 5.12]$ and $[-, 0]$. One unstable attractor (saddle point): $[1.16, 6.13]$. Hatched: basin of attraction of the trivial attractor. Limit of basins of attraction by numerical scanning (circles) and by backward time integration (line).

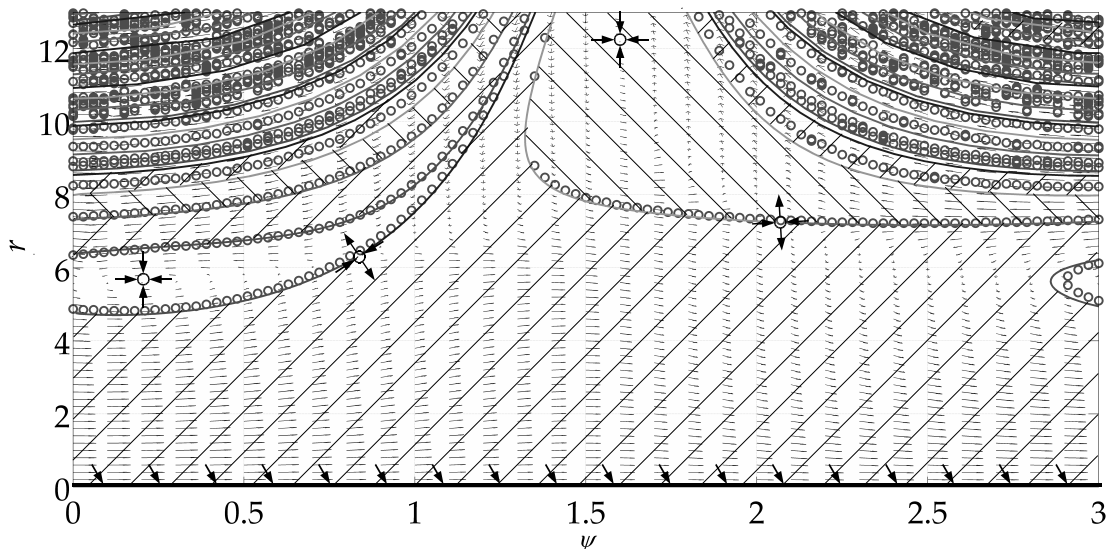


Figure 5.4: Poincaré map, ψ - r phase space, $\sigma = -0.4$. Three stable attractors: $[0.21, 5.61]$, $[1.61, 12.21]$ and $[-, 0]$. Two unstable attractors (saddle points): $[0.84, 6.30]$ and $[2.08, 7.25]$. Hatched $+45^\circ$: attracted by the trivial attractor. Hatched -45° : attracted by the node $[1.61, 12.21]$.

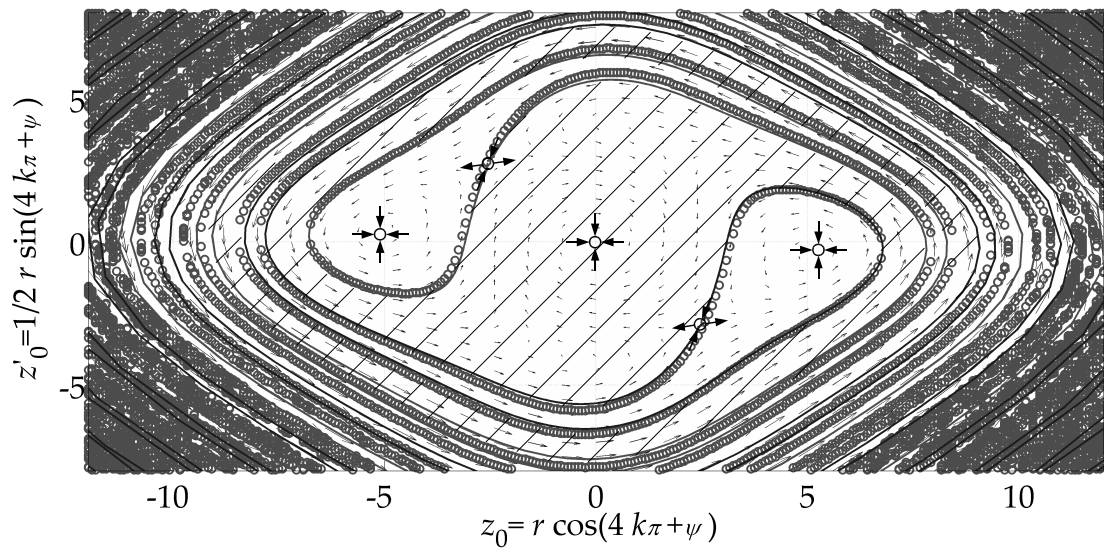


Figure 5.5: Poincaré map, z - z' phase space, $\sigma = -0.3$. Three nodes: $[\pm 5.06, \mp 0.38]$ and $[0, 0]$. Two saddle points: $[\pm 2.39, \mp 2.81]$. Hatched: basin of attraction of the trivial attractor. Limit of basins of attraction by numerical scanning (circles) and by backward time integration (line).

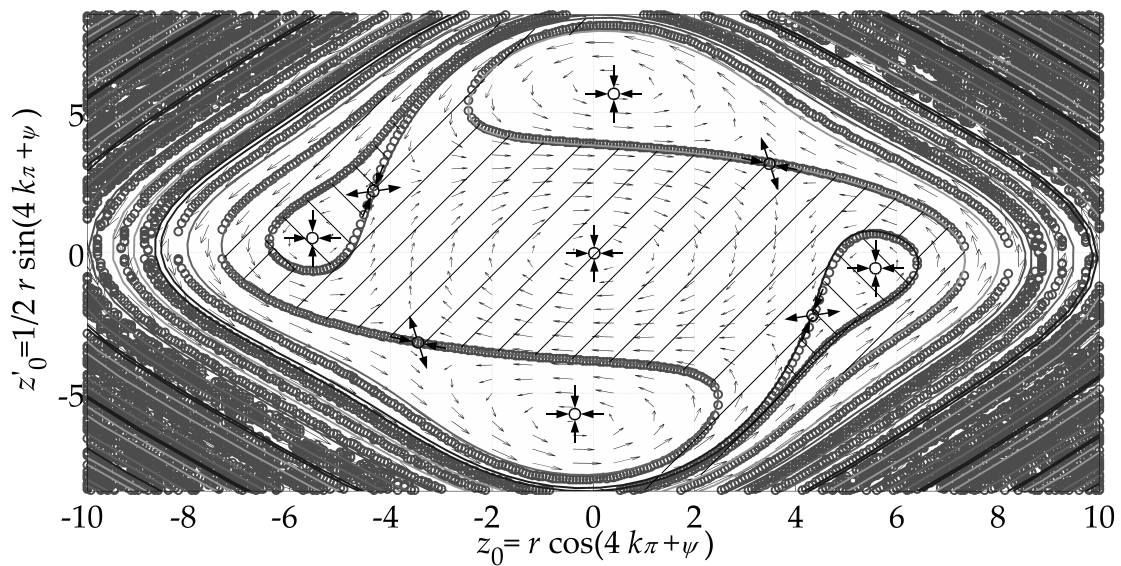


Figure 5.6: Poincaré map, z - z' phase space, $\sigma = -0.4$. Five nodes: $[\pm 5.49, \mp 0.61]$, $[\pm 0.44, \mp 5.66]$ and $[0, 0]$. Four saddle points: $[\pm 4.17, \mp 2.36]$ and $[\pm 0.28, \mp 3.63]$. Hatched $+45^\circ$: basin of attraction of the trivial attractor. Hatched $+45^\circ$: basin of attraction of the first non-trivial attractor. Limits of basins of attraction by numerical scanning (circles) and by backward time integration (line).

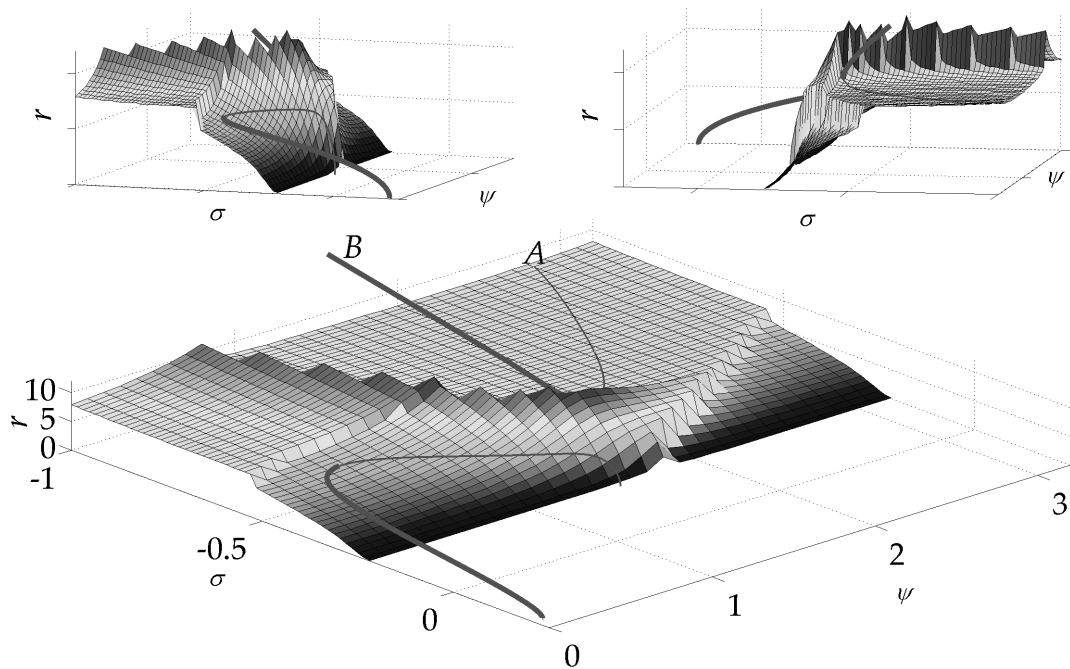


Figure 5.7: Lowest border (surface grid) between the basins of attraction of the bifurcated limit cycle (line) and stable trivial solutions (rest position) ($[\leq -0.207, -, 0]$ plane) in the σ - ψ - r phase parameter space.

Plotting the bifurcated branches in a three-dimensional σ - ψ - z phase parameter space (see **Fig. 5.7**) provides a better understanding of the interdependencies of z and ψ . Displaying the lowest border (surface grid) between the basins of attraction of the bifurcated limit cycle (line) and the stable trivial solutions (rest position) in the $[\leq -0.207, -, 0]$ -plane demonstrates the power of each attractor to attract the system.

Stable states along the bifurcated branches are indicated as bold lines. The unstable states (thin lines) along the branches are a subset of the border between the basins of attraction and are part of the surface displayed here. The second loop enters/leaves the displayed part of the phase parameter space at $A = [-1, 2.97, 7.91]$ and $B = [-1, \pi/2, 23.82]$.

The measure $P = \frac{r_{\text{border}}}{|z|} \Big|_{\sigma=2\sigma_b}$ introduced in Section 4.1.2 quantifies this behaviour. Here it takes on the value of $P = 0.87$ which means an increase by 211% compared to the value achieved with $\kappa^2 = 2.403 \cdot 10^{-2}$. Straightening the branches makes them diverge faster from the trivial attractor and reduces the risk of the system being attracted by a non-trivial attractor starting with a small but non-zero amplitude.

5.1.2 Non-steady Parametric Excitation

In the previous chapters the PE parameters ε_{lin} and $\varepsilon_{\text{nonlin}}$ have been treated as fixed and chosen by design considerations. However, for some applications ε_{lin} and $\varepsilon_{\text{nonlin}}$ might not be fixed but depend on operational circumstances. As a result the qualitative characteristics of the system at PRs are defined not only by the non-linearity of the stiffness but also by the PE parameters. This influence of the PE parameters ε_{lin} and $\varepsilon_{\text{nonlin}}$ is discussed in this section. Furthermore, it is demonstrated how the manipulation scheme has to be modified to tune or optimize the system's behaviour at PR.

Recalling the relation between the non-dimensional and physical parameters reveals that κ^2 depends on the non-linear stiffness and the non-linear PE stiffness constants, while ε_{lin} and $\varepsilon_{\text{nonlin}}$ depend on the PE stiffness constants.

Assuming that the PE parameters ε_{lin} and $\varepsilon_{\text{nonlin}}$ both result from the same physical effect which affects both in the same manner, both PE parameters can be renamed as

$$\varepsilon_{\text{lin}} = \varepsilon_{\text{PE}}, \quad \varepsilon_{\text{nonlin}} = C_{\text{nonlin}}\varepsilon_{\text{PE}}, \quad C_{\text{nonlin}} = \frac{\varepsilon_{\text{nonlin}}}{\varepsilon_{\text{lin}}}. \quad (5.1)$$

The non-linearity parameter κ^2 was introduced as

$$\kappa^2 = \frac{(k_{\text{b,nonlin}} + k_{\text{PE,nonlin}})x^{*2}}{m\Omega^{*2}} \quad (5.2)$$

and can be written with Eq. (5.1) as

$$\kappa^2 = \kappa_{\text{b}}^2 + C_{\text{nonlin}}\varepsilon_{\text{PE}}, \quad \kappa_{\text{b}}^2 = \frac{k_{\text{b,nonlin}}x^{*2}}{m\Omega^{*2}}. \quad (5.3)$$

If the magnitude ε_{PE} of the PE changes, then the amplitude characteristics \bar{r}_{b} and \bar{r}_{c} change too (see **Fig. 5.8**), becoming

$$\bar{r}_{\text{b}}(\varepsilon_{\text{PE}}) = \pm \sqrt{\frac{4\omega_0\varepsilon\sigma + 2\varepsilon_{\text{PE}}}{-2C_{\text{nonlin}}\varepsilon_{\text{PE}} + 3(\kappa_{\text{b}}^2 + C_{\text{nonlin}}\varepsilon_{\text{PE}})(1 - \frac{\varepsilon\sigma}{\omega_0})}}, \quad (5.4a)$$

$$\bar{r}_{\text{c}}(\varepsilon_{\text{PE}}) = \pm \sqrt{\frac{4\omega_0\varepsilon\sigma - 2\varepsilon_{\text{PE}}}{2C_{\text{nonlin}}\varepsilon_{\text{PE}} + 3(\kappa_{\text{b}}^2 + C_{\text{nonlin}}\varepsilon_{\text{PE}})(1 - \frac{\varepsilon\sigma}{\omega_0})}}. \quad (5.4b)$$

As can be seen in **Fig. 5.8**, the width of the PR also depends on ε_{PE} . Only the left branch is depicted in **Fig. 5.8**, but the bifurcation points $\sigma = \mp\sigma_{\text{b}}$ are symmetric regarding the angular centre frequency Ω_0 ($\sigma = 0$), so that

$$\sigma = \mp\sigma_{\text{b}}(\varepsilon_{\text{PE}}) = \mp\frac{\varepsilon_{\text{PE}}}{2\varepsilon\omega_0} \quad (5.5)$$

with the natural angular frequency

$$\omega_0 = \sqrt{\omega_{\text{b}}^2 + \varepsilon_{\text{PE}}}, \quad \omega_{\text{b}}^2 = \frac{k_{\text{b,lin}}}{m\Omega^{*2}} \quad (5.6)$$

also depending on ε_{PE} . For a small PE $\varepsilon_{\text{PE}} \ll 1$, so that

$$\omega_{\text{b}} \gg \varepsilon_{\text{PE}} \Rightarrow \sigma_{\text{b}} \approx \frac{\varepsilon_{\text{PE}}}{\text{const.}} \propto \varepsilon_{\text{PE}}. \quad (5.7)$$

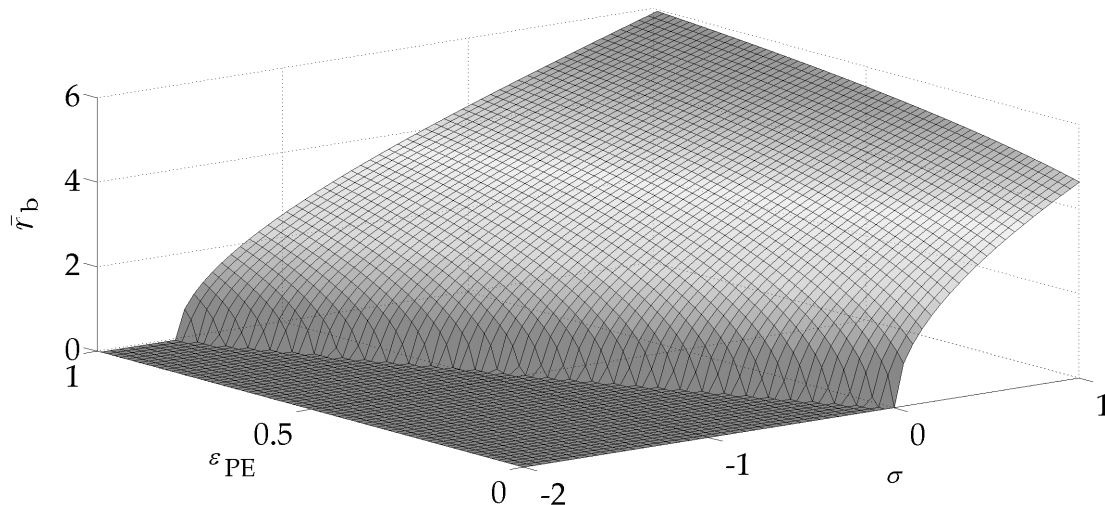


Figure 5.8: Amplitude characteristic $\bar{r}_b(\sigma, \varepsilon_{PE})$ of the bifurcated limit cycle with parameters from **Tab. 3.2** (except for $\varepsilon_{lin}, \varepsilon_{nlin}$). The width of the PR increases almost proportionally to ε_{PE} for small ε_{PE} .

As a result of $\omega_0(\varepsilon_{PE})$, the angular centre frequency Ω_0 of the PR also depends on ε_{PE} as

$$\Omega_0 = \Omega_0(\varepsilon_{PE}) = 2\omega_0 = 2\sqrt{\omega_b^2 + \varepsilon_{PE}}, \quad (5.8)$$

which can be linearised via a Taylor series for small ε_{PE} to

$$\Omega_0 \approx 2\omega_b + \omega_b \varepsilon_{PE}. \quad (5.9)$$

Together Ω_0 and σ_b define the location and the width of the instability interval of the trivial solution (**Fig. 5.9**). All newly introduced parameters and their relation to physical parameters are stated in **Tab. 5.1**. As stated in Eq. (5.9) and Eq. (5.7), the angular centre frequency as well as the borders of the PR (the stability limits) both depend almost linearly on ε_{PE} .

The problem of PR frequency bands not being symmetric around $\Omega_0(\varepsilon_{PE} = 0)$ and widening with increasing ε_{PE} is a known phenomenon of PE systems. It was addressed for example by NAYFEH ET MOOK [24]. In an approach to realise a PE-independent stability limit RHOADS ET AL. [25] propose a tunable linear stiffness to shift the instability wedge in order to tune the system's natural frequency. Their design aims at verticalising either the left or the right border of the instability wedge: the regarding stability border is forced to be perpendicular to the σ - or Ω -axis. Hence the stability limit of interest does not depend on the PE frequency. The stiffness of the additional spring is a function of ε_{PE} . It softens or hardens appropriately with increasing ε_{PE} . However, for a PR wedge symmetric around $\Omega_0(\varepsilon_{PE} = 0)$, it is sufficient to eliminate the time-constant part of $k(x, t)$ in Eq. (3.1). Many systems can be modelled in such a way that $k(x, t)$ can be expressed as $k(x, t) = k_{PE} \cos(\Omega_{PE}t)$ instead of $k(x, t) = k_{PE}(1 + \cos(\Omega_{PE}t))$. Such systems have a symmetric PR, since $\Omega_0 = 2\omega_0 = 2\omega_b = \text{const.}$ Yet, since $\sigma_b(\varepsilon_{PE}) = \varepsilon_{PE}/2\varepsilon\omega_0 \propto \varepsilon_{PE}$, the width of the PR still depends on ε_{PE} .

Table 5.1: Renamed parameters of Eq. (3.7), the 1DOF system depicted in Fig. 3.1.

Parameter	Symbol	Rel. to Physical Par.	Value
Structural Non-linearity Parameter	κ_b^2	$\frac{k_{b, \text{nonlin}} x^{*2}}{m \Omega^{*2}}$	$2.928 \cdot 10^{-2}$
PE Non-linearity Ratio	C_{nonlin}	$\frac{\varepsilon_{\text{nonlin}}}{\varepsilon_{\text{lin}}} = \frac{k_{\text{PE, nonlin}} x^{*2}}{k_{\text{PE, lin}}}$	$-4.383 \cdot 10^{-2}$
Structural Natural Angular Frequency	ω_b	$\frac{k_{b, \text{lin}}}{m \Omega^{*2}}$	2.395

Furthermore, by studying Eqs. (5.4) it becomes clear that the amplitude characteristics qualitatively depend on ε_{PE} , too. The dependence of the five qualitatively different amplitude and phase characteristics, which were determined in Section 3.1.3, on κ_b^2 and ε_{PE} is shown in Fig. 5.10:

- (I) Both branches have softening amplitude characteristics without intersection. The stable branch at PR has a phase shift of $\psi = 0$.
- (II) Both branches have softening amplitude characteristics and intersect. The stable branch at PR has a phase shift of $\psi = 0$.
- (III) One branch has a hardening, one a softening amplitude characteristic and they intersect. The stable branch at PR either has a phase shift of $\psi = 0$ or $\psi = \pi$.
- (IV) Both branches have hardening amplitude characteristics and intersect. The stable branch at PR has a phase shift of $\psi = \pi$.
- (V) Both branches have hardening amplitude characteristics without intersection. The stable branch at PR has a phase shift of $\psi = \pi$.

Increasing or decreasing ε_{PE} at a fixed valued of κ_b^2 can make the system change its characteristics qualitatively, if κ_b^2 is chosen appropriately. For the parameter set in use here, for example, the smallest possible value of κ_b^2 for having a softening amplitude characteristic of both branches \bar{r}_b and \bar{r}_c regardless of the value of ε_{PE} is $\kappa_b^2 = 0$. This means the spring has to have a linear or softening characteristic.

By setting $\kappa_b^2 = 0$, Eq. (3.16c) becomes the only stable solution at PR. Its phase shift ψ is close to 0. The dependence of \bar{r}_c on ε_{PE} and σ is illustrated in Fig. 5.11. For combinations of ε_{PE} and σ sufficiently close to $\sigma = \sigma_b$ and $\varepsilon_{\text{PE}} = 0$, the bifurcation's amplitude \bar{r}_c takes on relative constant values. This means the maximum value \bar{r}_{max} of the amplitude within the PR does not depend much on ε_{PE} (see Fig. 5.11). Within a range of $\varepsilon_{\text{PE}} = [0; 1]$ \bar{r}_{max} only changes by 2.1%.

Employing the case analysis for κ^2 from Section 3.1.3 the parameters of the 1DOF system are tuned to fulfil desired features of the characteristics of the bifurcated limit cycles in Section 5.1.1. Introducing a non-steady PE in Section 5.1.2 the width of the PR, the centre of the PR, the hardening/softening-behaviour of the amplitude characteristics and the phase shift of the stable limit cycles become dependent on the PE magnitude. Strategies are presented to fix the centre of the PR. Investigating a parameter map of the non-linearity parameters gives information about how to set them to not change the system's

qualitative behaviour during operation. Also, it is demonstrated that for certain parameter sets the maximum amplitude of the stable limit cycle at PR is almost independent of the PE magnitude.

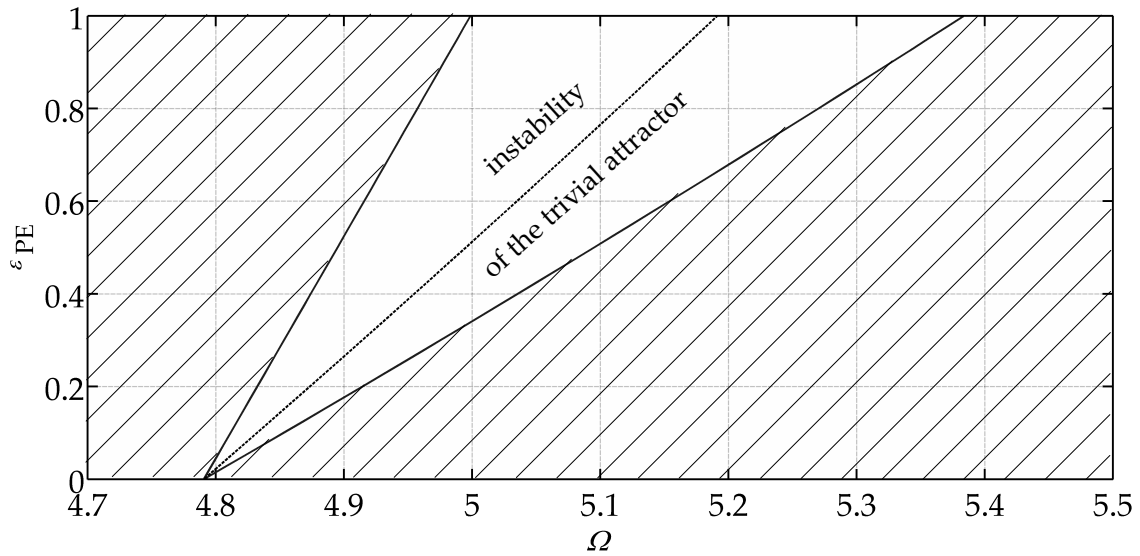


Figure 5.9: Stability chart for the trivial attractor with parameters from **Tab. 3.2** (except for ε_{lin} , $\varepsilon_{\text{nonlin}}$). Hatched: stability area of the trivial attractor—no PR possible. Dashed line: angular centre frequency $\Omega_0 = 2\omega_0$ of the PR. Compare to RHOADS ET AL. [25], Fig. 4a.

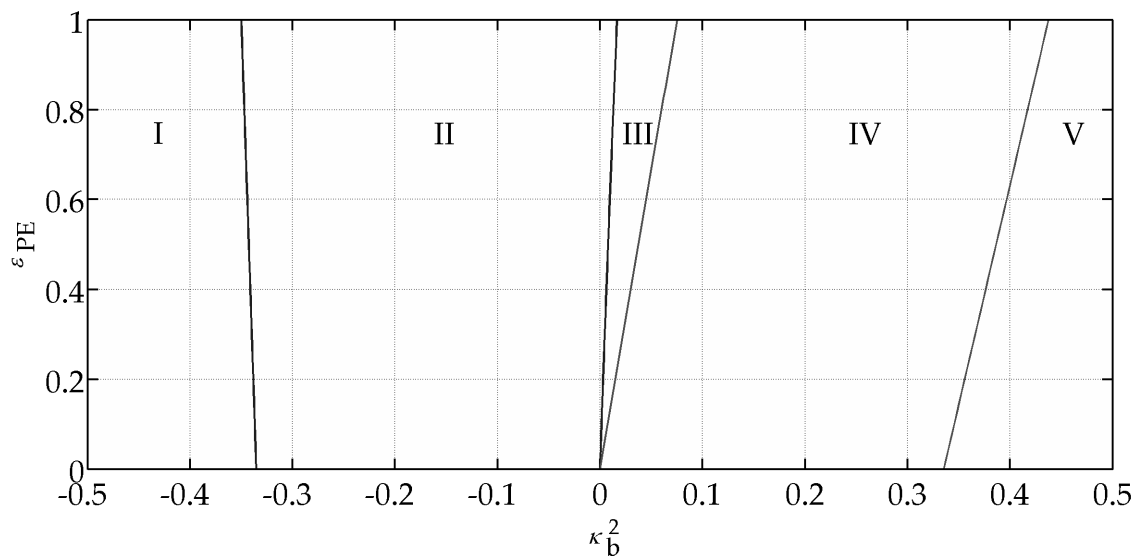


Figure 5.10: Parameter map $\kappa_b^2 - \varepsilon_{\text{PE}}$ indicating five qualitatively different amplitude and phase characteristics (compare **Fig. 3.2**).

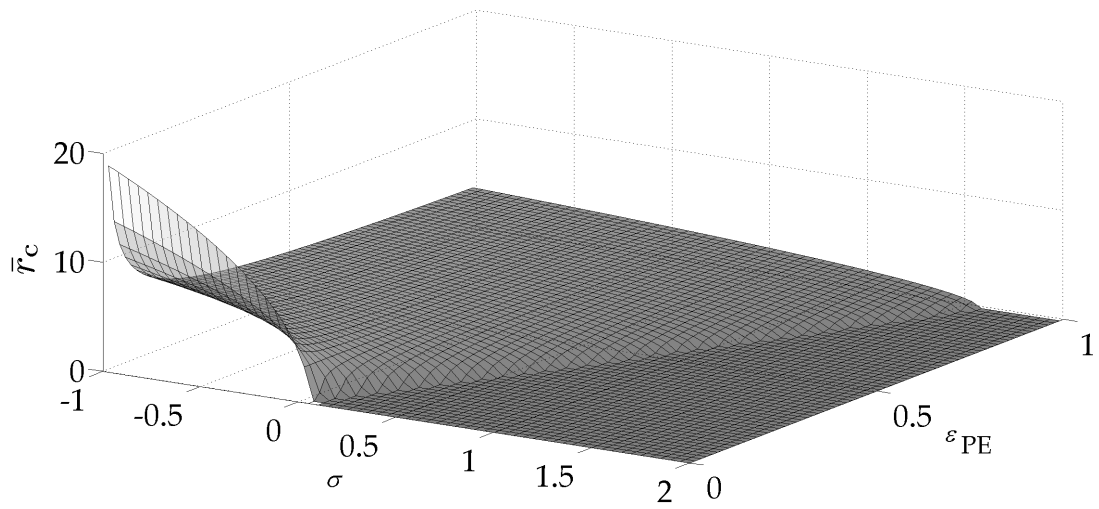


Figure 5.11: Bifurcated limit cycle $\bar{r}_c(\sigma, \varepsilon_{PE})$ with parameters from **Tab. 3.2** (except for $\varepsilon_{lin}, \varepsilon_{nlin}$). The non-linearity parameter has been tuned to $\kappa_b^2 = 0$.

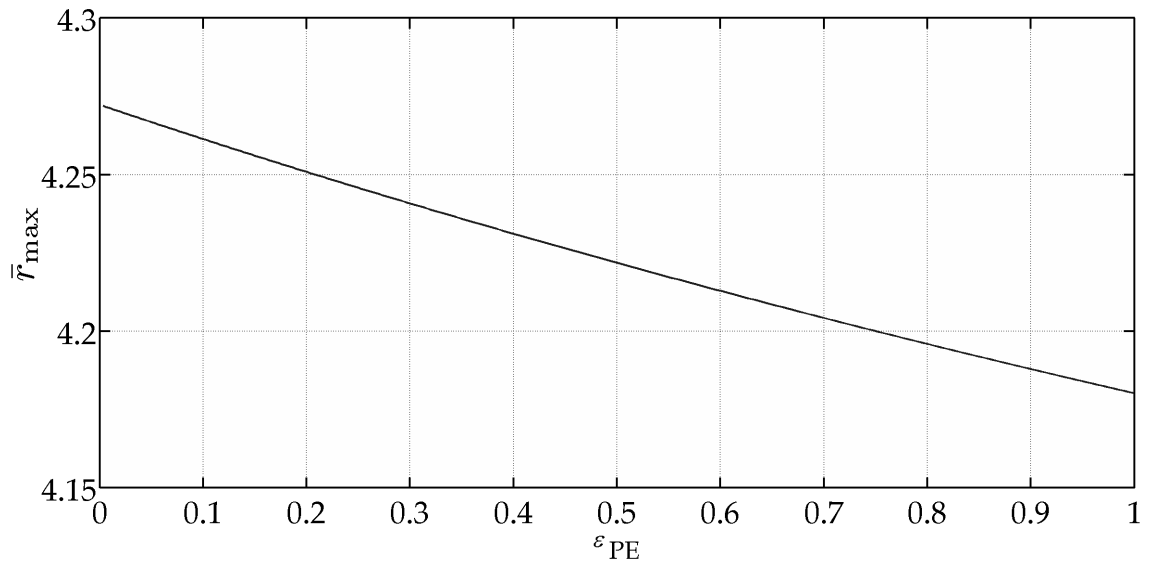


Figure 5.12: Maximum amplitude $\max \left(\bar{r}_c(\sigma, \varepsilon_{PE}) \Big|_{\sigma \in [-\sigma_b, \sigma_b]} \right) = \bar{r}_c(\sigma = -\sigma_b, \varepsilon_{PE})$ of the bifurcated limit cycle.

5.2 Manipulating the Characteristics of the 2DOF System

In Section 3.2.4 it was shown how to approximate a 2DOF non-linear PE system with a 1DOF model. This approach was validated numerically in Section 4.2. The following sections discuss how to manipulate the characteristics of the 2DOF System at PR using the knowledge gained in Section 5.1 and the approach from Section 3.2.4.

5.2.1 Steady Parametric Excitation

The studies for the non-linearity parameter κ^2 in Section 3.1.3 were applied to manipulate the characteristics of the 1DOF system at PR. With the method described in Section 3.2.4 the 2DOF non-linear PE system introduced in Section 3.2.1 can be approximated by a 1DOF system. Hence, the system can be manipulated in analogy to the 1DOF system. Thus, the coupling of the parameters has to be considered, since parameters cannot be tuned independently.

The parameters of the 2DOF system introduced in Section 3.2.3 cause hardening amplitude characteristics at both PRs for both bifurcating limit cycles. Hence, the stable non-trivial solutions at the PRs have a phase shift $\psi_i \approx \pi/2$. In analogy to Section 5.1.1 the characteristics are forced to have softening behaviours, demonstrating how to manipulate the amplitude characteristics of a 2DOF non-linear PE system in general. This is an optimisation of κ_i^2 towards a maximum amplitude r_i and a phase shift $\psi_i \approx 0$ at the PRs if all other parameters remain as stated in **Tab. 3.5**.

To get softening behaviour of both bifurcations at both PRs the non-linearity parameters of interest¹ can be chosen in analogy to Section 5.1.1:

$$\kappa_1^2 \stackrel{!}{\leq} \frac{2\varepsilon_{1,\text{nl}}\omega_1}{3(\omega_1 - \varepsilon\sigma)} \Big|_{\sigma = \frac{-\varepsilon_{1,\text{lin}}}{2\varepsilon\omega_1}} = \frac{4\varepsilon_{1,\text{nl}}\omega_1^2}{3(2\omega_1^2 + \varepsilon_{1,\text{lin}})} = -9.494 \cdot 10^{-6} \xrightarrow{\text{set to}} -1 \cdot 10^{-5}, \quad (5.10a)$$

$$\kappa_2^2 \stackrel{!}{\leq} \frac{2\varepsilon_{2,\text{nl}}\omega_2}{3(\omega_2 - \varepsilon\sigma)} \Big|_{\sigma = \frac{-\varepsilon_{2,\text{lin}}}{2\varepsilon\omega_2}} = \frac{4\varepsilon_{2,\text{nl}}\omega_2^2}{3(2\omega_2^2 + \varepsilon_{2,\text{lin}})} = -3.54 \cdot 10^{-5} \xrightarrow{\text{set to}} -4 \cdot 10^{-5}. \quad (5.10b)$$

To guarantee softening amplitude characteristics even in the case of small numerical mistuning the values were rounded towards smaller values.

The values of κ_i^2 are defined by the transformation from the physical to the quasi-modal coordinates (see Section 3.2.4). For simplification the stiffness of the coupling spring is set equal to the stiffness of a series of the outer springs:

$$k_{12,\text{nl}} = \frac{k_{01,\text{nl}}k_{02,\text{nl}}}{k_{01,\text{nl}} + k_{02,\text{nl}}}. \quad (5.11)$$

The relations between $k_{j,\text{nl}}$ and κ_i^2 reflect the complicated non-linear nature of the problem and cannot be expressed in a simple way. Values for $k_{j,\text{nl}}$ leading to satisfying values for κ_i^2 can be found by numerical trial and error. This means the values for $k_{j,\text{nl}}$ are varied within a certain interval until an acceptable value of κ_i^2 is achieved.

¹See Section 3.2.4 for explanation of how to model a 2DOF non-linear PE system with a 1DOF model at PRs. At PRs only a limited number of parameters of the 2DOF model decide on the behaviour significantly.

Table 5.2: Tuned values of the parameters of Eq. (3.28) for the 2DOF system depicted in Fig. 3.6

Symbol	Value	Unit
$k_{01,\text{nonlin}}$	$0.8878 \cdot 10^9$	Nm^{-3}
$k_{02,\text{nonlin}}$	$3.5644 \cdot 10^9$	Nm^{-3}
$k_{01,\text{nonlin}}$	$0.7108 \cdot 10^9$	Nm^{-3}

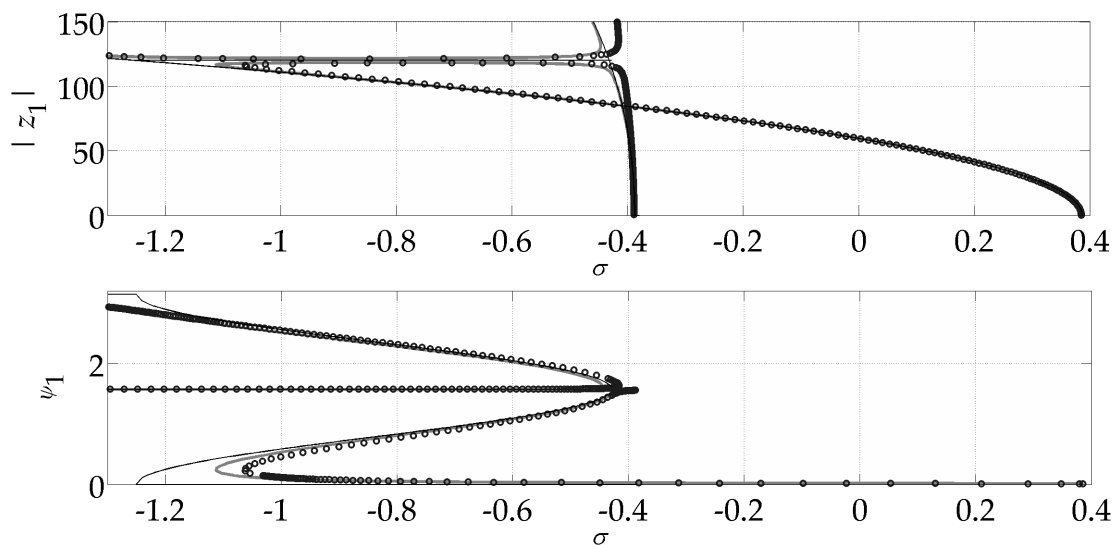
The calculated values for $k_{j,\text{nonlin}}$ are displayed in **Tab. 5.2**. The corresponding values for κ_i^2 are displayed in **Tab. 5.3**. They are within a 0.4% tolerance of the desired values.

The tuning shows the desired effect (see **Fig. 5.13** and **Fig. 5.14**). All amplitudes have softening characteristics. The maximum amplitude within the first PR is $\max(r_1) = r_1(-\sigma_b) = 83.51$. The maximum amplitude within the second PR is $\max(r_2) = r_2(-\sigma_b) = 56.02$. These values are 0.51% and 61.95% higher than for the original parameter set. The small increase of $\max(r_1)$ is because $\kappa_{1,\text{orig}}^2 = 1.081$ already is very close to the value of κ^2 for which the amplitude characteristic r_c becomes softening. Still, the value is maximised by the tuning of the non-linearity parameters. Additionally, the phase shifts $\psi_1 \approx \psi_2 \approx 0$ of the stable limit cycles at PR are realised.

Tuning the characteristics this way in order to achieve $\max\left(\frac{\partial r}{\partial \sigma}\right)$ also becomes visible in the Poincaré maps (see **Fig. 5.15-Fig. 5.19**): close to $\sigma = -\sigma_b$ four limit cycles are visible and the basin of attraction of the trivial attractor is relatively large. The small amplitude node ends up at the very left of the Poincaré maps due to the small phase shift. In contrast to the original parameter set the phase shift increases close to the trivial attractor. Comparing **Fig. 5.15** to **Fig. 5.16** and **Fig. 5.17**, the basin of attraction of the small amplitude node shrinks dramatically within a relatively small range of σ . Meanwhile the basin of attraction of the high amplitude node does not change size significantly. Hence, the basin of attraction of the trivial attractor, which is already large just below the bifurcation of r_b , increases significantly within this small range of σ . A qualitatively similar behaviour can be observed regarding the second PR (see **Fig. 5.18** and **Fig. 5.19**). However, since the slope of the amplitude characteristic r_b is not as large as compared to the first PR, the basin of attraction of the small amplitude node is far more dominant close to the bifurcation of r_b (compare **Fig. 5.18** to **Fig. 5.15**). Nonetheless, this basin of attraction also vanishes within a small range of σ .

Table 5.3: Tuned values of the non-linearity parameters of Eq. (3.48).

Symbol	Value
κ_1^2	$-0.996 \cdot 10^{-5}$
κ_{12}^2	$0.300 \cdot 10^{-5}$
κ_{13}^2	$-0.664 \cdot 10^{-5}$
κ_{14}^2	$-0.160 \cdot 10^{-5}$
κ_{15}^2	$-1.741 \cdot 10^{-5}$
κ_{16}^2	$-2.087 \cdot 10^{-5}$
κ_{26}^2	$+0.047 \cdot 10^{-5}$
κ_{25}^2	$-2.420 \cdot 10^{-5}$
κ_{24}^2	$-2.632 \cdot 10^{-5}$
κ_{23}^2	$0.016 \cdot 10^{-5}$
κ_{22}^2	$-3.629 \cdot 10^{-5}$
κ_2^2	$-4 \cdot 10^{-5}$

**Figure 5.13:** Limit cycles of Eqs. (3.48) for the first quasi-mode $z_1(\tau)$ at $\Omega_0 = 2\omega_1$ for parameters as displayed in **Tab. 5.3**. Thin, black: analytical solution; bold, grey: semi-analytical solution; circles: numerical solution.

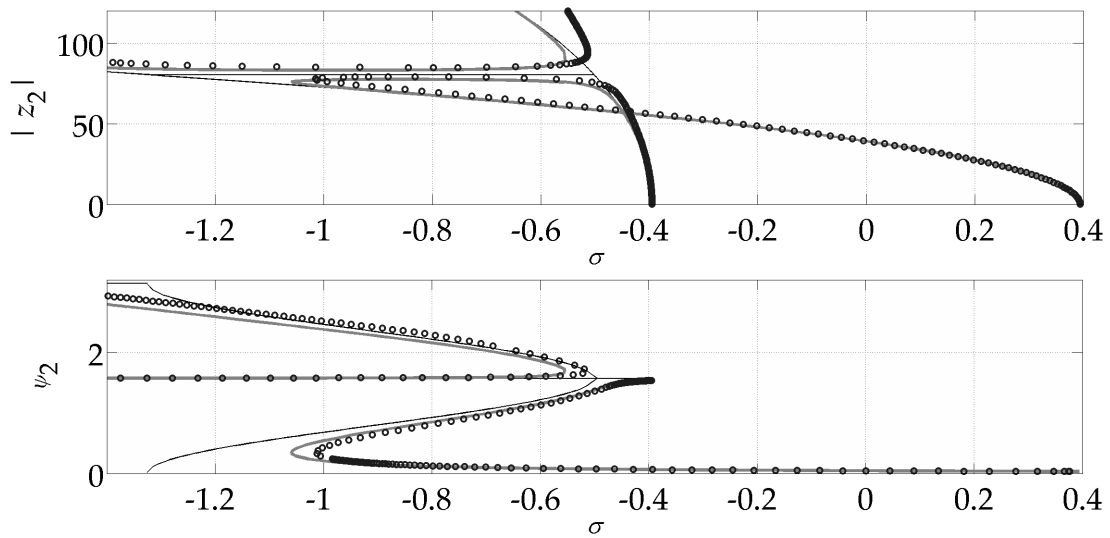


Figure 5.14: Limit cycles of Eqs. (3.48) for the second quasi-mode $z_2(\tau)$ at $\Omega_0 = 2\omega_2$ for parameters as displayed in **Tab. 5.3**. Thin, black: analytical solution; bold, grey: semi-analytical solution; circles: numerical solution.

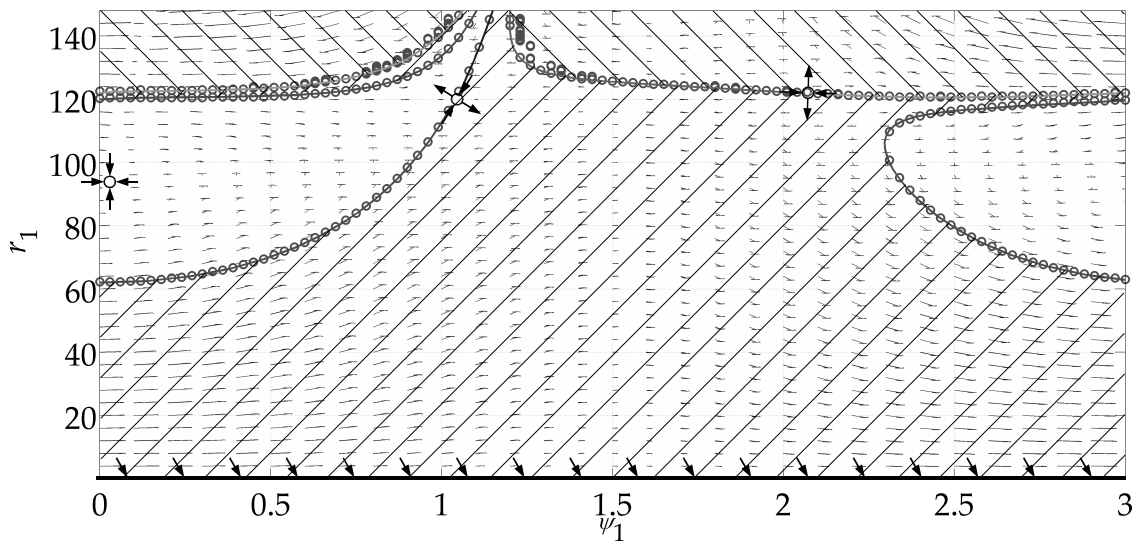


Figure 5.15: Poincaré map, first PR ($\Omega_0 = 2\omega_1$), ψ_1 - r_1 phase space, $\sigma = -0.6$. Two stable attractors: $[0.034, 94.35]$ and $[-, 0]$. Two unstable attractors (saddle points): $[1.05, 118.3]$ and $[2.069, 122.1]$. The high amplitude node lies beyond the amplitude range of the plot. Hatched $+45^\circ$: basin of attraction of the trivial attractor. Hatched -45° : basin of attraction of the high amplitude node. Limit of basins of attraction by numerical scanning (circles) and by backward time integration (line).

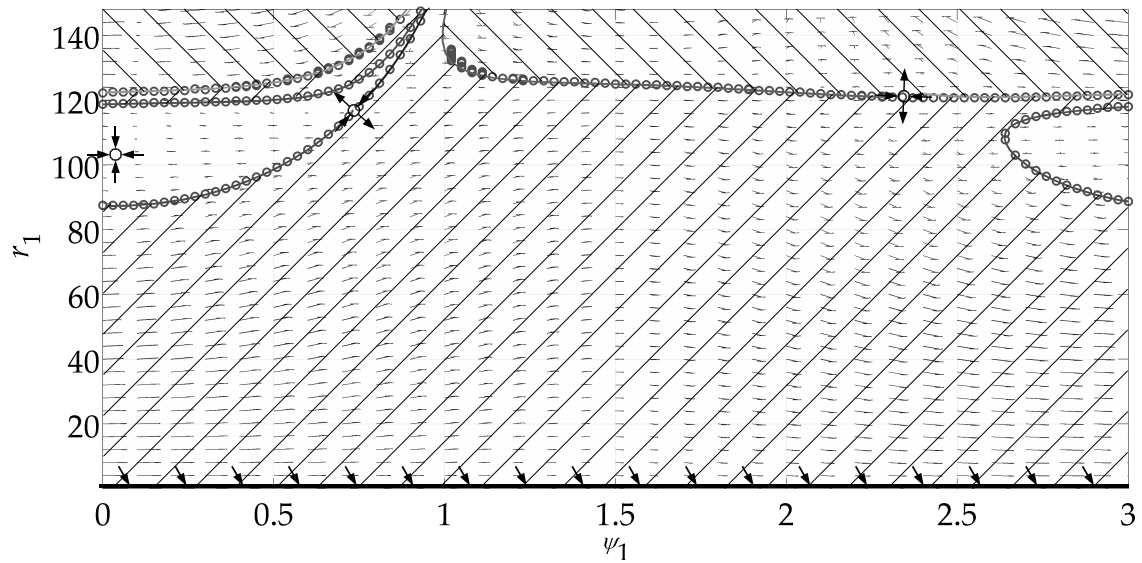


Figure 5.16: Poincaré map, first PR ($\Omega_0 = 2\omega_1$), ψ_1 - r_1 phase space, $\sigma = -0.8$. Two stable attractors: $[0.055, 103.1]$ and $[-, 0]$. Two unstable attractors (saddle points): $[0.781, 118.2]$ and $[2.312, 121.4]$. The high amplitude node lies beyond the amplitude range of the plot. Hatched $+45^\circ$: basin of attraction of the trivial attractor. Hatched -45° : basin of attraction of the high amplitude node. Limit of basins of attraction by numerical scanning (circles) and by backward time integration (line).

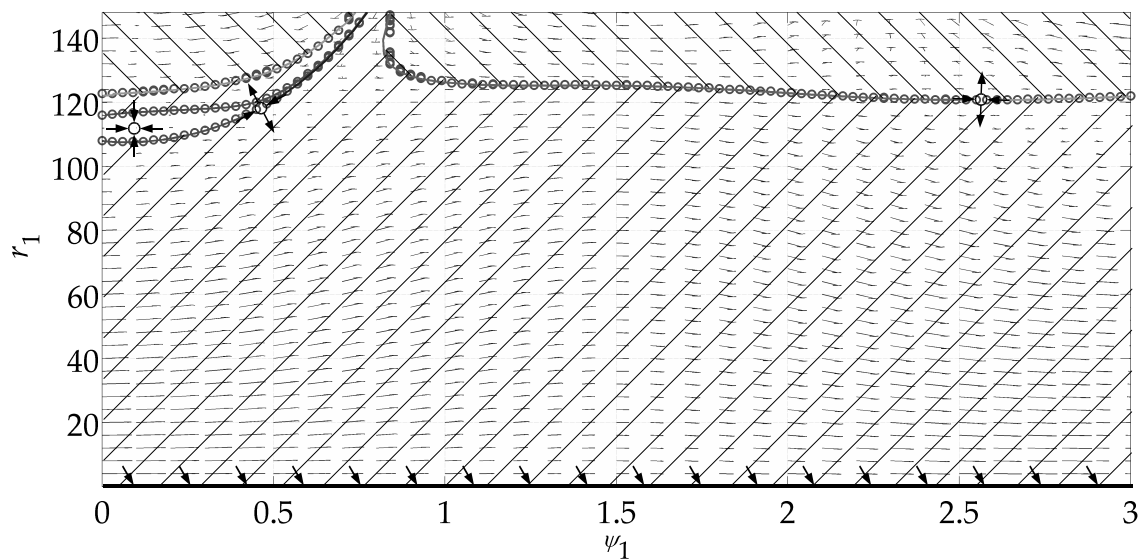


Figure 5.17: Poincaré map, first PR ($\Omega_0 = 2\omega_1$), ψ_1 - r_1 phase space, $\sigma = -1$. Two stable attractors: $[0.118, 112.4]$ and $[-, 0]$. Two unstable attractors (saddle points): $[0.457, 117.4]$ and $[2.550, 121.2]$. The high amplitude node lies beyond the amplitude range of the plot. Hatched $+45^\circ$: basin of attraction of the trivial attractor. Hatched -45° : basin of attraction of the high amplitude node. Limit of basins of attraction by numerical scanning (circles) and by backward time integration (line).

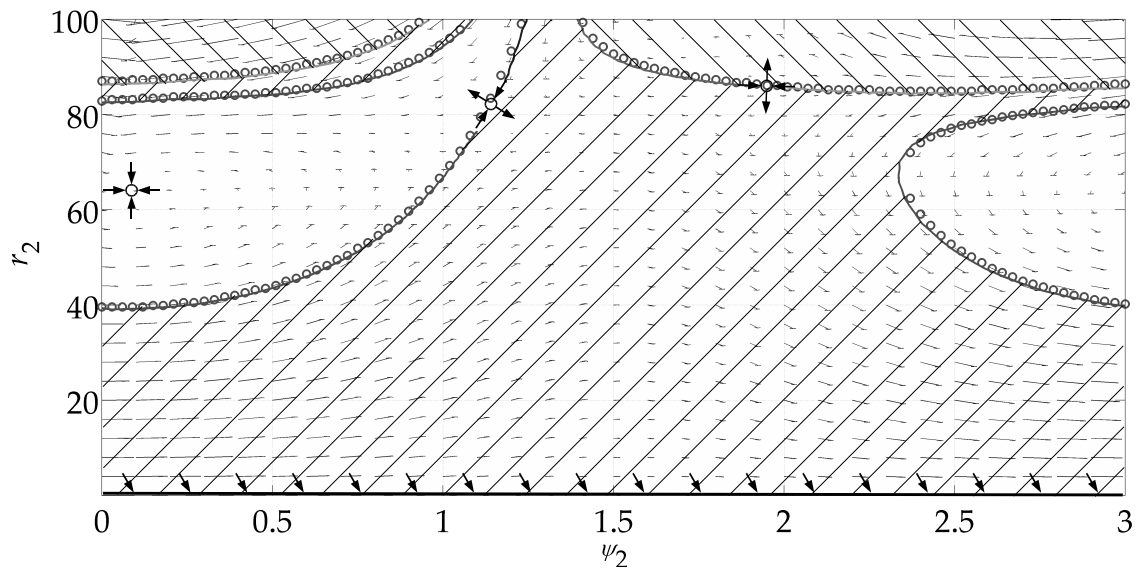


Figure 5.18: Poincaré map, second PR ($\Omega_0 = 2\omega_2$), ψ_2 - r_2 phase space, $\sigma = -0.6$. Two stable attractors: $[0.086, 63.38]$ and $[-, 0]$. Two unstable attractors (saddle points): $[1.131, 77.93]$ and $[1.928, 85.69]$. The high amplitude node lies beyond the amplitude range of the plot. Hatched $+45^\circ$: basin of attraction of the trivial attractor. Hatched -45° : basin of attraction of the high amplitude node. Limit of basins of attraction by numerical scanning (circles) and by backward time integration (line).

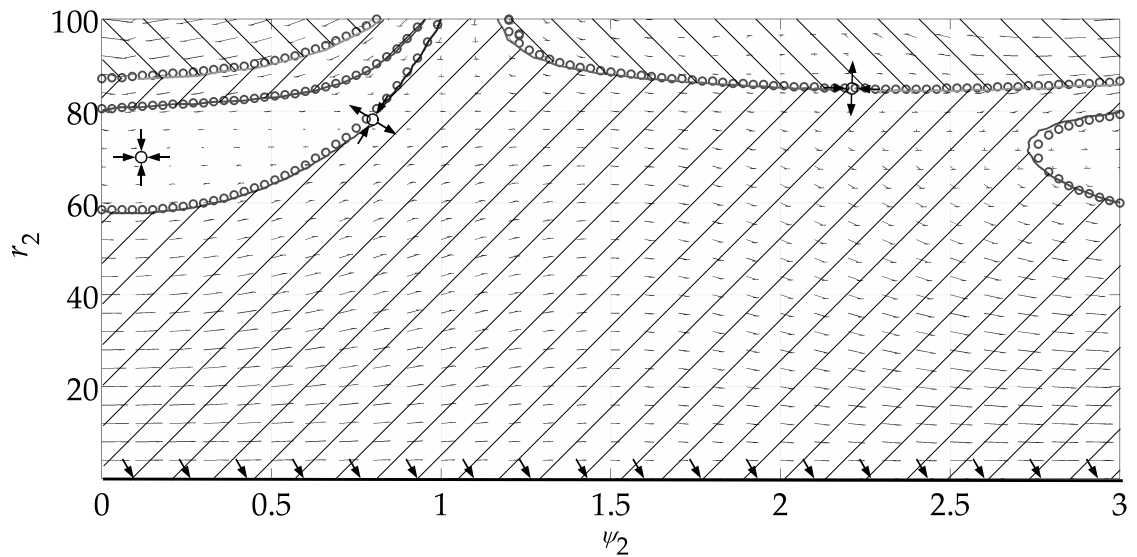


Figure 5.19: Poincaré map, second PR ($\Omega_0 = 2\omega_2$), ψ_2 - r_2 phase space, $\sigma = -0.8$. Two stable attractors: $[0.127, 69.24]$ and $[-, 0]$. Two unstable attractors (saddle points): $[0.827, 79.10]$ and $[2.284, 84.79]$. The high amplitude node lies beyond the amplitude range of the plot. Hatched $+45^\circ$: basin of attraction of the trivial attractor. Hatched -45° : basin of attraction of the high amplitude node. Limit of basins of attraction by numerical scanning (circles) and by backward time integration (line).

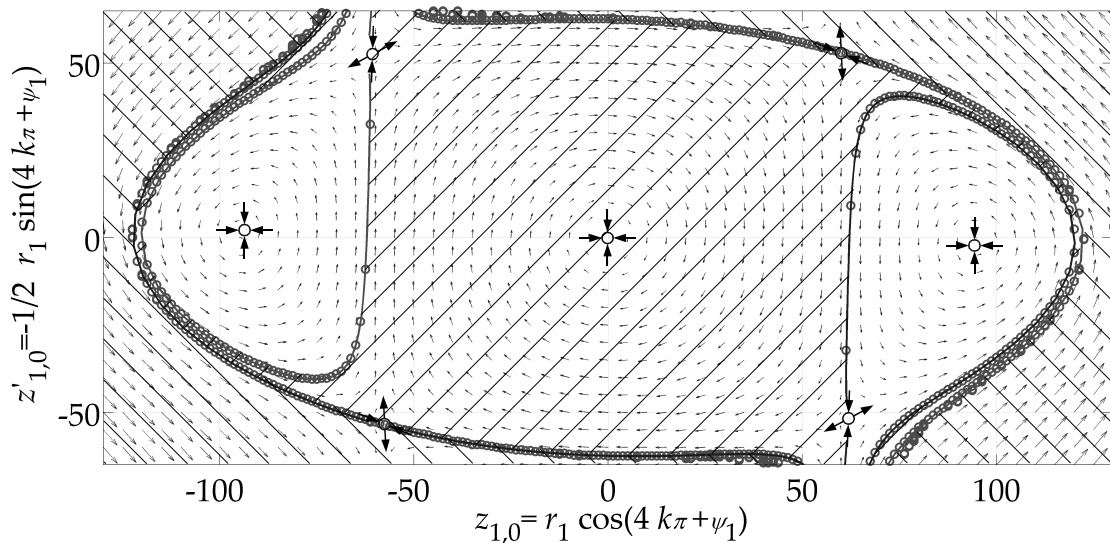


Figure 5.20: Poincaré map, first PR ($\Omega_0 = 2\omega_1$), z_1 - z_1' phase space, $\sigma = -0.6$. Three stable attractors: $[\pm 94.30, \mp 1.603]$ and $[0, 0]$. Four unstable attractors (saddle points): $[\pm 58.76, \mp 51.34]$ and $[\mp 58.34, \mp 53.63]$. The high amplitude node lies beyond the amplitude range of the plot. Hatched $+45^\circ$: basin of attraction of the trivial attractor. Hatched -45° : basin of attraction of the high amplitude node. Limit of basins of attraction by numerical scanning (circles) and by backward time integration (line).

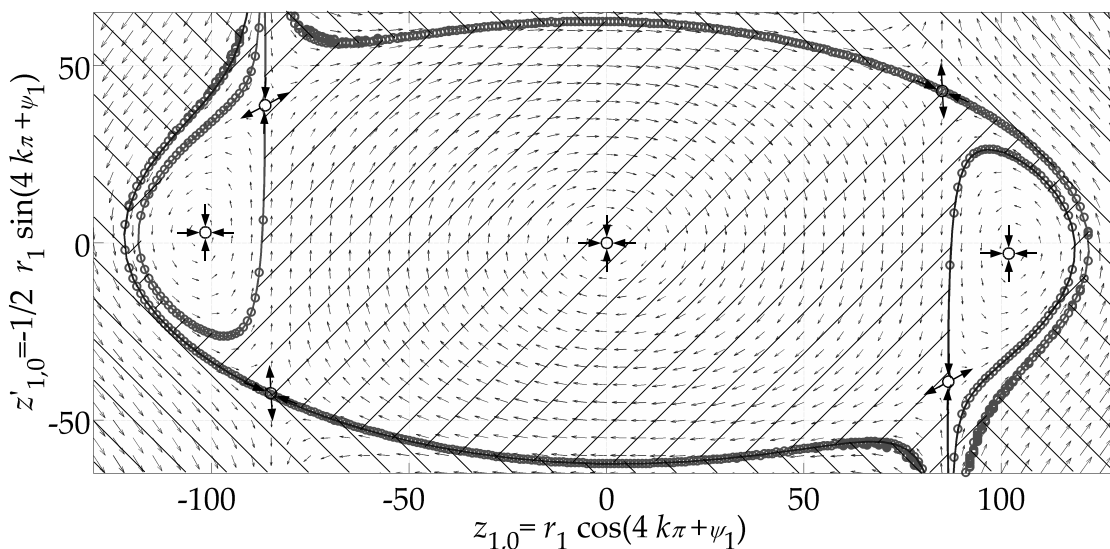


Figure 5.21: Poincaré map, first PR ($\Omega_0 = 2\omega_1$), z_1 - z_1' phase space, $\sigma = -0.8$. Three stable attractors: $[\pm 102.94, \mp 2.834]$ and $[0, 0]$. Four unstable attractors (saddle points): $[\pm 83.95, \mp 41.61]$ and $[\mp 81.97, \mp 44.78]$. The high amplitude node lies beyond the amplitude range of the plot. Hatched $+45^\circ$: basin of attraction of the trivial attractor. Hatched -45° : basin of attraction of the high amplitude node. Limit of basins of attraction by numerical scanning (circles) and by backward time integration (line).

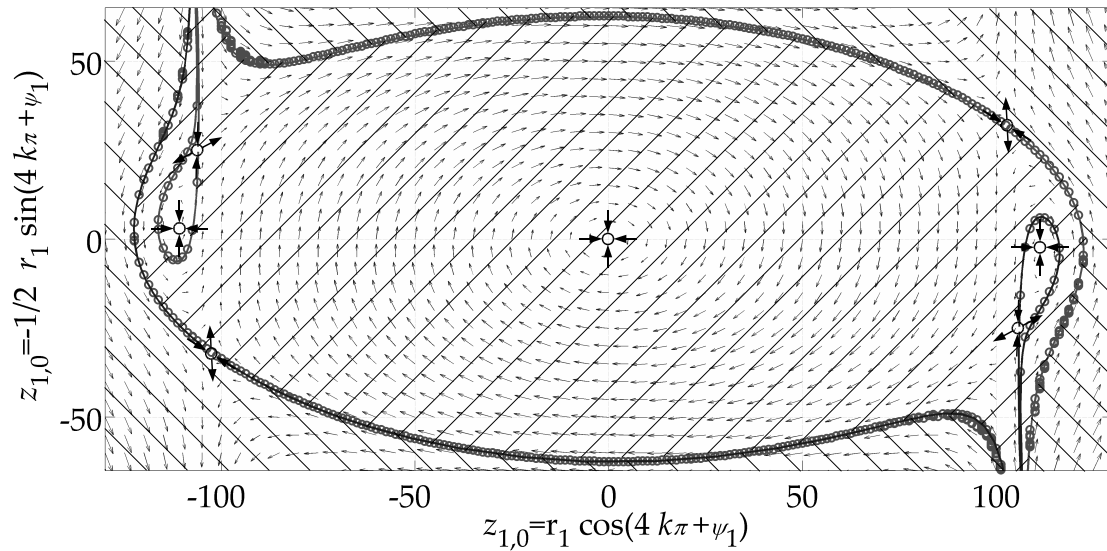


Figure 5.22: Poincaré map, first PR ($\Omega_0 = 2\omega_1$), z_1 - z_1' phase space, $\sigma = -1$. Three stable attractors: $[\pm 111.62, \mp 6.616]$ and $[0, 0]$. Four unstable attractors (saddle points): $[\pm 105.35, \mp 25.90]$ and $[\mp 100.60, \mp 33.80]$. The high amplitude node lies beyond the amplitude range of the plot. Hatched $+45^\circ$: basin of attraction of the trivial attractor. Hatched -45° : basin of attraction of the high amplitude node. Limit of basins of attraction by numerical scanning (circles) and by backward time integration (line).

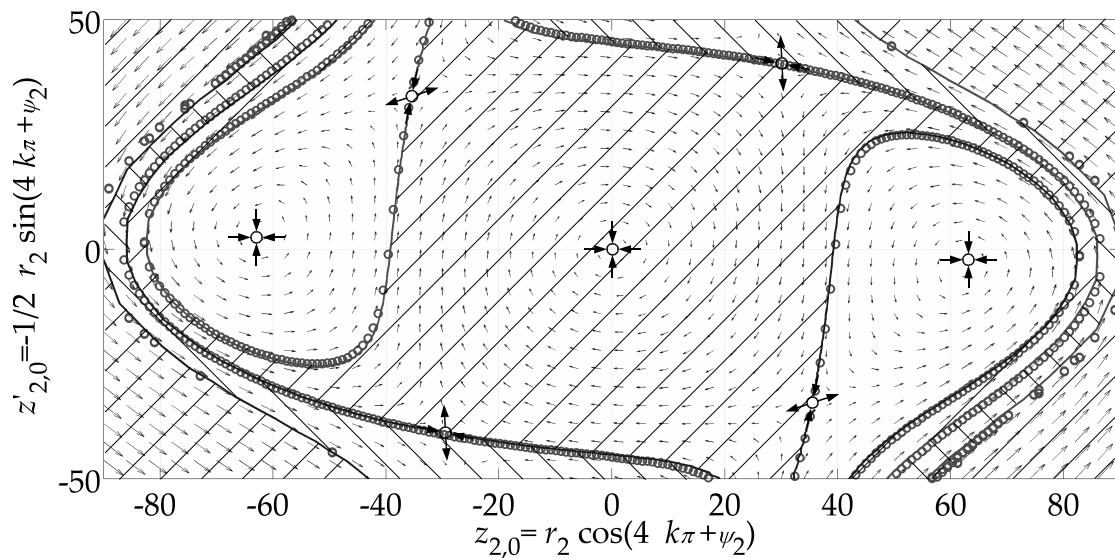


Figure 5.23: Poincaré map, second PR ($\Omega_0 = 2\omega_2$), z_2 - z_2' phase space, $\sigma = -0.6$. Three stable attractors: $[\pm 63.15, \mp 2.722]$ and $[0, 0]$. Four unstable attractors (saddle points): $[\pm 33.18, \mp 35.26]$ and $[\mp 29.96, \mp 40.14]$. The high amplitude node lies beyond the amplitude range of the plot. Hatched $+45^\circ$: basin of attraction of the trivial attractor. Hatched -45° : basin of attraction of the high amplitude node. Limit of basins of attraction by numerical scanning (circles) and by backward time integration (line).

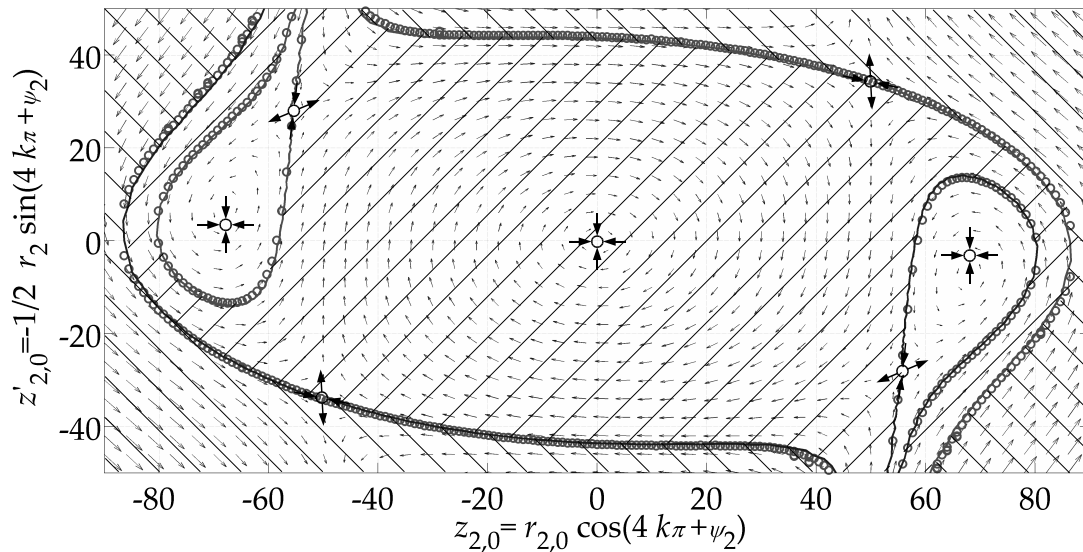


Figure 5.24: Poincaré map, second PR ($\Omega_0 = 2\omega_2$), z_2 - z'_2 phase space, $\sigma = -0.8$. Three stable attractors: $[\pm 68.68, \mp 4.385]$ and $[0, 0]$. Four unstable attractors (saddle points): $[\pm 53.56, \mp 29.10]$ and $[\mp 55.47, \mp 32.06]$. The high amplitude node lies beyond the amplitude range of the plot. Hatched $+45^\circ$: basin of attraction of the trivial attractor. Hatched -45° : basin of attraction of the high amplitude node. Limit of basins of attraction by numerical scanning (circles) and by backward time integration (line).

The bifurcated branches are plotted in a reduced three-dimensional σ - ψ_i - z_i parameter phase space for providing a better understanding of the interdependencies of z_i and ψ_i . Displaying the lowest border (surface grid) between the basins of attraction of the bifurcated limit cycle (line) and the stable equilibrium demonstrates the power of each attractor in attracting the system. In this three-dimensional parameter phase space, the stable equilibrium is a region defined by $z_i = 0$, ψ_i arbitrary and $\sigma < -0.3872$ at the first PR, $\sigma < -0.3955$ at the second PR respectively.

The measure $P = \frac{r_{\text{border}}}{|z|} \Big|_{\sigma=2\sigma_b}$ introduced in Section 4.1.2 quantifies this nature. At the first PR it takes on the value of $P = 0.795$. This means an increase of 3% compared to the results by analysing the original parameter set stated in Section 4.2. At the second PR it takes on the value of $P = 0.81$ which means an increase of 154% compared to the original results. By reducing κ^2 the amplitude characteristics have been amplified, diverging from the trivial attractor much faster in terms of σ . The risk of the system being attracted by a non-trivial attractor starting with a small but non-zero amplitude is reduced at both PRs. At the second PR the increase in P is significant.

The 2DOF system can be manipulated in analogy to Section 5.1.2. The non-linearity parameters κ_i^2 can be chosen according to the case analyses in Section 3.1.3. But due to the complicated non-linear interdependencies between physical and non-dimensional parameters an analytical relation cannot be given. Hence, the physical parameters have to be optimised with respect to the desired values of the non-linearity parameters κ_i^2 . For the presented system at both PRs the phase shift of the bifurcated limit cycles is eliminated, the amplitudes are amplified and the risk of the system being attracted by a non-trivial attractor is reduced.

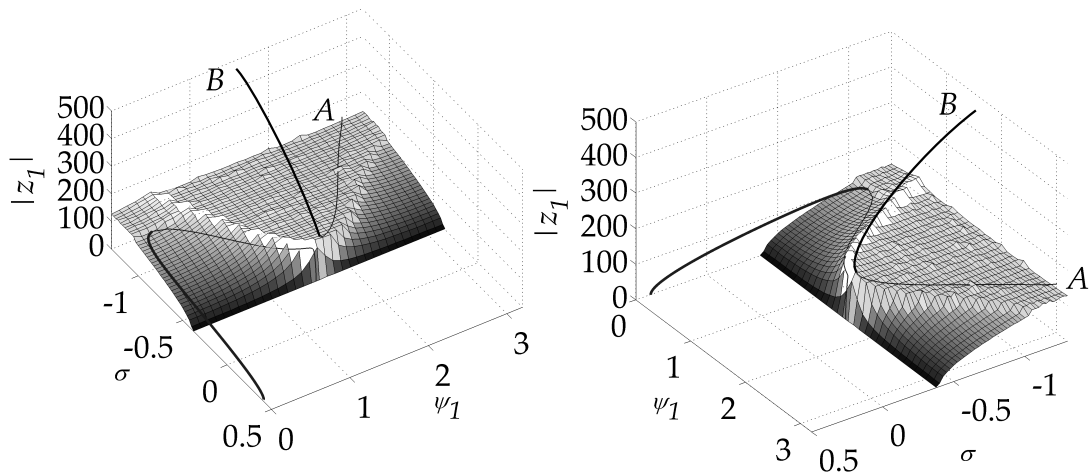


Figure 5.25: First PR ($\Omega_0 = 2\omega_1$). Lowest border (surface grid) between the basins of attraction of the bifurcated limit cycle (line) and stable trivial solutions ($[<-0.3872,-,0]$ plane) in the reduced σ - ψ_1 - z_1 phase parameter space. Stable states along the bifurcated branches are indicated as bold. Unstable states (plotted thinly) along the branches are a subset of the border between the basins of attraction and are part of the surface displayed here. The second loop enters/leaves the displayed part of the phase parameter space at $A = [-1.3, 2.932, 128.8]$ and $B = [-1.3, \pi/2, 487.1]$.

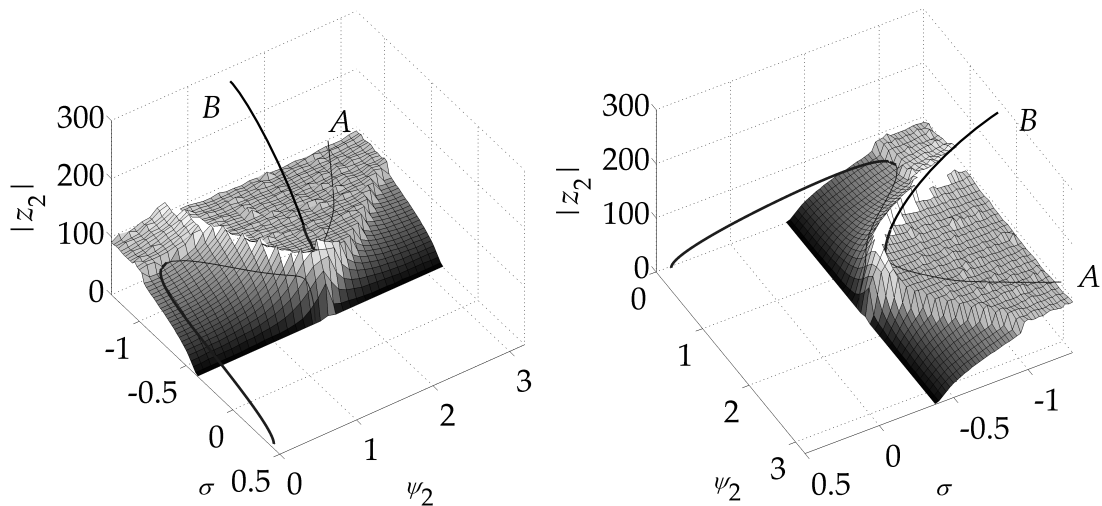


Figure 5.26: Second PR ($\Omega_0 = 2\omega_2$). Lowest border (surface grid) between the basins of attraction of the bifurcated limit cycle (line) and stable trivial solutions ($[<-0.3955,-,0]$ plane) in the reduced σ - ψ_2 - z_2 phase parameter space. Stable states along the bifurcated branches are indicated as bold. Unstable states (plotted thinly) along the branches are a subset of the border between the basins of attraction and are part of the surface displayed here. The second loop enters/leaves the displayed part of the phase parameter space at $A = [-1.3, 2.826, 91.65]$ and $B = [-1.3, \pi/2, 282.3]$.

5.2.2 Non-steady Parametric Excitation

In the previous section, tuning the non-linearity parameters of a 2DOF non-linear PE system for fulfilling certain requirements such as eliminating the phase shift or maximising the amplitudes of the bifurcated limit cycles was discussed. Analytic conditional equations were given. However, the approach presented is only applicable, if the PE has a constant amplitude. If the PE amplitude fluctuates slowly, the system's behaviour is not only determined by the non-linearities of the time-invariant stiffnesses but also by the actual magnitude of the PE.

Approximating the 2DOF system at PRs with a corresponding 1DOF system as established in Section 3.2.4, the results from Section 5.1.2 could be employed. However, analytic expressions for κ_i^2 and subsequently for \bar{r}_i as well as for ω_i cannot be given.

The stability charts for both PRs can be evaluated numerically (see **Fig. 5.27** and **Fig. 5.28**). The original parameters of **Tab. 3.5** are employed, only the magnitude of the PE is varied so that $\varepsilon_{1,\text{lin}}$ and $\varepsilon_{2,\text{lin}}$ both take on values within $[0, 1]$. In analogy to Section 5.2.2 the angular centre frequencies of the PRs depend almost linearly on $\varepsilon_{i,\text{lin}}$. Since the value of the bifurcation points $\sigma = \mp\sigma_b$ is proportional to $\varepsilon_{i,\text{lin}}$, the stability border $\Omega_0 \mp \sigma_b$ shows an almost linear dependency.

As derived in Section 5.1.1 the centre frequencies increase almost proportionally with $\Delta\Omega_0 = \omega_i|_{\varepsilon_{i,\text{lin}}=0} \Delta\varepsilon_{i,\text{lin}}$. The bandwidth also increases almost proportionally with $\Delta\sigma_b = \frac{\Delta\varepsilon_{i,\text{lin}}}{\varepsilon\omega_i|_{\varepsilon_{i,\text{lin}}=0}}$. Note, that having a non-steady $\varepsilon_{i,\text{lin}}$ is sufficient alone, $\varepsilon_{i,\text{nl}}$ does not have to be non-steady necessarily to get these effects.

Further investigations are computationally too expensive for the 2DOF system to be presented here. In difference to the 1DOF system, analytic expressions for κ_i^2 cannot be provided. For the 2DOF system κ_i^2 result from the quasi-modal transformation of the equations of motion and depend on the entries of the non-linear stiffness matrices \mathbf{K}_{nl} in a complicated manner. Hence, analytic expressions for the amplitude characteristics like Eqs. (5.4) cannot be given. Thus, the qualitative behaviour cannot be determined and a parameter map like **Fig. 5.10** cannot be presented.

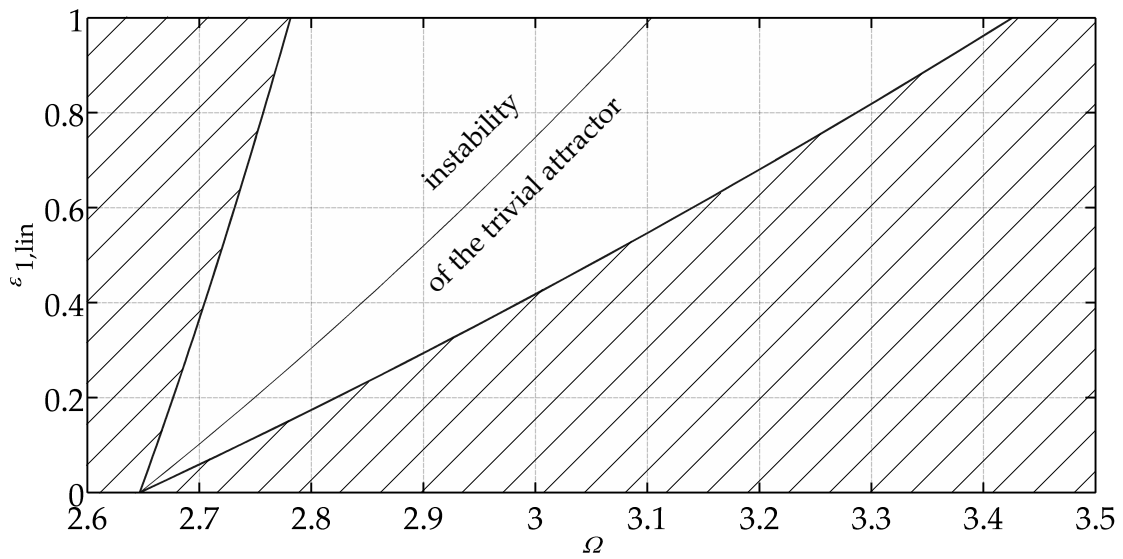


Figure 5.27: Stability chart for the trivial attractor at the first PR with parameters from **Tab. 3.5** (except for $\varepsilon_{i,lin}, \varepsilon_{i,nlin}$). Hatched: stability area of the trivial attractor—no PR possible. Thin line: angular centre frequency $\Omega_0 = 2\omega_1$ of the PR.

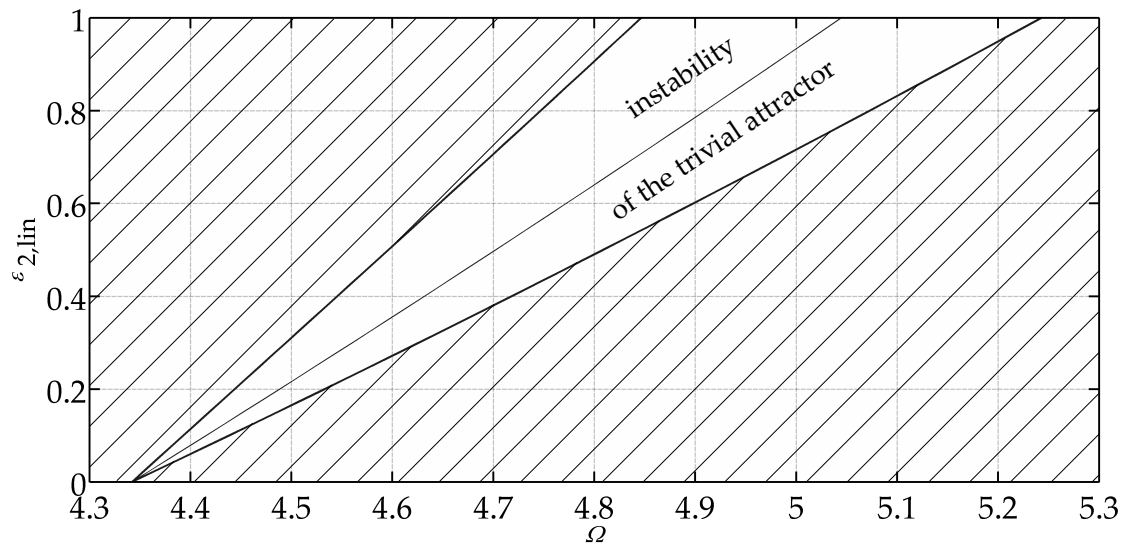


Figure 5.28: Stability chart for the trivial attractor at the second PR with parameters from **Tab. 3.5** (except for $\varepsilon_{i,lin}, \varepsilon_{i,nlin}$). Hatched: stability area of the trivial attractor—no PR possible. Thin line: angular centre frequency $\Omega_0 = 2\omega_2$ of the PR.

5.3 Achievements of Manipulating the Characteristics

The findings in Chapter 3 and Chapter 4 were applied successfully in manipulating the characteristics of both the 1DOF and the 2DOF non-linear PE system introduced earlier. PEs with constant amplitudes and such with non-constant amplitudes, which change slowly compared to the PE frequency, were discussed.

In case of steady PE amplitudes, it was demonstrated for the 1DOF and 2DOF system how to tune parameters in order to modify the characteristics of the bifurcated stable limit cycle at PR. The analytic results from Section 3.1.3 were employed leading to analytic expressions and straight forward tuning algorithms. As a result the phase shifts can be changed from $\pi/2$ to 0 and vice versa, the amplitudes can be maximised and the risk of the system being attracted by a non-trivial attractor close to a PR can be reduced.

Discussing the basins of attraction of the stable limit cycles at or close to the PRs, a different behaviour compared to the original systems can be observed: straightening of the amplitude characteristics, two stable limit cycles exist very close to the borders of the PR. The stable high amplitude limit cycle influences the basins of attraction of both the trivial attractor and the non-trivial low amplitude attractor more strongly than in the original systems.

In case of non-steady PE the qualitative behaviour of the system can change by the variation of the PE amplitudes. For the 1DOF system, analytical findings from Section 3.1.3 can be utilised to find limit cases for the steady part of the non-linearity parameter. This way the system can be designed to behave qualitatively the same regardless of the PE amplitude. Also, the maximum amplitude at PR can be shown to be almost independent of the PE amplitude for a certain parameter set.

For the 2DOF system, the analytic results from Chapter 3 cannot be employed due to the fact that the transformation from physical displacements to the quasi-modal displacements could not be described analytically in Chapter 4. The drift of the PR angular centre frequency and the widening of the PR depending on the magnitude of the PE amplitude is investigated. An analytical statement regarding the values of certain parameters for which the qualitative behaviour of the system does not change cannot be given. To make such a statement numerical methods have to be employed.

6 Applications

In Chapter 3 1DOF and 2DOF non-linear PE systems have been studied analytically in order to understand the influences of the parameters on the behaviour of these systems at PRs. Parameter regimes could be identified for which the systems show certain qualitative behaviours. Analytical and semi-analytical expressions of the relation between parameter values and the amplitudes and phase shifts of the vibrations at PR were deduced. These findings were validated numerically in Chapter 4. In addition, the basins of attraction of the coexisting stable states at PRs were identified. Based on these results the aspect of enlarging certain basins of attraction for ensuring the attraction of the system to the desired state was addressed. Finally in Chapter 5 the results made previously were employed to optimise the systems' behaviour at PR regarding amplitude and phase shift of the vibrations at PR. Design rules were given.

The results made in those chapters are of general nature and can be applied to any system which can be modelled as in Section 3.1.1 or Section 3.2.1. However, in this chapter three microelectromechanical Systems (MEMS) are presented for demonstrating the benefits of the research findings. All of these systems have been manufactured yet. They specifically use PE actively to outperform standard systems. Yet, so far all of them are limited to 1DOF.

In each section first the system is explained. It is shown how each system takes advantage of certain features of the PE. Referring to Chapter 5 possibilities of tuning the system are illustrated. In the end it is sketched out what extending each system from 1DOF to 2DOF means and which further benefits can be exploit.

6.1 MEMS Energy Harvester for Health Monitoring

In medical engineering the number of applications for wirelessly continuously monitoring the patient's health increase steadily. Such systems are necessary for monitoring high risk patients or patients with chronic diseases. With rapidly ageing societies in industrial countries the demand for these systems grows fast. Health parameters of interest are, for example, blood pressure, body core temperature or Electrocardiogram (ECG) signals [27].

A main problem of such devices is realising the necessary energy supply. An autonomous energy supply by energy harvesters means a comfortable wireless and low maintenance solution for the patient. These energy harvesters convert body movements to electric energy for supplying the monitoring system.

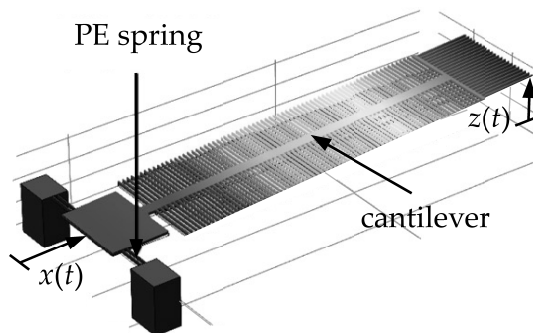


Figure 6.1: MEMS Energy Harvester from [26]. The PE spring causes a longitudinal vibration of the cantilever's clamp. This resembles a periodic change of the cantilever's effective stiffness.

Vibrating cantilevers which are externally excited by body movements are a common choice for energy harvester designs. The cantilever's vibrations result in large displacements at the free end and large tensions at the clamped end. Large displacements at the free end means high efficiency of electromagnetic and -static transducers, while large tensions at the clamped end mean high efficiency of piezoelectric transducers [26]. For further increasing the efficiency of electromagnetic and -static transducers [28] suggests to excite the cantilever auto-parametrically (see **Fig. 6.1**). Instead of using the body movements directly to excite the cantilever externally, these movements destabilize the rest position. The transducer is excited parametrically. The cantilever's clamped end is mounted flexibly, which allows a longitudinal vibration. With simplifications the movement of the clamped end and can be modelled as a harmonically forced oscillation and the cantilever as a 1DOF system (see **Fig. 6.2a**). Hence, the system can be approximated mathematically by

$$\ddot{z} + 2\zeta \sqrt{\frac{3EI}{m_{\text{eff}}l_{\text{eff}}^3}} \dot{z} + \left(\frac{3EI}{m_{\text{eff}}l_{\text{eff}}^3} + \frac{\Omega_{\text{PE}}^2 \hat{x}}{l_{\text{eff}}} \cos(\Omega_{\text{PE}}t) \right) z + \mu z^3 = 0. \quad (6.1)$$

Here E represents Young's modulus, I the area moment of inertia, m_{eff} the effective mass, l_{eff} the effective length, Ω_{PE} the angular frequency and \hat{x} the amplitude of the clamped end's longitudinal vibration, ζ the damping ratio and μ a non-linear stiffness of the cantilever.

In fact, with the design configurations presented in [26] (see **Fig. 6.1**) modelling the system as depicted in **Fig. 6.2a** is a rather inappropriate approach. The PE spring's torsional stiffness is not sufficient to model the beam's end as clamped. Quite the contrary, it barely supports the beam in terms of a rotation about the y -axis. If the spring's torsional stiffness is significantly smaller than the beam's bending stiffness, the system can be modelled as depicted in **Fig. 6.2c**. This leads to the equation of motion

$$\ddot{z} + \frac{c_{\varphi}}{m_{\text{eff}}l_{\text{eff}}^2} \dot{z} + \left(\frac{k_{\varphi}}{m_{\text{eff}}l_{\text{eff}}^2} + \frac{\Omega_{\text{PE}}^2 \hat{x}}{l_{\text{eff}}} \cos(\Omega_{\text{PE}}t) \right) z + \mu z^3 = 0. \quad (6.2)$$

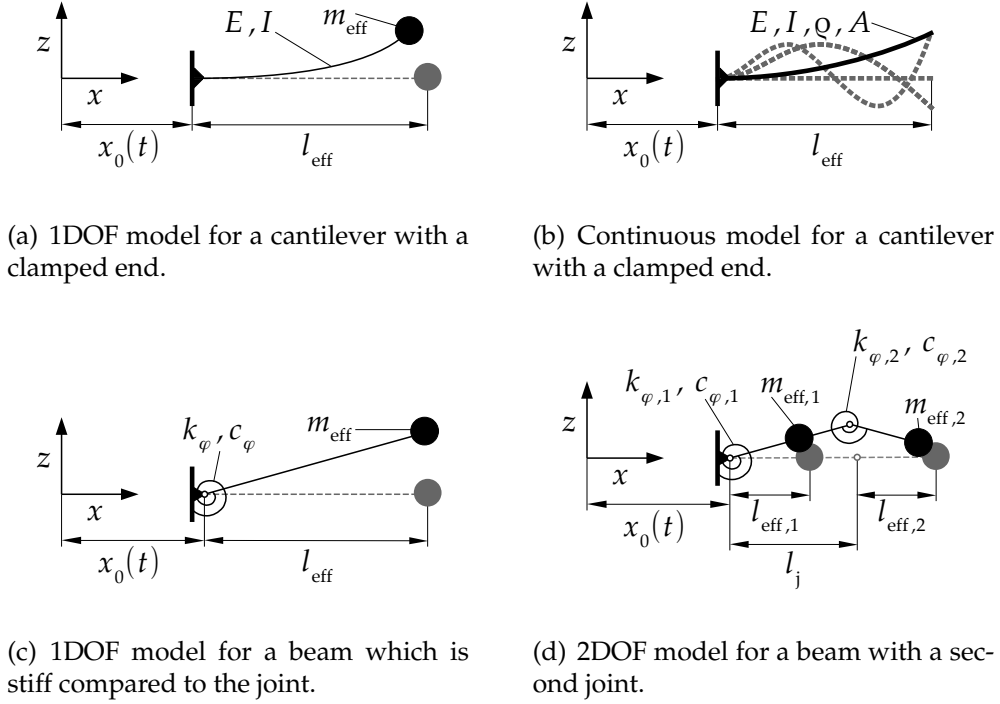


Figure 6.2: Mechanical models for a system as depicted in Fig. 6.1. The cantilever's clamped end vibrates along the x -axis with $x_0(t) = \hat{x} \cos(\Omega_{PE}t)$. Hence, the cantilever's vibration is excited parametrically. (a)-(c) represent different modelling approaches for the system in [26], while (d) shows an alternative design.

Here, k_φ is the spring's effective torsional stiffness and c_φ is the spring's effective torsional damping. The parameter μ represents the non-linearity of the torsional characteristic of the PE spring.

However, renaming the parameters and introducing the eigentime $\tau = \Omega_{PE}t$ Eq. (6.1) and Eq. (6.2) both can be written as Eq. (3.4):

$$m \Omega_{PE}^2 x'' + c \Omega_{PE} x' + k_{b,lin} x + k_{b,nlin} x^3 + (k_{PE,lin} x + k_{PE,nlin} x^3)(1 + \cos(\tau)) = 0.$$

In this case there is no non-linear PE ($\varepsilon_{nlin} = 0$). Also, the free end's transverse vibration's angular natural frequency

$$\omega_0 = \sqrt{\frac{3EI}{m_{eff}l_{eff}^3}}, \quad \omega_0 = \sqrt{\frac{k_\varphi}{m_{eff}l_{eff}^2}}, \quad \text{resp.} \quad (6.3)$$

does not depend on the amplitude \hat{x} of the longitudinal PE. Since $\mu > 0 \Rightarrow \kappa^2 > 0$, both amplitudes \bar{r}_b and \bar{r}_b of the bifurcated branches show hardening characteristics. At PR only Eq. (3.16b) is a stable limit cycle in this case.

This PE design outperforms ordinary cantilever energy harvesters due to two effects: Operating the system at an instability of the rest position instead of at resonance means

larger amplitudes of the free end's traversal oscillation. This leads to higher energy conversion efficiency when employing electromagnetic or -static transducers. More importantly, the longitudinal PE needs only very small amplitudes to destabilize the cantilever. Whereas an ordinary design needs an appropriate external excitation at a resonance frequency. In a health application the energy input into the system mostly is by shocks, noise or broadband vibrations of the surrounding tissue. The PE design can make use of small amplitudes of signal components with PE frequency. Hence, the cantilever is much more likely to be excited in average over time. Note that the presented design adds PE to the existing external excitation mechanism and does not substitute the existing external excitation mechanism.

Extending the system to more degrees of freedom means more PRs and PCR to be exploit. With little damping being present in the system energy dissipation at PARs will not be significant. For health applications extending the number of PRs and PCR is a promising way to increase the efficiency by overcoming the problem of only using a very limited bandwidth of the tissue's vibration.

The system can be extended to more degrees of freedom in two different ways at least. If the device can be modelled with a clamped cantilever, examining the continuous model and investigating modes up to the order desired is possible (see **Fig. 6.2b**). If the PE spring's torsional stiffness is small compared to the beam's bending stiffness, reducing the beams cross-section at certain points adds additional degrees of freedom (see **Fig. 6.2b**). Considering 2DOF the system can be modelled mathematically with Eq. (3.28) in either case:

$$M\ddot{x} + C\dot{x} + K(x)x + K_{PE}(x) \cos(\Omega_{PE}t)x = 0.$$

Hence all findings in Section 3.2, Section 4.2 and Section 5.2 are applicable.

Applying the findings from Section 5.2.1 the effect of design parameters on the amplitude can be predicted in an early conceptual stage. Different designs configurations can be evaluated and tuned to maximise the amplitude of the free end's vibration and hence to maximise the device's efficiency.

6.2 MEMS Load Cell

A totally different way for PE of a mechanical system is presented by ZHANG, BASKARAN ET TURNER [29]. They demonstrate how to employ a capacitive design for PE. A so called rigid backbone is linked to its surrounding by beam springs (see **Fig. 6.3**). PE is realised by so-called comb drives. Comb drives are comb shaped capacitors which are moveable relatively to each other. In this design the combs move in parallel to each other and do not interdigitate. The electrostatic forces acting between the combs depend on the displacement of the backbone and on the voltage between the combs. Considering this voltage to be time-periodic the electrostatic forces can be modelled by time periodic stiffness parameters, thereby constituting a parametrically excited system.

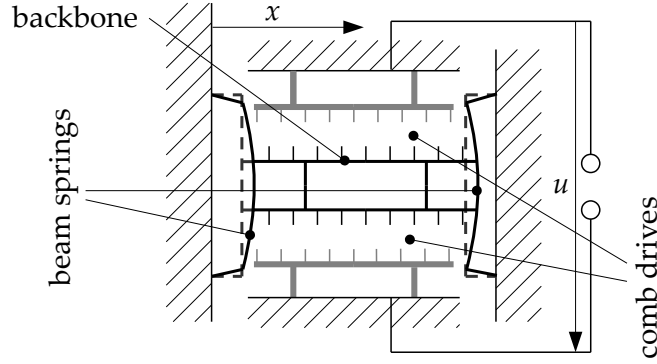


Figure 6.3: MEMS Load Cell from [29]. The mechanical mass spring system undergoes PE by the electrostatic forces by the electric field within the comb drives.

The electrostatic force depends quadratically on the comb's voltage. Having a maximum shift relatively to each other at rest the electrostatic force increases with the teeth approaching each other. Considering the voltage to be harmonic and eliminating harmonic squares, u^2 can be written as

$$u^2(t) = \hat{u}^2 \cos^2\left(\frac{1}{2}\Omega_{PE}t\right) = \hat{u}_{\text{eff}}^2 (1 + \cos(\Omega_{PE}t)), \quad \hat{u}_{\text{eff}} = \frac{1}{\sqrt{2}} \hat{u}. \quad (6.4)$$

Hence the system's equation of motion becomes Eq. (3.2):

$$m\ddot{x} + c\dot{x} + k_{b,\text{lin}}x + k_{b,\text{nonlin}}x^3 + (k_{PE,\text{lin}}x + k_{PE,\text{nonlin}}x^3)(1 + \cos(\Omega_{PE}t)) = 0.$$

Here, m is the mass of the backbone, c may represent some small damping due to structural damping, air damping or both, $k_{b,\text{lin}}$ and $k_{b,\text{nonlin}}$ are the beams stiffnesses. The PE stiffness constants become $k_{PE,\text{lin}} = s_{\text{lin}}\hat{u}_{\text{eff}}^2$ and $k_{PE,\text{nonlin}} = s_{\text{nonlin}}\hat{u}_{\text{eff}}^2$ where s_{lin} and s_{nonlin} are design parameters and depend on the comb drive's dimension and shape.

The device can be used as a load cell: adding an additional mass to the backbone tunes the PR frequency and the bifurcation points of the bifurcated branches. Forward scanning the frequency of the capacitor's voltage the system first follows the bifurcated branch Eq. (3.16b). Increasing the voltage's frequency furthermore, the followed branch becomes unstable leading to a sudden decay of the amplitude of the backbone's vibration. This sharp transition detects the the right bifurcation point Eq. (3.17). From the change in the PR frequency the additional mass can be calculated.

In difference to the MEMS energy harvester from Section 6.1 for this system the PE amplitude is a controllable input for the system. But here $\kappa^2 \neq \kappa_b^2$ because non-linear PE is present in the system. Also, ω_0 depends approximately linearly on the PE amplitude ε_{PE} (see Eq. (5.9)). Hence ε_{PE} has to be chosen carefully when operating the device. The results made in Section 5.1 can be applied to to ensure the desired qualitative behaviour.

At a first glance, extending the device to more degrees of freedom does not seem to be beneficial as additional PRs and PCRs do not improve the device's performance. However, PARs might be advantageous for the system's efficiency. At PR the vibrations am-

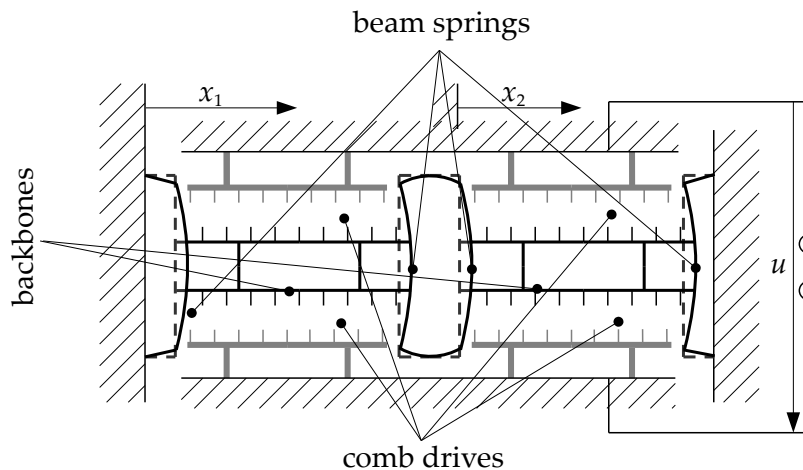


Figure 6.4: MEMS Load Cell depicted in Fig. 6.3 extended by an additional degree of freedom.

plitude increase significantly and waiting for the vibrations to decay is time consuming due to very little damping being present. This process can be accelerated substantially by exploiting PARs when extending the system to 2DOF. After weighing the measurement mass both natural frequencies can be computed. Feeding a voltage with the frequency $\Omega_{PE} = \omega_2 - \omega_1$ excites the system at PAR and hence leads to a faster dissipation of the oscillation energy.

Extending the system to 2DOF can be accomplished as shown in Fig. 6.4 by serially coupling two systems. The electric field between all comb drives results of the voltage $u(t)$ but the effective electrostatic forces depend on the displacements x_1 and x_2 , respectively. Both backbones are parametrically excited. Hence the system can be modelled by Eq. (3.28).

Owing to the approximation Eq. (3.16) of the limit cycles the weighing mass can be calculated for the 2DOF system with no more effort than for the 1DOF system. The detected bifurcation point Eq. (3.17)

$$-\sigma_b = -\frac{\varepsilon_{\text{lin}}}{2\varepsilon\omega_0}$$

reveals the natural angular frequency of the excited mode. Since this natural angular frequency Eq. (3.41) was determined analytically in Section 3.2.2 only a scalar analytical equations has to be evaluated numerically.

6.3 MEMS Bandpass Filter for Electric Signals

ROADS ET AL. [25] present a setting in which a pair of further developed systems from [29] is employed to band filter electric signals. The system in Section 6.2 can be used as a bandpass filter, if an input voltage $u(t)$ is fed into the comb drives. The backbone only vibrates at PR. The comb drives capacitance and hence the current's phase shift oscillate accordingly. This frequency band can be used as a bandpass.

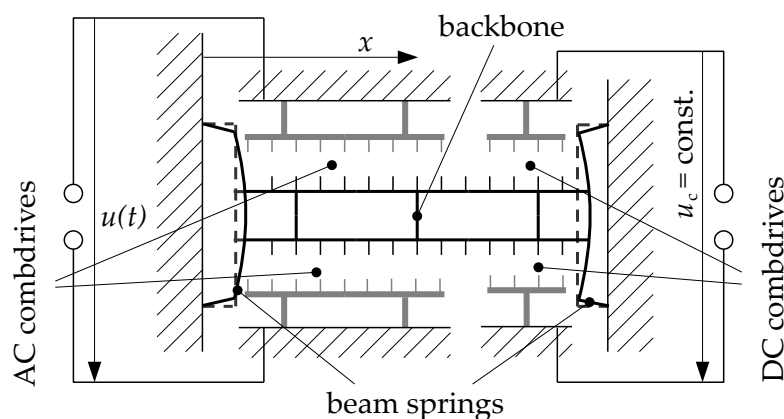


Figure 6.5: Centrepiece of the MEMS bandpass filter from [25]. The mechanical mass spring system undergoes PE by the electrostatic forces by the electric field within the comb drives. The DC comb drives control the magnitude of the effective non-linear stiffness and hence determine the position of the bifurcation points at PR.

As derived earlier the system's equation of motion is Eq. (3.2). However, the magnitude of the electrostatic forces on the comb drive and hence the parameters ε_{lin} and ε_{non} are determined by the amplitude \hat{u} of the voltage $u(t)$. This means the stability of the rest position is determined by \hat{u} as shown in Section 5.1. The PR's centre frequency and the bandwidth depend on \hat{u} . In addition such a system is at risk of showing different qualitative behaviour at PR depending on the value of \hat{u} . These problems are overcome by adding further DC driven comb drives to the system (see Fig. 6.5). As mentioned in Section 5.1, appropriately choosing the magnitude of the control voltage u_c one stability border can be forced to be frequency independent. A pair of these systems, one having a frequency independent stability limit on the left-hand side and one having it on the right-hand side, can be operated in parallel and be used as a bandpass filter [25, 7].

The sudden change from the trivial to the non-trivial bifurcated state causes a sharp roll-off at the filter's corner frequencies [30]. The bandwidth is narrow. A Q-factor of 500 can be realised [25].

Extending the system to 2DOF more PRs become available to be exploited as bandpasses. In addition, due to PCRs, the number of possible instability intervals may increase further than with using another 1DOF system. Also, with more than 1DOF, PARs may occur. This effect can be adopted actively for adding bandstops to the bandpasses.

Similarly to the MEMS load cell in Section 6.3 extending the device to 2DOF can be achieved by serially coupling two systems (see Fig. 6.6) [10, 31]. With the parameter set in Section 3.2.1 two bandpasses at 43.38 kHz and 70.38 kHz can be exploited. The bandwidths are 3.36 kHz, 5.57 kHz and 1.56 kHz. In addition the PAR at 27 kHz can be engaged for fast dissipation of the masses' vibration. For this parameter set, integrating such two 2DOF systems in an IC and using them as frequency controlled switches (see [25] for more details) results in an amplitude characteristic of the filter as depicted in Fig. 6.7.

Note that all bandpasses have ideal filter characteristics because, as explained earlier, a pair of devices with stability limit characteristics complementing each other is in use.

Applying the findings in Section 5.2 designing such 2DOF devices can be accomplished time-efficiently. Time-consuming numerical simulations are not necessary in an early design stage. Approximating the 2DOF system with an analytical 1DOF model the dependence of the system's behaviour on the design parameters can be assessed easily.

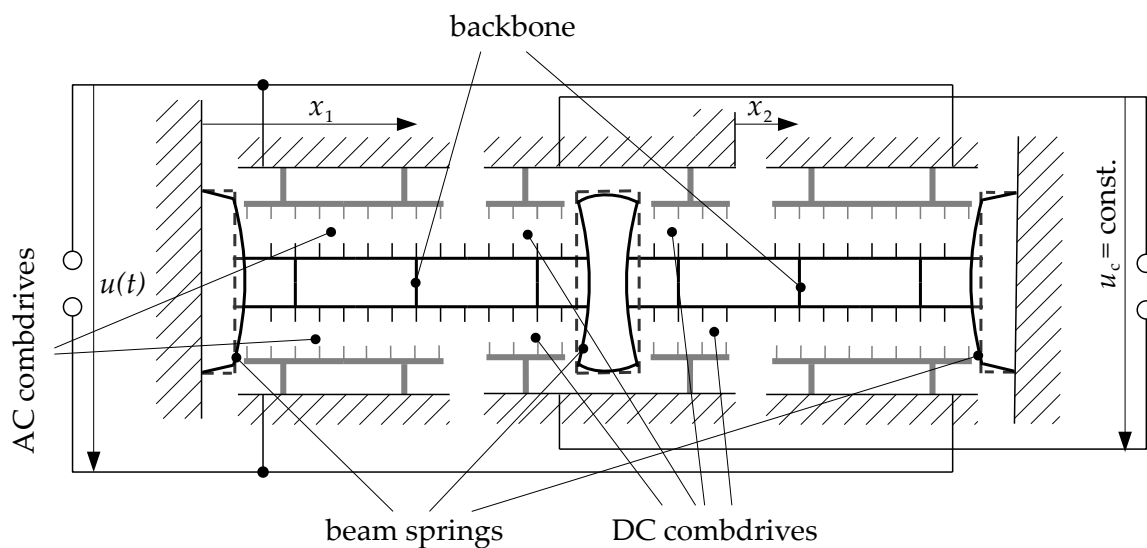


Figure 6.6: System depicted in Fig. 6.5 extended by an additional degree of freedom.

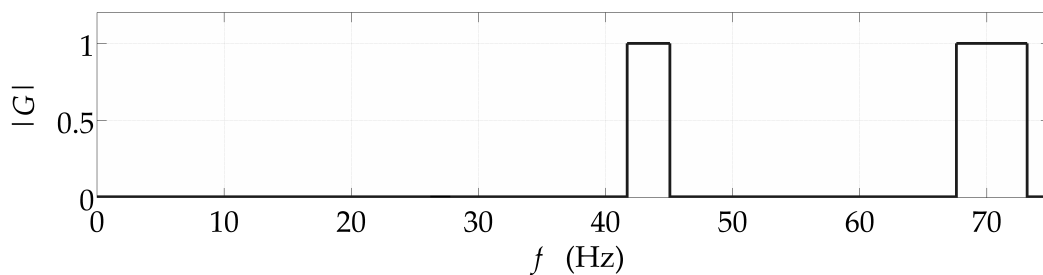


Figure 6.7: Amplitude characteristic of a filter employing a pair of PE devices (as depicted in Fig. 6.6) with parameters as stated in Tab. 3.4.

7 Conclusion

Parametric Excitation (PE) is different to external excitation in many ways: Parametric resonances (PRs), which are by nature intervals of instability, are much more narrow than ordinary resonances. Furthermore, at PRs the vibrations show an exponential increase over time instead of a linear increase over time in case of ordinary resonances. Moreover, since the vibrations at PRs are only limited due to non-linearities, in general much larger vibration amplitudes can be realised than in ordinary systems. In addition the effect of enhanced energy dissipation at parametric anti-resonances offers a possibility to stabilise a system's rest positions. These aspects promise great potential to increase the performance of systems.

In the field of MEMS time-periodic stiffness parameters can be realised more easily than in large scale applications by specially shaped capacitors. Also, in this field of technology simplicity and minimum weight of structures along with optimal performance is crucial. PE MEMS are already implemented in systems successfully outperforming conventional systems. They specifically take advantage of one or more of the features of PE outlined above.

So far the focus of research has mostly been on one degree of freedom (1DOF) systems. This is partly caused by a lack of methods to investigate and design multi degree of freedom (MDOF) systems time-efficiently. Restricting the systems to 1DOF ignores the opportunity to make use of PE effects only available in MDOF systems: parametric combination resonances and parametric anti-resonances. The approaches presented in this thesis support researchers and designers to investigate and design MDOF non-linear PE systems time-efficiently employing analytical, semi-analytical and numerical methods. Furthermore the quasi-modal reduction of the phase space allows to concentrate on important state parameters and to depict states of MDOF non-linear PE systems graphically in, to three dimensions reduced, phase spaces and two dimensional sections of those. This enables scientists to investigate MDOF systems which often means a major progress in terms of the system performance.

Still, the work presented here is only of theoretical nature. Physical experiments are necessary to proof whether the expectations can be met in technical systems. Moreover, cases of non-steady PE amplitudes, e.g. transient or fluctuating PE amplitudes, are complicated to investigate. However, for systems for which the PE amplitude is caused by an uncontrollable input variable, investigating the system for certain fixed PE amplitudes might not be sufficient. More research has to be carried out to fully understand such systems.

Bibliography

- [1] Huan, R. H., Zhu, W. Q., Ma, F., and Liu, Z. H., 2014. "The Effect of High-Frequency Parametric Excitation on a Stochastically Driven Pantograph-Catenary System". *Shock and Vibration*, **2014**, pp. 1–8.
- [2] Spiegelberg, H., Gutschmidt, S., and Hagedorn, H., 2012. "Stability Analysis of a Two-blade Wind Turbine with Floquet Theory". In Proc. 1st EUROMECH Colloquium 532 on Time-periodic Systems, pp. 76–79.
- [3] Han, Q., and Chu, F., 2013. "Parametric Instability of a Jeffcott rotor with Rotationally Asymmetric Inertia and Transverse Crack". *Nonl. Dynamics*, **73**(1-2), pp. 827–842.
- [4] Tondl, A., 1998. "To the Problem of Quenching Self-excited Vibrations". *Acta Technica CSAV*, **43**, pp. 109–116.
- [5] Dohnal, F., and Mace, B., 2008. "Amplification of Damping of a Cantilever Beam by Parametric Excitation". In Proc. MOVIC 2008. MOVIC2008/1248.
- [6] Ecker, H., 2005. *Suppression of Self-excited Vibrations in Mechanical Systems by Parametric Stiffness Excitation*. ARGESIM, Vienna.
- [7] Rhoads, J. F., Shaw, S. W., Turner, K. L., Moehlis, J., DeMartini, B. E., and Zhang, W., 2006. "Generalized Parametric Resonance in Electrostatically Actuated Microelectromechanical Oscillators". *J Sound and Vibration*, **296**(4-5), pp. 797–829.
- [8] Kniffka, T. J., 2012. "Studies on Anti-resonance in Parametrically Excited MDOF Torsional Vibrations". Master's thesis, TU Wien, Vienna.
- [9] Blanch, G., 1972. "Mathieu Functions". In *Handbook of Mathematical Functions with Formulas, Graphs, and Mathematical Tables*, M. Abramowitz and I. A. Stegun, eds., Appl. Math. Ser. **55**. Nat. Bureau of Standards, USA, Washington D.C., pp. 721–746.
- [10] Kniffka, T. J., Welte, J., and Ecker, H., 2012. "Stability analysis of a time-periodic 2-dof MEMS structure". *AIP Conf. Proc.*, **1493**(559), pp. 559–566.
- [11] Kniffka, T. J., and Ecker, H., 2013. "Observations Regarding Numerical Results Obtained by the Floquet-Method". In Proc. ASME 2013 IDETC/CIE. DETC2013/MSNDC-13292.
- [12] Ecker, H., and Pumhössel, T., 2012. "Vibration Suppression and Energy Transfer by Parametric Excitation in Drive Systems". *J Mechanical Engineering Science. Proc. Institution of Mechanical Engineers, Part C* **226**(8), pp. 2000–2014.

- [13] Ecker, H., 2009. "Parametric Excitation in Engineering Systems". In Proc. COBEM 2009.
- [14] Doedel, E. J., Govaerts, W., and Kuznetsov, Y. A., 2003. "Computation of Periodic Solution Bifurcations in ODEs Using Bordered Systems". *SIAM J. Numer. Anal.*, **41**(2), pp. 401–435.
- [15] Doedel, E. J., and Friedman, M. J., 1989. "Numerical Computation of Heteroclinic Orbits". *J Comp. and Appl. Math.*, **26**, pp. 155–170.
- [16] Govaerts, W., Kuznetsov, Y. A., and Dhooge, A., 2005. "Numerical Continuation of Bifurcations of Limit Cycles in MATLAB". *SIAM J Sc. Comp.*, **27**(1), pp. 231–252.
- [17] Gray, B., 1975. *Homotopy Theory; an Introduction to Algebraic Topology*. Pure and Applied Mathematics **64**. Acad. Press, New York.
- [18] Kuznetsov, Y. A., 1998. *Elements of Applied Bifurcation Theory*. 2nd ed., Appl. Math. Sc. **112**. Springer, New York.
- [19] Lyapunov, A. M., 1966. *Stability of Motion*. Academic Press, New York, London.
- [20] Thomas, O., Lazarus, A., and Touzé, C., 2010. "A Harmonic-based Method for Computing the Stability of Periodic Oscillations of Non-linear Structural Systems". In Proc. ASME 2010 IDETC/CIE. DETC2010-28407.
- [21] Verhulst, F., 1996. *Nonlinear Differential Equations and Dynamical Systems*. 2nd ed. Springer, Berlin.
- [22] Welte, J., 2012. "Parametric Excitation in Microelectromechanical Systems (MEMS)". Master's thesis, TU Wien, Vienna.
- [23] Guckenheimer, J., and Holmes, P., 1983. *Nonlinear Oscillations, Dynamical Systems, and Bifurcations of Vector Fields, 7th edition*. 7th ed., Appl. Math. Sc. **42**. Springer, New York.
- [24] Nayfeh, A. H., and Mook, D. T., 1979. *Nonlinear oscillations*. John Wiley & Sons, New York.
- [25] Rhoads, J. F., Shaw, S. W., Turner, K. L., and Baskaran, R., 2005. "Tunable Microelectromechanical Filters that Exploit Parametric Resonance". *J Vibration and Acoustics*, **127**(5), pp. 423–430.
- [26] Jia, Y., Yan, J., Soga, K., and Seshia, A. A., 2013. "Parametrically Excited MEMS Vibration Energy Harvesters with Design Approaches to Overcome the Initiation Threshold Amplitude". *J Micromechanics and Microengineering*, **23**. 114007.
- [27] Varshney, U., 2007. "Pervasive Healthcare and Wireless Health Monitoring". *Mobile Networks and Applications*, **12**(2-3), pp. 113–127.
- [28] Jia, Y., Yan, J., Soga, K., and Seshia, A. A., 2012. "Parametrically Excited MEMS Vibration Energy Harvesters". In Proc. PowerMEMS 2012, pp. 215–218.

- [29] Zhang, W., Baskaran, R., and Turner, K. L., 2002. "Effect of Cubic Nonlinearity on Auto-parametrically Amplified Resonant MEMS Mass Sensor". *Sensors and Actuators A: Physical*, **102**(1), pp. 139–150.
- [30] Kniffka, T., Mace, B., Halkyard, R., and Ecker, H., 2014. "Combdriiven MEMS: Towards Ideal Filters". In Proc. IEEE IMSNZ Conf. 2014.
- [31] Welte, J., Kniffka, T. J., and Ecker, H., 2013. "Parametric Excitation in a Two Degree of Freedom MEMS System". *Shock and Vibration*, **20**(6), pp. 1113–1124.

Curriculum Vitae

Education

- since 10/2012 **TU Wien, Austria**
Doctoral programme
- 10/2010–09/2012 **TU Wien, Austria**
Master's programme Mechanical Engineering
- Area of specialisation: applied dynamics and simulation,
technical dynamics and modelling
- Master's thesis: "Studies on Anti-resonances of Parametrically
Excited MDOF Torsional Vibration Systems"
graduation with distinction
- 10/2007–09/2010 **Leibniz Universität Hannover, Germany**
Bachelor's programme Mechanical Engineering
- Area of specialisation: mechanics and design
- Bachelor's thesis: "Evaluation of Actuator Technologies for an Ap-
plication in a Variable Configurable Display and
Design of a Keypad with Haptic Feedback"
- 06/2006 **Gymnasium Schillerschule, Hanover, Germany**
Abitur (higher education entrance qualification)

Professional Experience

- 03/2014–06/2015 **University of Auckland, Auckland, New Zealand**
Teaching Assistant
courses: Dynamics, Managing Design and Communication,
Dynamics of Fluids and Structures, Engineering Vibrations
- 10/2012–02/2014 **TU Wien, Austria**
Research and Teaching Assistant
research on parametrically excited systems
courses: Continuous Simulations, Vibrations, Rotor Dynamics
- 05/2012–09/2012 **TU Wien, Austria**
Teaching Assistant
courses: Rotor Dynamics, Machine Dynamics,
Measurement and Vibration Technology

03/2011–02/2012 **TU Wien, Austria**
Teaching Assistant
courses: Machine Dynamics, Mechanics 1, Mechanics 2

Awards and Grants

10/2015–06/2016 **TUtheTOP—High Potential Programm TU Wien**
sponsorship scheme with industrial cooperation,
programme partner: **Techniker Cercle**,
individual partner: **Infineon Austria**

3/2015–08/2015 **Marietta Blau Grant**
full study grant for highly qualified doctoral candidates by the
Austrian Ministry of Science, Research and Economy

03/2014–03/2015 **One-year Grant for Doctoral Candidates**
full study grant by the **German Academic Exchange Service**

10/2013 **Grant by the Faculty of Mechanical and Industrial Engineering,
TU Wien**

06/2012 **Best Student Paper Award ICNPAA 2012**
9th International Conference on Mathematical Problems in
Engineering, Aerospace and Sciences, Vienna, Austria

06/2012 **German Student Academy (DSA) 2005, Rostock, Germany**
summer academy for highly talented high school students,
grant for participation by the
German Ministry of Education and Research, and the
Stifterverband für die Deutsche Wissenschaft

Focus of Interest

- modelling and simulation of mechanical linear and non-linear systems
- continuous simulation, discrete event simulation and state event simulation
- time-periodic and non-linear vibration systems
- machine dynamics and rotor dynamics
- product development, value and performance optimisation